Morris, J.D., Villinger, H.W., Klaus, A., et al., 2003
Proceedings of the Ocean Drilling Program, Initial Reports Volume 205

5. SITE 1254[1]

Shipboard Scientific Party[2]

SITE SUMMARY

Site 1254 is located ~1.5 km arcward from the deformation front at a water depth of 4183 m, close to the holes drilled at Site 1040 during Leg 170 (Kimura, Silver, Blum, et al., 1997). Hole 1254A is positioned ~15 m west of Hole 1040C, and Hole 1054B is ~50 m northeast of Hole 1040C (Figs. **F1, F2, F3**). Therefore, all comparisons to Leg 170 results are to Hole 1040C at Site 1040, as it was the only one that penetrated the décollement and underthrust.

The primary objective of Site 1254 was to investigate a fault zone in the prism, investigate the décollement, and install a long-term observatory for monitoring of fluid flow, pressure, and temperature in the décollement. Results from Site 1040 (Kimura, Silver, Blum, et al., 1997) and seismic data (Fig. **F3**) provided the framework for drilling the sedimentary sequence and the interpretation of pore fluid geochemistry and structure. Site 1040 geochemical anomalies suggest that deeply sourced fluids, perhaps from seismogenic depths, are migrating along the décollement and prism fault. At Site 1254, we intended to investigate in detail the structure and geochemistry of these zones and install an observatory in the décollement. Although perturbed by drilling disturbance, high recovery at Site 1254 enabled detailed structure observations (where they were considered reliable) and higher-resolution chemical sampling than was possible during Leg 170. The high recovery also made it possible to better correlate intervals of maximum inferred fluid flow to specific structural horizons.

The seismic record (Fig. **F3**) in the vicinity of Site 1254 (common midpoint 3130) shows no coherent reflections above the décollement. This reflects the general chaotic sedimentary pattern observed in cores from Hole 1254A. The first prominent reflector relevant for drilling objectives is at 6 s two-way traveltime, which marks the boundary between margin sediments and the underthrust sequence, cored at 361

F1. Bathymetric map of Leg 205 and 170 drill sites, p. 42.

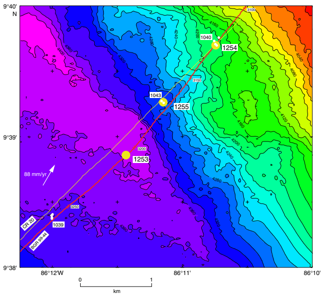

F2. Location of Site 1254, p. 43.

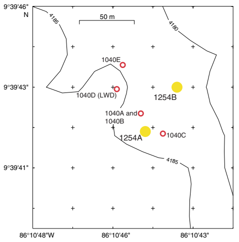

F3. Multichannel seismic profile BGR 99-44, p. 44.

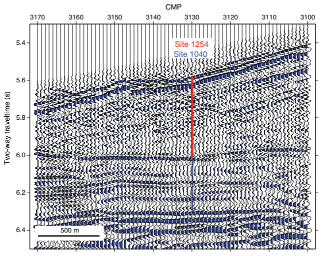

---

[1] **Examples of how to reference the whole or part of this volume.**
[2] **Shipboard Scientific Party addresses.**

Ms 205IR-105

meters below seafloor (mbsf). The prism fault zone is not imaged in the seismic data.

After setting the reentry cone in Hole 1254A, we cored the prism fault zone (150–230 mbsf) and the décollement (300–367.5 mbsf) with the rotary core barrel (RCB). Recovery averaged ~88% throughout the cored interval. With generally good hole conditions, we planned to case the hole with 10¾-in casing. However, after running the casing to 232 mbsf, the casing could no longer advance and had to be pulled up. Soon it became clear that the reentry cone had hung up on the casing; when the sections that were jammed into the cone were pulled up into the moonpool, it became obvious that the casing had collapsed in the throat of the reentry cone for unknown reasons. Hole 1254B, the second attempt for a CORK-II installation, was offset 50 m to the northeast. However, drilling conditions there prevented us from deepening the hole to >278 mbsf, when the drill string got stuck during several attempts to deepen the hole. Therefore, we decided to install the osmotic fluid sampler in the upper fault zone with the screen located at 225 mbsf; this interval, cored and analyzed in Hole 1254A, was not recored because of time constraints. The depth for the screen was determined by inference from the geochemical results of Hole 1254A, which indicate that deeply sourced fluids containing thermogenic hydrocarbons are present in the target zone. After a successful installation of the 10¾-in casing, the installation of the CORK-II failed as it got stuck ~20 m above the final depth. Attempts to penetrate further probably caused the 4½-in casing to break right below the CORK-II head. Thus, we had to abandon Hole 1254B with ~20 m of casing sticking out of the reentry cone.

In total, we drilled 367.5 m at Site 1254, with 140.5 m cored and 227 m drilled and washed. Because of the nature of the tectonic structures encountered, part of the core was heavily disturbed by RCB drilling, which makes structural and paleomagnetic studies difficult. However, the generally good recovery (average = 89%) allowed extensive whole-round sampling of the cored sections for pore water and organic geochemistry in addition to sampling aboard the ship for physical property and paleomagnetic studies and provided personal samples for postcruise studies.

Lithostratigraphy

The sedimentary sequence recovered at Site 1254, Subunit P1B after Leg 170, is dominated by structureless and typically unsorted dark greenish gray claystones with variable subsidiary quantities of silt and rare interbedded volcanic ashes, sandstone, and redeposited limestone clasts, spanning a sparsely dated sequence of presumed Pliocene–Pleistocene age (Fig. F4). Recovered cores often show moderate to extreme degrees of drilling disturbance; nonetheless, coherent fragments of more lithified sedimentary rocks do indicate that much of the section is either massive or slightly mottled, which is suggestive of moderate bioturbation.

F4. Structural and geochemical results, p. 45.

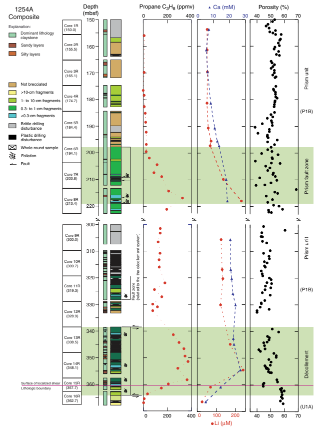

The dominance of clay minerals within the sequence is readily apparent from smear slides, as is the downcore decrease in volcanic ash. Fresh volcanic glass is present at low (<10%) and moderate (<30%) levels above 230 mbsf, becoming heavily altered deeper (>300 mbsf) in the section. The continental provenance of the sediments cored in Hole 1254A is clear from the abundance of quartz and feldspar grains and also from the bright brownish red biotite mica flakes that are found at all stratigraphic levels. The terrigenous nature of the sediments is confirmed by the very low biogenic component (<5%) of the sediment, restricted to occasional nannofossils above 200 mbsf and below 360 mbsf. Below Section 205-1254A-15R-2 (360.62 mbsf), the proportion of diatoms increases sharply (>10%). The appearance of diatoms is considered important for understanding the structure of the forearc prism because the uppermost sedimentary subunit in the subducting Pacific stratigraphy (Subunit U1A) recorded high percentages of diatom abundance (Kimura, Silver, Blum, et al., 1997).

Redeposited blocks of shallow-water peloid limestones, lithified prior to incorporation within mudstones, are found throughout the section, which is consistent with fluidized gravity and debris flows being the dominant mode of sedimentation. The cobbles show evidence for a shallow-water depositional environment, identified by shallow-water bivalve shell fragments and small gastropods.

Compared to the sequence of well-preserved tephra found at Sites 1039 and 1253 on the subducting Cocos plate, there is little well-preserved tephra stratigraphy found at Site 1254. Although occasional thin altered ash layers are recognized, they are rare, typically <2 cm thick, and often completely altered to claystone. Volumetrically, the tephra represents <1% of the total section. Two thicker coherent ash layers are recorded at Site 1254 (intervals 205-1254A-5R-8, 14–20 cm, at 193.49–193.55 mbsf, and 8R-8, 22–65 cm, at 222.37–222.80 mbsf). Both the thicker ashes preserve relatively fresh glass shards and are interpreted to be the product of primary air fall deposition followed by settling through the water column. The base of the tephra recovered in Section 205-1254A-8R-8 was not recovered, resulting in a minimum thickness estimate of 43 cm. Because Site 1254 is ~150 km from the nearest arc volcano in Central America, this thickness at this range indicates that this must have been a very large eruption, comparable to the Minoan ash from Santorini Volcano as the closest analog (Watkins et al., 1978). Major and trace element analyses of this tephra (interval 205-1254A-8R-8, 22–65 cm) characterize its source as being the volcanic arc of Central America.

Structural Geology

Coring at Site 1254 targeted two different structural domains based on Site 1040 results: (1) a fault zone from 150 to 223 mbsf containing fractured sediment and locally steep bedding dips called the prism fault zone and (2) the décollement zone from 300 to 368 mbsf (Fig. F4). A variety of deformation structures is present at Site 1254, and description of deformation was based on breccia size, foliation, hardness of breccia clasts, and the presence of polished surfaces. Because structural observations in poorly lithified material require good quality cores and the recovered cores are sometimes severely disturbed by drilling, it is difficult to distinguish natural from drilling-induced features.

Cores from 150 to 223 mbsf show various degrees of deformation, with the intensity of deformation, particularly brecciation and brittle shearing, increasing downward, reaching a peak at ~219 mbsf. Deformation is discontinuous, being focused along sheared horizons, 20 cm to 2 m thick. These horizons are characterized by stratal disruption, foliated breccia with fragments as small as a few millimeters in length, brittle shear zones, deformation bands, and distinctly inclined bedding. A concentration of deformation structures at ~210 and 219 mbsf documents that this is indeed a fault zone. Riedel shears within a well-preserved foliated breccia (interval 205-1254A-8R-1, 0–24 cm; 213

mbsf) indicate reverse movement. Paleomagnetic reorientation of this shear zone suggests that the fault is a northeast- or southwest-dipping feature, implying that it is a thrust fault (Fig. F4) that strikes parallel to the deformation front.

The second interval cored started at 300 mbsf, and well-preserved structures are observed starting at Core 205-1254A-11R (319.30 mbsf) (cf. Fig. F4). Cores typically show pervasive drilling disturbance, previously described during Leg 170 as "spiraliferous" (Kimura, Silver, Blum, et al., 1997), consisting of a spiral rotation of clay-rich sections. Despite the drilling disturbance, some bedding plane orientations were observed. Bedding and fissility show various dips, indicating heterogeneity of deformation, but the paleomagnetic reorientation shows that they consistently dip northeast or southwest, with strike parallel to the deformation front. The recovered section from 319.30 to 367.50 mbsf is characterized by intense deformation. The deformation is heterogeneous, and brecciation, usually associated with a strong foliation, is the basis for dividing the deformed interval in two zones.

The upper zone from 319.30 to 328.90 mbsf is characterized by generally increasing brecciation with depth, producing fragments of <0.3 cm in length. Foliation is common throughout Core 205-1254A-11R, resulting in a clear alignment of clasts, which are equidimensional but internally strongly foliated. Below 324.15 mbsf (Core 205-1254A-12R), deformation sharply decreases and consolidated and coarsely brecciated sand layers become common. These sandstone layers have steeply dipping laminations and a few web structures. We interpret this well-defined change in deformation intensity as marking the top of a relatively less deformed rock volume that may be the footwall of the fault identified between 319.3 and 328.9 mbsf and may be related to the décollement zone. This indicates a more articulate structural geometry for the décollement and associated faults than that observed at Site 1040 (Kimura, Silver, Blum, et al., 1997; Tobin et al., 2001).

The upper boundary of the décollement zone at 338.5 mbsf is defined by increasing deformation intensity in Core 205-1254A-13R. The upper boundary of the décollement is difficult to define precisely because the deformation gradually increases in intensity with depth. A sharp increase in deformation is not observed between Cores 205-1254A-12R and 13R. The décollement zone itself is heterogeneous, with a general downward increase of brecciation intensity, fragment aspect ratio, and hardening of the sediments. Despite the good recovery, "spiraliferous" drilling disturbance affects the cores, although less extensively than at Site 1040. Unlike at Site 1040, "spiraliferous" disturbance is not concentrated in the lowermost part of the décollement zone. Brecciation can be pervasive and severe with fragments characterized by polished surfaces; the development of scaly fabric is precluded by the abundant silt and sand in the sediments. From 354.8 to 355.9 mbsf, sandstone layers are brecciated and foliated. At 360.60 mbsf the appearance of diatoms in the sediments marks the lithologic boundary with the hemipelagic Subunit U1A of the underthrust (Figs. F4, F5). The lithologic boundary is present below 50 cm of finely brecciated sand and 10 cm of highly sheared clay indicating a surface of ductility contrast that appears as a major structural discontinuity. The hemipelagic sediments below the lithologic boundary are still intensely deformed and brecciated with aligned clasts showing a strong internal foliation (Fig. F6). The base of the décollement is placed at 364.2 mbsf and is below the lithologic boundary. Deformation starts to decrease and becomes localized below 364.2 mbsf, where intact sediments are separated by 3-

F5. Lithologic boundary between Subunits P1B and U1A, p. 46.

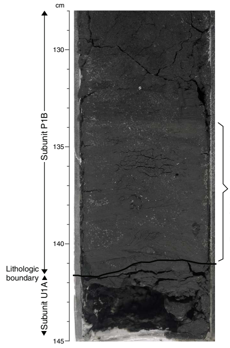

F6. Deformed hemipelagic Subunit U1A, p. 47.

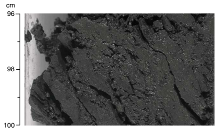

to 8-cm-thick brittle shear zones producing gouge or Riedel shears (Fig. F7). These brittle shear zones show exceptionally consistent normal movement and landward dips when reoriented to the geographical coordinates. The hemipelagic sediments above 364.2 mbsf are also deformed by normal faults; a few of them are present as conjugate features. At Site 1254 the décollement zone has a thickness of 25.7 m. Based on this interpretation, the décollement has cut down into the uppermost underthrust section, incorporating a small amount (4.2 m) of Subunit U1A into its base. The complex geometry of the décollement system at Site 1254 contrasts with that described at Sites 1040 and 1043, where the top of the décollement was identified by an increase in brecciation and the lithologic boundary between the prism and the hemipelagic subunit coincides with the base of the décollement.

F7. Fault gouge, p. 48.

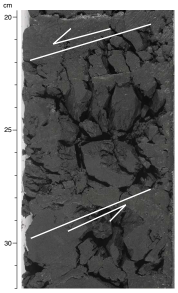

Paleomagnetism

Paleomagnetic measurement on archive-half sections and discrete samples are severely degraded by pervasive drilling disturbance and drill string overprints. Natural remanent magnetization (NRM) inclinations are still variable after alternating-field demagnetization and make the firm identification of magnetic polarity changes and the construction of a magnetostratigraphy difficult. However, the declination data were useful in carefully selected intervals to reorient core segments for structural interpretation. Demagnetization curves of discrete samples from the prism sediments (Subunit P1B) are often poorly behaved, indicating that they have a very unstable magnetization. Two significant high magnetic intensity and susceptibility zones were observed in the intervals from 184 to 202 mbsf and from 310 to ~350 mbsf. The interval of the first anomaly is close to the prism fault zone at ~210 to 220 mbsf, and the second anomaly is within the décollement zone. These variations suggest changes in concentration, grain size, and chemical components of magnetic minerals related to lithology and/or chemical alteration perhaps related to fluid flow.

Inorganic Geochemistry

A total of twenty 35- to 45-cm whole rounds were sampled at Site 1254 for pore fluid geochemistry. Pore waters were analyzed for Ca, Mg, K, Na, B, Ba, Fe, Mn, Sr, H_4SiO_4, NH_4, and SO_4 concentrations (Fig. F4). Samples taken from between 305 and 366 mbsf were analyzed for Li, Ca, K, Mg, and Na in "real time" on the inductively coupled plasma–atomic emission spectrophotometer (ICP-AES) aboard the ship to identify the horizon of maximum flow of deeply sourced fluid within the décollement zone based on correlation to nearby Site 1040. The real-time chemical analyses were available 2 hr after core recovery and, together with careful observations of hydrocarbon gas concentrations and penetration rate, helped to identify the top of the underthrust section.

The pore fluid salinity in the prism sediments (Subunit P1B) is lower than that of seawater by 20%, and thin excursions of higher dilutions up to a maximum of 29% are present at 218 and ~351 mbsf (13 m from base of the décollement zone). The two main salinity minima also show C_3H_8, Li, and Ca concentration maxima, as well as Mg/Ca, K, and Mg minima. The geochemical excursions between 210 and 218 mbsf are present within a highly fractured interval interpreted as a fault zone, whereas the excursions at ~351 mbsf are located within the décollement zone and appear to coincide with a brecciated, moderately indurated, sandy interval. A small peak in Ca, Li, and C_3H_8 concentrations is present at 330 mbsf and may also be associated with a similar sandy, brecciated interval within the décollement. These data, together with results from the entire interval cored during Leg 170, suggest that fluid has migrated along conduits and permeated the lower half of the deformed wedge. Assuming that the geothermal gradient is ~20°–30°C/km, the source region must be present at >4 km depth because the *minimum* temperature required for thermogenic gas formation is 80°–90°C. The minima in K concentrations at 218 and 351 mbsf further suggest that the deformed sediments have been permeated by a fluid from an elevated temperature source of 80° to 120°C, where the illitization reaction, which consumes potassium, is effective. Also, the K depletion signature of this fluid provides an approximate upper limit to the temperature at the source of ~<150°C, although the data do not preclude the possibility of mixing between fluids from greater depths (>150°C) with shallower fluids along the flow path. Above this temperature, fluid-rock reactions leach potassium from the rocks. Lithium, like K, is partitioned into solids at low to moderate temperatures. At higher temperatures, >100°C but <250°C, Li is released into the fluid phase (Chan and Kastner, 2000). The precise threshold temperatures for the partitioning of Li and K into the solid or fluid phases are as yet unknown. Clay and other silicate mineral dissolution or alteration releases B into the fluid phase; however, clay, especially illite, formation consumes B and may be responsible for the low B concentrations within the deformed sediments. The deeply sourced fluid, however, is not enriched in dissolved silica.

Geochemical excursions in Ca, Li, C_3H_8, K, and Mg are present at ~218 mbsf within the prism fault zone at Site 1254. Similar increases in Ca, Li, and C_3H_8 concentrations, as well as marked decreases in Mg and K concentrations, were observed at an observed prism fault zone at Site 1040; however, the prism fault zone was present between ~180 and 200 mbsf. Therefore, the upper geochemical excursion in Hole 1254A is ~20 m below the same anomaly observed during Leg 170.

The geochemical change at ~218 mbsf separates intervals with pore fluid chemistry typical of clay-rich sediments from those permeated by a fluid from an elevated temperature source, and it seems to be independent of lithology. Bulk sediment chemistry is also relatively homogeneous throughout the entire prism. Changes in pore water chemistry in a lithologically and chemically homogeneous sediment section likely result from fluid advection into the lower half of the deformed sediment section. The chemical changes observed at the base of the fault zone (conduit) at ~218 mbsf are similar to those observed near the bottom of the décollement zone. Except for the biogeochemical components, the pore fluid concentration depth profiles of the underthrust section are similar to those at the reference Site 1039. The concentrations themselves are slightly different in magnitude than those at Site 1039, presumably reflecting the changes in solubilities and dissolution rates of the major sediment components under the new pressure regime as they are underthrust. In contrast to Site 1039, the higher NH_4^+ concentrations and the absence of SO_4 at the interface between décollement and the underthrust sediments reflect the fact that all the sulfate is reduced at Site 1254 by microbiological activity. Sulfate reduction thus reaches completion in the uppermost few meters of the underthrust hemipelagic section, resulting in somewhat elevated CH_4 concentrations within the zero-sulfate depth interval. These geochemical patterns are similar to those observed in Hole 1040C.

Organic Geochemistry

Volatile hydrocarbon gases were sampled by headspace and vacutainer techniques at a higher frequency than pore water samples to assist in determining the exact depths of the inferred fluid conduits associated with fault zones discovered at Site 1040. Analyses of the vacutainer samples (Fig. F4) show that the gas mainly consists of CH_4 but also contains considerable amounts of higher alkanes up to C_5H_{12}. Methane concentrations were very high (7–9 $\times 10^5$ ppmv) throughout the cored interval but dropped to ~4 $\times 10^4$ ppmv directly below the décollement zone at 364 mbsf. Propane, which is a strong indicator of deeply sourced fluids because of its thermogenic origin (>80°–90°C required), shows one peak at 216 mbsf and another in the basal part of the décollement zone at 355 mbsf, with maximum levels of 326 and 370 ppmv, respectively. These high C_3H_8 concentrations correlate with structurally identified fault zones. Similar patterns, at much lower concentrations, were also observed in the headspace gas samples.

Microbiology

Samples for microbiological investigations were taken and either frozen or fixed for postcruise adenosine triphosphate (ATP) quantification, deoxyribonucleic acid (DNA) assessment, or cell counts. Samples of drilling water were frozen to evaluate contamination of cores. The chemical tracer for quantifying microbiological contamination was not deployed during coring at Site 1254 because of concern that the trace element chemistry of the perfluorocarbon tracer may affect postcruise pore fluid geochemical analyses. Particulate tracer tests yielded fluorescent microsphere counts suggesting very low to no particulate contamination in the interior of the microbiology whole rounds.

Physical Properties

Porosities and bulk densities at Site 1254 (Fig. F4) exhibit trends similar to those seen in Hole 1040C. Variations in porosity and density within the structurally defined décollement zone correlate with core descriptions: in general, zones of lower porosity (40%–45%) correspond to zones characterized by "spiral" deformation interpreted as drilling disturbance; zones of higher porosity (50%–55%) correspond to zones characterized by brecciation. Porosity is also low (42%–44%) between 358 and 361 mbsf, within and adjacent to a zone of localized shear. Porosity increases and bulk density decreases sharply below 361 mbsf across the lithologic boundary between prism sediments and Pleistocene diatomaceous claystone.

Downhole Measurements

We attempted three downhole measurements of formation temperature and pressure, two with the Davis-Villinger Temperature-Pressure Probe (DVTPP) at 50 and 200 mbsf and one at 150 mbsf with the Davis-Villinger Temperature Probe (DVTP). The temperature measurement at 200 mbsf was the only deployment with an interpretable decay curve and indicated a temperature of 3.59°C. This is in good agreement with measurements from Hole 1040C. All pressure measurements were unsuccessful because of tool movement when in formation. However, pressures measured at the mudline and bottom of the hole are in very good agreement with expected hydrostatic pressures expected at that depth, which clearly demonstrates that the pressure sensor is reliable.

Summary

In summary, the analyses of structural fabric and geochemical anomalies allowed us to identify a fault and geochemical boundary at ~218 mbsf. The region above has pore fluids typical of clay-rich sediments; below, the section is lithologically homogeneous but permeated by a fluid from a source at elevated temperature. At ~338.5 mbsf a fault marks the upper boundary of the décollement zone, which extends into the upper meters of the underthrust sequence at 364.2 mbsf. Maximum pore fluid chemical anomalies, indicative of active fluid flow, may preferentially follow zones characterized by brittle fabric. Analysis of cores from the two intervals allowed us to select the optimal depth interval for the long-term borehole fluid sampler experiment. However, because of unstable hole conditions, the attempts to install a CORK-II failed and Site 1254 had to be abandoned because of time constraints.

OPERATIONS

Transit from Site 1253 to Site 1254 (Proposed Site 1040R-B)

After the drill string was pulled out of Hole 1253A, the ship moved in dynamic-positioning mode to Site 1254 (1.1 nmi) while the drill string was being retrieved. The beacon from Site 1253 was recovered at 0430 hr on 11 October 2002 and redeployed at 0945 hr on 11 October at Site 1254A (all times reported are local ship time, which is Universal Time Coordinated [UTC] – 5 hr).

Site 1254 (Proposed Site 1040R-B)

Hole 1254A

The first operation at Site 1254 was to install a reentry cone and 16-in surface casing. Two joints (29.37 m) of 16-in casing were made up to a casing hanger and latched into a standard reentry cone. The reentry cone was lowered to the seafloor, and Hole 1254A was initiated at 2225 hr on 11 October. The seafloor was determined to be 4194 meters below rig floor (mbrf).

The sediments proved to be quite consolidated near the seafloor, and 10 hr was required to jet in the 16-in casing. The casing running tool was released at 0850 hr on 12 October, and the drill string was pulled out of the hole, clearing the reentry cone at 0900 hr. The camera system was recovered, and the casing running tool cleared the rotary table at 1645 hr 12 October.

After installing the reentry cone and 16-in casing, we assembled an RCB bottom-hole assembly (BHA) and lowered it to the seafloor. Hole 1254A was reentered at 0110 hr on 13 October, and we drilled without coring from the 16-in casing shoe at 4223 mbrf (29 mbsf) to 4244 mbrf (50 mbsf). A DVTPP measurement was made at 50 mbsf, but the data were not usable. Hole 1254A was then drilled from 4244 to 4344 mbrf (50 to 150 mbsf), where a second DVTPP deployment was made; the data were once again not usable. Hole conditions through this part of Hole 1254A were stable, and the rate of penetration was 9.3 m/hr.

RCB Cores 205-1254A-1R through 6R were cut from 4344 to 4397.8 mbrf (150–203.8 mbsf). A third DVTPP measurement was made at 203.8 mbsf, and for the first time during this leg, good temperature data were recorded. The pressure data, however, were not good. RCB Cores 205-1254A-7R and 8R were taken from 4397.8 to 4417 mbrf (203.8–223.0 mbsf). Cores 205-1254-A-1R through 8R penetrated 73 m, and we recovered 66.59 m (91%) (Table T1); the overall penetration rate was 10.8 m/hr. No hole problems were encountered, and the hole remained stable while this interval was cored.

T1. Coring summary for Site 1254, p. 92.

Hole 1254A was then drilled without coring from 4417 to 4494 mbrf (223–300 mbsf) in 8.5 hr (9 m/hr). The hole remained stable throughout this drilled interval, requiring only periodic circulation of sepiolite mud to keep the hole clean.

To determine the upper and lower boundaries of the décollement, Hole 1254A was cored from 4494 to 4561.7 mbrf (300–367.5 mbsf). Cores 205-1254A-9R through 16R had a recovery of 58.41 m (87%) (Table T1), and the penetration rate through this interval was 10 m/hr.

Sepiolite mud was circulated periodically over this cored interval to maintain hole stability; however, none of the anticipated hole problems associated with drilling through a décollement occurred. The hole was displaced with 111 barrels of sepiolite, and the RCB bit was pulled out of the hole. The RCB bit cleared the reentry cone at 0530 hr on 16 October and reached the rig floor at 1230 hr.

A BHA was assembled with a 14¾-in bit for opening the hole in preparation for installing the 10¾-in casing string. We reentered Hole 1254A at 2135 hr on 16 October and rotated and washed from the 16-in casing shoe at 4223 mbrf (29 mbsf) to 4527 mbrf (333 mbsf). Fifty barrels of sepiolite mud were then circulated to clean out the hole, and twice the borehole volume was then circulated. We then conducted a wiper trip that encountered a tight spot at 4395 mbrf (201 mbsf). The bit was washed and reamed through the tight spot and lowered back down to the total depth of the 14¾-in hole at 4527 mbrf (333 mbsf); 2 m of fill at the bottom of the 14¾-in section of hole had to be washed out.

We circulated another 50 barrels of sepiolite and twice the hole volume with seawater. A second wiper trip was undertaken back to the 16-in casing shoe and encountered tight spots at 4482, 4420, and 4386 mbrf (288, 226, and 192 mbsf). During the wiper trip back down, the bit encountered a bridge at 4386 mbrf (192 mbsf), which supported ~20,000 lb of drill string weight. We washed and reamed through this tight spot and back down to 4527 mbrf (333 mbsf).

Once again, we swept the hole with 60 barrels of sepiolite and twice the hole volume with seawater. The hole was then displaced with 255 barrels of sepiolite to help stabilize the hole while we prepared to assemble and install the 10¾-in casing string. The drill string encountered no significant drag while it was pulled out of the hole. The bit cleared the reentry cone at 2215 hr on 17 October and reached the rig floor at 0500 hr on 18 October.

Twenty-eight joints (324 m) of 10¾-in casing were made up and attached to a 10¾-in casing hanger. The cementing tools were assembled and attached to the casing running tool, which in turn was made up to the 10¾-in casing string. The 10¾-in casing string was then lowered to the seafloor, and Hole 1254A was reentered at 1738 hr on 18 October.

The 10¾-in casing shoe was lowered to 4426 mbrf (232 mbsf) when it suddenly appeared to hang up, as identified by a reduction in string weight of 20,000 lb. The drill string was immediately picked up to the hanging weight of the string. The casing was lowered again and took weight at the same depth.

A stand of drill pipe had just been picked up, and there was not much traveling space in the rig available to work the casing up and down. The casing was worked within these traveling limits without being able to pass the tight spot.

The space-out was such that the drill string could not be picked up without activating the Crown-O-Matic (the stand of drill pipe was too close to the top of the derrick) and could not be lowered and secured on the rig floor without putting the casing in compression. Thus, the ship was offset far enough to allow the drill string to be landed on the drilling elevator stool without putting the casing in compression. A stand of drill pipe was laid out, and the ship was moved back over the hole. When we raised the drill string so that we could remove a single joint of drill and attach the top drive, the reentry cone was pulled up off the seafloor along with the 10¾-in casing string.

The 10¾-in casing string and reentry cone were worked in an unsuccessful attempt to free the reentry cone from the casing string. The vibration-isolated television (VIT) camera system was lowered to the reentry cone for a visual inspection. It appeared that a joint of 10¾-in casing had collapsed inside the reentry cone. With all options for freeing the reentry cone from the 10¾-in casing string exhausted, the 10¾-in casing string with the reentry cone and 16-in casing attached was pulled out of the hole.

Once the casing string with the stuck reentry cone was clear of the seafloor, we offset the ship 0.5 nmi perpendicular to the seismic line on which Site 1254 is located. If the reentry cone or other hardware fell off during recovery, we didn’t want it to fall in the area where the scientists wanted to attempt another CORK-II installation. The reentry cone was pulled into the moonpool at 0845 hr on 19 October. While laying out the 10¾-in casing string, we found four joints that were bent. This bending likely occurred during attempts to break off the casing inside the reentry cone at the seafloor. Approximately 3 m of a collapsed joint of 10¾-in casing was found protruding out of the top of the reentry cone.

It was deemed unsafe and too costly in time to attempt to salvage the reentry cone and casing. Thus, preparations were made for jettisoning the reentry cone. The connection between joints 7 and 8 was partially loosened. The reentry cone was then lowered below the keel of the ship and hung off near the top of joint 9 in slips at the rotary table. Although the casing was hung off in the slips, the elevator was left attached to the casing and positioned just beneath the collar. A padeye was then welded to the casing just below the elevator to prevent the joint from jumping upward when the reentry cone was released. With all personnel cleared from the rig floor and the moonpool area, the rotary table was engaged to finish unscrewing the loosened connection, and at 0920 hr on 19 October the reentry cone was jettisoned, ending Hole 1254A.

Hole 1254B

The scientific party decided to make a second attempt at installing a CORK-II at Site 1254. The ship was then moved to ~48 m at N36°E from Hole 1254A. After the 10¾-in casing handling equipment was rigged down, the 16-in casing handling equipment was rigged up. A reentry cone, which had been previously assembled for our next site, was moved into the well center on top of the moonpool doors. Two joints of 16-in casing (20 m) plus a 16-in casing cementing shoe were then made up to a 16-in casing hanger, and the assembly was latched into the reentry cone. The jetting BHA was then made up and latched into the 16-in casing hanger. The reentry cone was then picked up off the moonpool doors, and the reentry cone was then lowered to the seafloor. We started washing in the 16-in casing at 2550 hr on 19 October, beginning with Hole 1254B. After it was washed into the seafloor to 20.42 mbsf in 6.5 hr, the casing running tool was released and the drill string was retrieved. Our next step was to drill a 14¾-in hole into which we could install the 10¾-in casing. We assembled a drilling BHA with a 14¾-in bit, lowered it to the seafloor, and reentered Hole 1254B at 2134 hr on 20 October.

The 14¾-in hole was advanced to 4418 mbrf (231 mbsf) when the upper fault zone was penetrated. As we advanced through the fault, increased fill and torque were encountered. The fault zone had to be reamed and swept clean by circulating sepiolite before the bit could penetrate deeper.

When the bit reached 4452 mbrf (265 mbsf), the hole began to pack off around the drill string. The bit was raised 20 m and then washed and reamed back down to 265 mbsf. We drilled to 4465 mbrf (278 mbsf) when the pipe became stuck. After 3 hr of working the pipe with overpull up to 200,000 lb, the pipe was raised again.

Because of the poor drilling conditions, we decided to conduct a wiper trip. The bit was pulled up to 4289 mbrf (102 mbsf), encountering 80,000 lb of drag from 4453 to 4415 mbrf (266–228 mbsf). It took 6.75 hr to wash and ream back to the bottom of the hole at 4465 mbrf (278 mbsf); 40 m of fill in the bottom of the hole had to be drilled and washed out. With hole conditions deteriorating and no hope of setting casing to the décollement, we decided to install a CORK-II to monitor the upper fault zone.

The bit was pulled up to the 16-in casing shoe at 4210 mbrf (23 mbsf), and then the pipe was lowered back down. The bit encountered resistance (took weight) at 4397 mbrf (210 mbsf) and was washed and reamed from there to 4424 mbrf (237 mbsf). With the bit at the bottom of the hole, we circulated from the bottom up in preparation for setting 10¾-in casing. Because the 14¾-in hole extended through the zone of interest, the hole was left full of seawater and no sepiolite mud was used. The bit was pulled out of the hole and was back on the rig floor at 0830 hr on 23 October.

Seventeen joints (197 m) of 10¾-in casing were then assembled, and a casing hanger was attached to the top. The cementing and casing running tools were latched into the casing hanger, and the entire assembly was lowered to the seafloor. At 1822 hr on 23 October, Hole 1254B was reentered with the 10¾-in casing string. It appeared that the hole was producing fluid as we observed, as evidenced by a billowing cloud within the reentry cone and water flowing out of the drill pipe at the rig floor between connections.

The casing was lowered to 4360 mbrf (173 mbsf) when it encountered some resistance and began to take weight. At this point, we picked up the top drive to wash the casing in. The cementing manifold was picked up, and the casing was landed at 2045 hr on 23 October. We confirmed that it was latched in and cemented it in place with 20 barrels of 15.8-lb/gal cement. The 10¾-in casing shoe was at 198.88 mbsf. The casing running tool was released and was back on the rig floor at 0915 hr on 24 October.

Our next operation was to drill out the cement plug and clean out a rathole for the CORK. We assembled a drilling BHA with a 9⅞-in tricone bit, lowered it to the seafloor, and reentered Hole 1254B at 1716 hr on 24 October. After lowering the bit to the casing shoe, it took 1.5 hr to drill through the shoe. The hole was then cleaned to 4424 mbrf (237 mbsf) in preparation for deploying the CORK-II. The hole was then circulated from the bottom up and left with only seawater in it. The drill bit was pulled out of the hole and was back on the rig floor at 0445 hr on 25 October.

After some routine preventative maintenance (slipping and cutting the drill line), we started assembling the CORK-II. A screen, packer, 15 joints of 4½-in casing (230 m), umbilical, centralizers, and the wellhead made up the complete CORK-II. The wellhead was lowered to the moonpool doors, where the pressure data logger was tested; it was then lowered into the water to purge the hydraulic lines. At 1445 hr on 25 October, the CORK-II assembly was lowered to the seafloor and Hole 1254B was reentered with the CORK-II at 2050 hr. The 4½-in casing was lowered to 4366 mbrf (179 mbsf) when it encountered some resistance and began to take weight. The top drive was picked up so that we could jet the 4½-in casing in. The jetting process was hampered as a result of having to maintain the drill string pressure below 400 psi to prevent inflation of the packer.

After ~8 hr of attempting to jet the 4½-in casing in with the active heave compensator on at 0745 hr on 26 October, the top joint pin of the 4½-in casing failed through the last engaged thread. With the CORK-II wellhead still attached to the running tool, the vessel was offset to observe the reentry cone. At the time of the failure, the end of the pipe was ~10 m above the reentry cone. The broken end of the 4½-in casing was extending out of the reentry cone, but otherwise the reentry cone did not appear to have any observable problems. The CORK-II wellhead was retrieved and was back on the rig floor at 1645 hr on 26 October, ending Hole 1254B. The scientists decided to abandon efforts to deploy a borehole installation at this site and decided to move to Site 1255 (proposed Site 1043R).

The Site 1254 beacon was released at 1106 hr and was back on deck at 1221 hr on 26 October. The ship moved the ~1.1 nmi to Site 1255 in dynamic-positioning mode while the CORK-II wellhead was being recovered.

Return to Hole 1254B

After finishing operations at Site 1255, we moved back to Hole 1254B in dynamic-positioning mode to attempt to fish the screen, packer, and 4½-in casing that was left in Hole 1254B.

The vessel was positioned over Hole 1254B at 1721 hr on 2 November. A fishing BHA was assembled, consisting of a choker loop formed from wire rope slings, a rig-fabricated jet sub, five 8¼-in drill collars, one tapered drill collar, and the usual two stands of 5½-in drill pipe and a crossover sub.

The fishing tool was lowered to 4157 mbrf, and at 2343 hr on 2 November the 4½-in casing was snared. We applied 20,000 lb of overpull to the fish (4½-in casing), and it suddenly dropped off. When the snare was set, the end of the wire rope slings was too far below the end of the BHA for us to visually confirm if the fish was still there. Also, the total weight of the casing string being fished was too small to be distinguished on the weight indicator. The vessel was offset 0.5 nmi as the BHA was pulled out of the hole so that if the fish dropped off, it would not land back on the reentry cone. When the fishing BHA was back on the rig floor, the snare was empty and the casing was not recovered. When the ship was positioned back over the hole so that we could inspect the reentry cone with the VIT camera, we observed that the casing was still sticking out of the reentry cone. After the camera was back on deck and all equipment secured we began the transit to Balboa, Panama, at 1600 hr on 3 November. Leg 205 ended with the last line ashore at 1030 hr on 6 November.

F8. Stratigraphic log, Sites 1040 and 1254, p. 49.

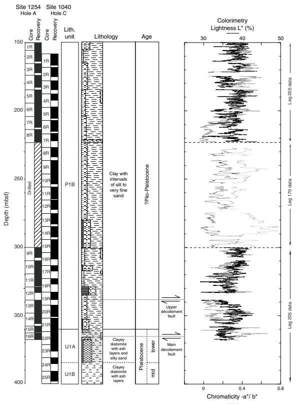

LITHOSTRATIGRAPHY

Site 1254 is located on the lower trench slope of the Costa Rica forearc; targeted coring was conducted to penetrate through a fault zone within the forearc prism, as well as through the plate boundary décollement and into the uppermost underthrust sediments close to the location of Site 1040. Figure F8 shows that the section recovered at Site 1254 overlaps with that sampled at Site 1040, spanning a sparsely dated sequence that is presumed to be Pliocene–Pleistocene in age (Shipboard Scientific Party, 1997b). The section recovered at Site 1254 largely comprises massive dark greenish gray claystones and silty claystones with minor volumes of interbedded volcanic ashes, fine sands, and silts. Figure F9 shows a typical example of the sediment facies, with a thin diffuse altered volcanic ash layer interbedded within homogeneous claystone. This example is from a relatively coherent piece of core, yet the sediments and sedimentary rocks recovered often show moderate to extreme degrees of drilling disturbance so that it is commonly difficult to tell if the absence of sedimentary structures in the cut core surface reflects a true absence in the original section or whether they were present but have been homogenized by drilling. Nonetheless, coherent fragments of more lithified sedimentary rocks do indicate that much of the section is either massive or slightly mottled, suggestive of moderate bioturbation. There is no evidence for strong bottom-current activity in the sediment depositional process at Site 1254.

F9. Altered volcanic ash, p. 50.

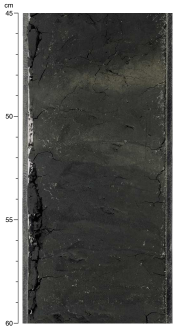

Although fine-grained sediment dominates the sequence, this material is typically not well sorted, with an array of clay, silt, and more rarely, fine sand grains visible to microscopic analysis (Fig. F10A). In addition, rare clasts of shallow-water carbonate rock are found as blocks in a muddy matrix. Together these characteristics suggest rapid deposition by way of debris or gravity flows as the dominant mode of sedimentation. There is a general trend downsection to more development of sandy layers. Cores 205-1254A-8R through 11R contain thin silty and sandy layers that are often strongly disrupted by drilling, with a soft sediment deformation character, indicating that the sediment was largely unconsolidated prior to recovery. Major coherent intervals of fine- to medium-grained sand were described in intervals 205-1254A-

F10. Recovered sediments, Site 1254, p. 51.

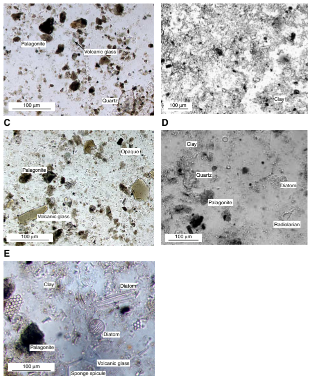

10R-4, 91–128 cm (315 mbsf); 12R-1, 37–52 cm (329 mbsf); 12R-3, 75–115 cm (333 mbsf); 14R-3, 85–97 cm (352 mbsf); 14R-7, 40–109 cm (356 mbsf); and 16R-4, 31–72 cm (367 mbsf). These sands are mostly massive and although subject to heavy drilling disturbance, especially in Cores 205-1254A-12R and 14R, the sand appears to have been partially lithified prior to recovery. Parallel laminations are noted locally (e.g., interval 205-1254A-12R-3, 74–91 cm) (Fig. **F11**), suggestive of current activity during deposition of at least that unit.

F11. Sandy interval with weakly formed parallel laminations, p. 52.

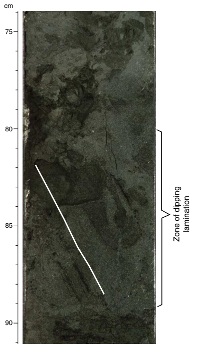

Smear Slides

The variation in lithology downsection can be broadly assessed from data derived from microscopic analysis of smear slides, presented graphically in Figure **F12** (see **"Site 1254 Smear Slides"**). The dominance of clay minerals within the sequence is readily apparent, as is the downcore decrease in volcanic ash. Variability in the sandy grade component is not well tracked by smear slide analysis, which tends to underestimate its abundance. The downhole increase in sand is more accurately shown by core description, shown in Figure **F8.** All samples showing abundant levels of volcanic glass are present above 250 mbsf, where the shards are usually found as very clear angular grains that have apparently not yet suffered heavy alteration (Fig. **F10B**). Volcanic material is, however, present at low (<10%) and moderate levels (<30%) in most of the sediment, sometimes still fresh (Fig. **F10C**) but also often heavily altered to palagonite or even zeolites deeper (>250 mbsf) in the section. In these cases, the grains show rounded geometries and are often cloudy in transmitted light. The continental provenance of the sediments cored in Hole 1254A is clear from the abundance of quartz and feldspar grains and also from the bright brownish red biotite mica flakes that are found at all stratigraphic levels. Biotite composes <5% of the total sediment mass. The quartz and feldspar grains are partially delivered to the forearc by volcanic ash fall, but the subrounded character of many of the grains indicates that these have experienced significant transport and are largely reworked from terrestrial source terrains, which themselves are mostly volcanic.

F12. Smear slide data, Sites 1254 and 1040, p. 53.

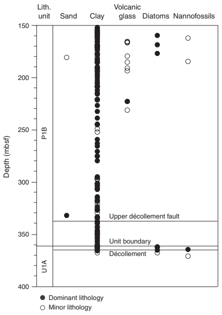

The biogenic component of the sediment is very low (<5%) and restricted to occasional nannofossils above 200 mbsf and below 360 mbsf. More significantly, below Section 205-1254A-15R-2, 142 cm (360.62 mbsf), the proportion of diatoms increases sharply (>10%) (Fig. **F10E**). The appearance of diatoms is considered important for understanding the structure of the forearc prism because the uppermost sedimentary unit in the subducting Cocos plate stratigraphy (Subunit U1A) recorded high percentages of diatom abundance (Shipboard Scientific Party, 1997a). It should be noted that although 360.62 mbsf marks the clearest lithologic break between underthrust and forearc wedge sediments, the structural base of the décollement lies at 364.2 mbsf (see **"Structural Geology,"** p. 20). Although diatom abundance increases most sharply below 360 mbsf, it should be noted that diatoms forming up to 2%–3% of the total sediment are noted in sediments from Core 205-1254A-14R (Fig. **F10D**). Although this may indicate a structural break higher in the section, we suggest that it could instead reflect either original sediment variability within the forearc wedge strata or a tectonic interleaving of underthrust sediment above the principal boundary.

The downsection transition from diatom-free to diatom-rich sediment noted in the smear slides lies just above the décollement and represents a passage from forearc wedge sediment into sediment originally deposited on the Cocos plate in the Middle America Trench. In the core, the lithologic break is seen as a slight change of color from a dark-colored more clay-rich sediment above to a lighter more silty claystone below (Fig. F5).

Redeposited Blocks

Evidence for significant downslope resedimentation in the sediments above the lithostratigraphic unit boundary at 360 mbsf occurs in the form of occasional blocks of strongly lithified tan-colored carbonate rock (e.g., Fig. F13). The most prominent examples are found in intervals 205-1254A-7R-4, 42–45 cm (208.72 mbsf); 7R-4, 52–55 cm (208.82 mbsf); and 14R-CC, 20–23 cm (356.06 mbsf). The blocks are angular and <3 cm thick. Under microscopic thin section analysis, the lithologies present in the cobble recovered in Sample 205-1254A-14R-CC, 20–23 cm, were revealed to be a peloidal limestone interbedded with a micritic cemented sandstone. Figure F14A shows the peloids with no micritic matrix but instead a sparry calcite cement that shows the fanning pattern characteristic of precipitation with a fully saturated subtidal environment (Fig. F14C) (Flügel, 1982). The lack of dissolution of the peloids and the regular form of the calcite spar laths argues against significant flow of the pore fluid during cementation. The lack of a muddy matrix indicates that sedimentation occurred in a current-swept setting, whereas the lack of compaction of the peloids, typically interpreted as fecal pellets from shrimp or crablike organisms, constrains cementation and lithification to have occurred early after deposition and before burial compaction could occur. Such pelsparite limestone facies are most common in shallow shelf regions, above storm wave base, and below the intertidal zone (i.e., ~10–30 m water depth) (Wilson, 1974).

F13. Light tan cobble of limestone, p. 54.

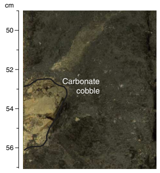

F14. Photomicrographs from a cobble of carbonate, p. 55.

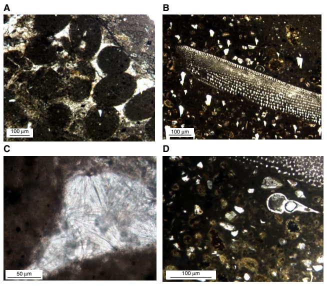

Further evidence for a shallow-water depositional environment is found in the identification of shallow-water bivalve shell fragments (Fig. F14B) and small gastropods (Fig. F14D), found within a medium-grade sandstone. This sandstone is composed largely of grains of altered volcanic rock with a significant subsidiary component of quartz and is well sorted, consistent with a current-swept shallow marine setting. The lithified carbonate cobbles are interpreted as having been transported as coherent clasts within muddy debris flows into the trench from their origin within the coastal zone. The enclosing muddy matrix sediments must represent debris flow deposits in which these blocks were carried into the lower trench slope area. Thus, the carbonate cobbles confirm the hypothesis that the section is dominated by reworked gravity and debris flow units, rather than being the product of a gentle hemipelagic rain and earlier accretion to the forearc wedge.

Tephra Layers

Compared to the sequence of well-preserved tephra found at Sites 1039 and 1253 on the subducting Cocos plate, little well-preserved tephra stratigraphy is found at Site 1254. Although occasional thin altered ash layers are recognized, they are rare, typically <2 cm thick and often completely altered to claystone. More coherent volcanic ash layers recognized in the core are listed in Table T2. Tephras are mostly seen in the upper cored intervals (155–215 mbsf) and are either structureless bands or occasionally show normal grading. The original volcanic glass shards are often altered to palagonite. Volumetrically the tephra represent <1% of the total section. However, much larger volumes of vol-

T2. Location of the major tephra layers, Site 1254, p. 93.

canic detritus falling in the forearc appear to be largely reworked into the dominant silt-clay sediment. Given the relative lack of evidence for bioturbation, we suggest that much of this reworking occurs during debris flow events that emplace the bulk of the section.

Two larger coherent ash layers were recovered at Site 1254. The thinner unit is identified in interval 205-1254A-5R-8, 14–20 cm (193.49 mbsf), and is marked by being light gray, homogeneous, and quite deformed by drilling. The larger tephra is a reverse-graded layer, recovered in Sample 205-1254A-8R-8, 22–65 cm (222.37–222.80 mbsf) (Fig. F15). This is colored light gray in its basal section and grades into lighter greenish gray coarse sand–grade material toward the top, where it has a sharp contact with the overlying dark greenish gray claystone. Both of the thicker ashes preserve relatively fresh glass shards and are interpreted as the product of primary air fall deposition, followed by settling through the water column.

F15. Major siliceous tephra layer, p. 56.

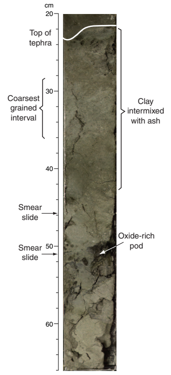

The base of the tephra recovered in Sample 205-1254A-8R-8, 22–65 cm, was not recovered because this bed was at the base of Core 205-1254A-8R, the last core taken in the upper cored interval at this site. The study of available core results in a minimum thickness estimate of 43 cm. Because Site 1254 is ~150 km from the nearest arc volcano, this thickness at this range indicates that this must have been a very large eruption. For comparison, the 1980 eruption of Mount Saint Helens resulted in a tephra <2 cm thick at a distance of 150 km (Sarna-Wojcicki et al., 1981). The Site 1254 ash exceeds the Pleistocene eruption of Crater Lake that deposited the Mazama ash layer, which is only ~10 cm thick at a range of 150 km (Williams and Goles, 1968). The Minoan ash from Santorini Volcano provides the closest analog in being 25 cm thick at this distance from the source (Watkins et al., 1978).

Given the incomplete recovery of the tephra in Sample 205-1254A-8R-8, 22–65 cm, a more meaningful comparison between tephra can be made using grain size data. Grains within this unit are up to 400 µm in diameter with a median of ~100 µm. Following Ninkovich et al. (1978), the maximum grain size relative to the distance from the eruption location implies an eruption event comparable to or slightly larger than that which emplaced the Minoan tephra from Santorini Volcano (Fig. F16A). A comparison of the median grain size to the distance from the eruptive center shows that the tephra in Sample 205-1254A-8R-8, 22–65 cm, represents a large event, but one that is less than the predicted upper limit for terrestrial volcanism defined by Walker (1971). Consequently, we conclude that the tephra in Sample 205-1254A-8R-8, 22–65 cm, represents deposition from a very large event, yet one that is resolvably less powerful than the greatest known events, such as the Toba Volcano eruption (Sumatra, 75 ka). Because the section at Site 1254 is not dated by biostratigraphy or paleomagnetic work, we cannot unambiguously correlate this layer with any of the tephra found at Sites 1039 and 1253.

F16. Tephra grain size comparisons, p. 57.

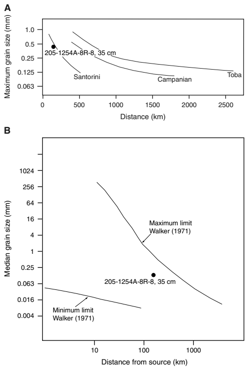

Sediment Geochemistry

Major and trace element analyses of 15 sediment samples and 1 volcanic ash were conducted aboard the ship following the methods described in "Inorganic Geochemistry," p. 24, in the "Explanatory Notes" chapter. Major, minor, and trace element analyses are presented in Table T3. The tephra was run on the ICP-AES separately from the sediments, and the results are discussed below. Analyses were made on freeze-dried bulk samples that are a mixture of sediment particles and

T3. Bulk geochemical analysis of sediments and tephra, p. 94.

sea salts (see **"Inorganic Geochemistry,"** p. 24, in the "Explanatory Notes" chapter). The data have not yet been corrected for porosity and pore water contribution to the bulk sediment composition.

The ICP-AES geochemical data at this forearc site can be useful for (1) assessing whether the sediments in the overthrust wedge are similar to those in the subducting section and testing models for sediment accretion; (2) determining the degree of chemical heterogeneity in the wedge; and (3) constraining the provenance of the clastic sediments composing the wedge.

Figure **F17** shows variations in TiO_2, Al_2O_3, SiO_2, and Ti/Al with depth below seafloor. Volcanic detritus is nearly ubiquitous at low concentrations in much of the sediment recovered, and the tephra analyzed at Site 1254 has much lower aluminum and titanium concentrations than the surrounding wedge sediments. This distinction suggests that reworked tephras may account for only a relatively moderate proportion of the total sediment in the wedge.

F17. Depth profiles for TiO_2, Al_2O_3, SiO_2, and Ti/Al, p. 58.

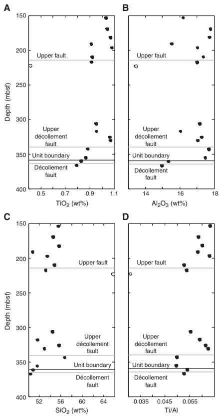

Major element compositions are seen to change across the lithostratigraphic boundary from wedge to underthrust sediment. Although the alkali elements show little variability overall (Fig. **F18**), there is a slight decrease in TiO_2, Al_2O_3, and SiO_2 below the lithostratigraphic unit boundary. Within the range of elemental values recorded at Site 1040, these changes are small but likely reflect the higher proportion of biogenic hemipelagic material in the underthrust Subunit U1A compared to the more clastic sedimentary rocks in Subunit P1B (Fig. **F8**). Higher silica concentrations in the wedge may signify more advanced diagenesis because the formation of clay minerals and zeolites resulting from volcanic glass alteration will tend to concentrate silica. The internal silica source from diatoms may, however, supply the needed silica. The shift to generally higher potassium in the sediments of the wedge may also be consistent with this process (Fig. **F18**). Within the wedge the major element chemistry is remarkably constant, a characteristic also noted at Site 1040 (Shipboard Scientific Party, 1997b). The lack of variation is interpreted to indicate a relatively uniform sediment type with little interbedded biogenic sediment. The sediment is likely derived from the same source throughout the time of deposition and has experienced a large degree of homogenization during emplacement, as might be expected from the debris flow depositional process favored on the basis of the sedimentary structures and grain size character.

F18. Depth profiles for Na_2O and K_2O, p. 59.

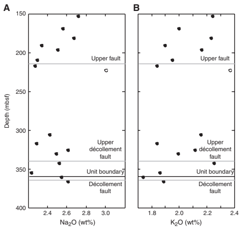

Figure **F19** plots CaO, MgO, Sr, and Ba against depth for the sediments and volcanic ash at Site 1254. Levels of CaO and Sr remain constant with depth, suggesting a relatively constant low proportion of carbonate content throughout the wedge and top of the underthrust section. The lithostratigraphic unit boundary at 360 mbsf is best highlighted in terms of the trace element Ba, as also recognized at Site 1040. Ba rises sharply below 360 mbsf. Although higher concentrations of Ba are sometimes attributed to the presence of volcanic materials in the sediment, the evidence from the SiO_2 and K_2O concentrations instead favors higher volcanic influence in the wedge (Subunit P1B). Smear slide analysis did not identify a large increase in volcanic material below the level of the lithostratigraphic unit boundary. Consequently, we interpret the increased Ba concentration in the sediment below 360 mbsf (Subunit U1A) as a function of higher barite content in the hemipelagic units.

F19. Depth profiles for CaO, MgO, Sr, and Ba, p. 60.

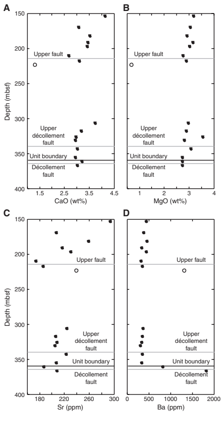

Tephra Geochemistry

Major and trace element analyses of a single tephra (Sample 205-1254A-8R-8, 22–65 cm) are presented in Table **T3.** The volcanic glass appeared fresh under microscope inspection, suggesting that the bulk sediment analysis should be close to a melt composition. Although the analytical total only just exceeds 92%, this may not necessarily imply strong alteration because the magmatic water content of high silica arc glass can reach up to ~5% (Burnham and Jahns, 1962), meaning that only ~3% of the missing total may be attributable to postdepositional hydration. In terms of its major elements, the tephra in Sample 205-1254A-8R-8, 22–65 cm, is classified as a dacite using the scheme of Cox et al. (1979) and as a subalkalic magma under the classification of Miyashiro (1978). The geochemical discrimination plots of Middlemost (1975) show that whereas the ash is calc-alkaline, it is sufficiently K_2O rich to be classified as medium K in that scheme (Fig. **F20**). These basic characteristics are consistent with the presumed source of the tephra in the volcanic front of Costa Rica.

F20. Discrimination plots for tephra, p. 61.

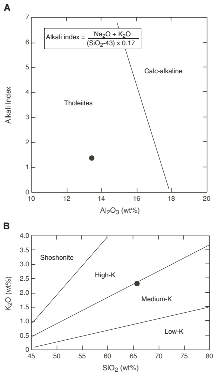

Diagenesis

Diagenesis appears to have proceeded to only a moderate degree at Site 1254, with the exception of the well-cemented redeposited carbonate blocks, which experienced early diagenesis further upslope. No soupy sediment was recovered, and the sediment was typically lithified, while still being easy to scratch or gouge with metal instruments (i.e., a chalk-type consolidation). Clearly some cementation had occurred, as evidenced by the recorded brittle deformation of the sediment (e.g., the development of polished joint planes, crosscutting original bedding fabric). Such features are detailed in **"Structural Geology,"** p. 20. Nonetheless, some of the sand units (e.g., intervals 205-1254A-10R-4, 91–128 cm; 315 mbsf) show strong plastic drilling disturbance that is incompatible with a lithified state prior to drilling over certain intervals above the décollement.

Cores 205-1254A-11R through 14R (319–357 mbsf) show development of occasional carbonate concretions that are often focused on burrow structures. These tan-colored bodies are irregular, usually >5 cm in diameter, and show a similar degree of consolidation as the surrounding sediment, unlike the redeposited carbonate blocks (Fig. **F21**). Rare authigenic pyrite is restricted to the upper cored section (150–185 mbsf) where it is present as tiny (<20-µm diameter) irregular grains dispersed in the claystones.

F21. Carbonate concretions within the dominant claystone lithology, p. 62.

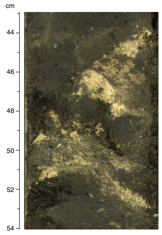

X-Ray Diffraction Analysis

The combined results of X-ray diffraction (XRD) analyses of randomly oriented bulk sediment powders from Sites 1040 and 1254 are presented. Shipboard Leg 170 XRD data were not evaluated previously, nor were mineral peaks identified. Data from Leg 170 diffractograms were analyzed for the first time during Leg 205 and are interpreted and discussed here. Site 1040 peak intensity and peak area data are listed in Table **T4,** with peak area ratios listed in Table **T5.** Site 1254 peak intensity and peak area data are listed in Table **T6,** and the corresponding peak area ratios are listed in Table **T7.**

Cristobalite/quartz peak area ratio data have been used to monitor opal transformation during diagenesis (e.g., Mitsui and Taguchi, 1977)

T4. XRD analysis of bulk powder sediment samples, Site 1040, p. 95.

T5. Peak area ratios of dominant minerals, Site 1040, p. 97.

T6. XRD analysis of bulk powder sediment samples, Site 1254, p. 99.

T7. Peak area ratios of dominant minerals, Site 1254, p. 101.

because the proportion of cristobalite is known to increase with temperature (e.g., Gambhir et al., 1999). The cool borehole temperatures (<10°C at the base) encountered at Site 1254 are below those required for in situ formation of cristobalite in this location. Volcanic ash diagenesis to cristobalite could be an alternative source. The origin of the cristobalite in Subunit U1A is not resolvable based on the existing analyses aboard the ship. However, the difference in cristobalite/quartz ratios between prism and underthrust units is notable; the average peak area ratio in the prism units is 0.68, and the average peak area ratio in the two uppermost underthrust units is 1.05. This difference suggests little or no accretion of hemipelagic sediments in Subunit U1A into the forearc wedge.

Clay Mineralogy

Clay separates were obtained for nineteen sediment samples from Hole 1254A. Oriented aggregate slides were generated as described in **"Lithostratigraphy,"** p. 4, in the "Explanatory Notes" chapter. Figure F22 presents relative weight percentages for smectite, illite, and kaolinite in the samples; Tables T8 and T9 portray the peak intensity and peak area data and calculated relative weight percentages for the three clay minerals considered.

F22. Relative abundances of smectite, illite, and kaolinite/chlorite based on X-ray diffraction analyses, p. 63.

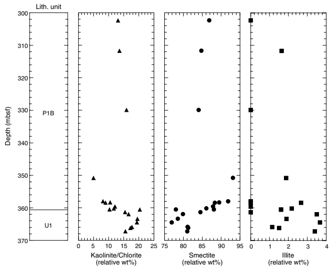

Relative weight percentages of smectite, illite, and kaolinite/chlorite in the clay splits vary downhole. Smectite ranges from 77 to 93 wt%, illite ranges from 0 to 3.67 wt%, and kaolinite/chlorite ranges from 5 to 20 wt%. The maximum proportion of smectite (93 wt%) occurs at 350.81 mbsf in Sample 205-1254A-14R-3, 0–40 cm, taken from interstitial water squeeze cake trimmings. The maximum percentage for illite (4 wt%) occurs at 364.5 mbsf in Sample 205-1254A-16R-2, 20–21 cm (noted in **"Structural Geology,"** p. 20) in part of a brittle shear zone. The maximum percentage for kaolinite/chlorite (20 wt%) occurs at 360.55 mbsf in Sample 205-1254A-15R-3, 0–44 cm, taken from interstitial water squeeze cake trimmings.

T8. 17-Å smectite, 10-Å illite, and 7-Å kaolinite/chlorite peaks, p. 102.

T9. Calculated smectite, illite, and kaolinite, Site 1254, p. 103.

Summary

The sediments and sedimentary rocks recovered at Site 1254 are dominated by structureless claystones with variable subsidiary quantities of silt and rare interbedded volcanic ashes and sandstones. Below 360 mbsf, these sediments contain abundant diatoms and are assigned to a different lithostratigraphic unit, interpreted to represent Cocos plate hemipelagic sediment underthrust under the forearc wedge. Redeposited blocks of shallow-water limestones, lithified prior to incorporation within mudstones, are consistent with sedimentation by fluidized gravity and debris flows. Sediment provenance indicates erosion of volcanic and quartz-mica-bearing basement rocks onshore, with no evidence for the incorporation of hemipelagic sediments into the forearc wedge.

A single large tephra was identified in Sample 205-1254A-8R-8, 22–65 cm, characterized by chemistry consistent with a source within the Costa Rica arc volcanic front. Grain size and thickness characteristics of the tephra indicate that it was the product of a giant eruption similar in size to that associated with the Minoan tephra of Santorini Volcano. The age of the deposit is unknown.

STRUCTURAL GEOLOGY

Coring at Site 1254 targeted two different structural domains based on coring and logging while drilling at Site 1040: (1) a zone from 150 to 223 mbsf, containing fractured and locally steepened bedding within the prism, described as the prism fault zone and (2) the basal décollement zone from 300 to 368 mbsf. The deformation structures observed in these intervals are summarized, along with lithostratigraphy, in Figure F23. All structural data are given in Table T10. Core descriptions of deformation including breccia size, foliation (if present), hardness of breccia clasts, and the presence of polished surfaces are also shown.

Prism Fault Zone

The concentration of deformation structures at ~180 mbsf at Site 1040 (Kimura, Silver, Blum, et al., 1997) and the clear sheared nature of that horizon (Vannucchi and Tobin, 2000) mark the presence of a fault zone, associated with a strong geochemical anomaly (Kimura, Silver, Blum, et al., 1997). This interpretation was confirmed by coring in Hole 1254A from 150 to 223 mbsf (Fig. F23). Structural observations in poorly lithified material require high-quality cores. Because Cores 205-1254A-1R through 2R were heavily disturbed by drilling, structural data were collected starting at a depth of 165.10 mbsf (Core 205-1254A-3R). The entire recovered interval is characterized by deformation, consisting of stratal disruption, foliated breccia with fragments as small as a few millimeters in length, brittle shear zones, deformation bands, and inclined bedding (Fig. F24). There is no unequivocal evidence that the stratal disruption and the deformation bands are natural rather than drilling induced. The intensity of deformation, particularly brecciation and brittle shearing, increases downward, reaching a peak in the interval from 215.95 to 216.40 mbsf (interval 205-1254A-8R-2, 105–150 cm) (Fig. F23). Deformation is not continuous but is localized along preferentially sheared horizons that range in thickness from 2 m to 20 cm. The distribution of sheared and brecciated zones with depth is depicted in Figure F23. Reidel shears within a 24-cm-thick, exceptionally well preserved foliated breccia (interval 205-1254A-8R-5, 0–24 cm) indicates reverse displacement consistent with the results from Site 1040 (Vannucchi and Tobin, 2000). Paleomagnetic reorientation of the shear zone shows that it dips to the northeast (Fig. F25). This is the only shear zone among those encountered in the recovered sediments for which paleomagnetic reorientation yields a reliable geometry. Given the complexity of the prism, particularly in three dimensions, the relationship between the fault zone observed here at 210–220 mbsf and that encountered at 180–190 mbsf at Site 1040 cannot be uniquely established.

Décollement Zone

Coring of the décollement zone started after washing from 223 to 300 mbsf, and well-preserved structural features can be observed beginning with Core 205-1254A-11R, corresponding to a depth of 319.30 mbsf (Fig. F23). The cores typically exhibit significant drilling disturbance, like that encountered and described during Leg 170 as "spiraliferous" (Kimura, Silver, Blum, et al., 1997), consisting of rotation and continuous torque of clay-rich sections. Despite the drilling disturbance, some bedding plane orientations were recorded (Fig. F26). Bed-

F23. Structural and lithologic summary, p. 64.

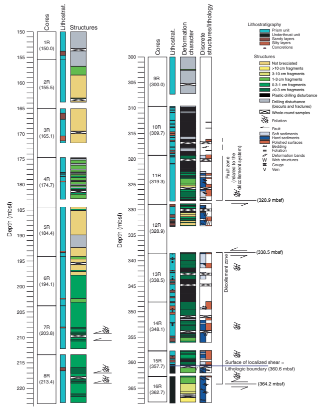

T10. Summary of structural data, Site 1254, p. 104.

F24. Bedding dips and bedding azimuth in the prism fault zone, p. 65.

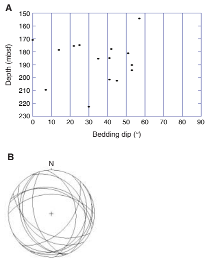

F25. Foliation and Riedel shear surfaces, p. 66.

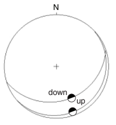

F26. Bedding dips and bedding azimuth in the décollement zone, p. 67.

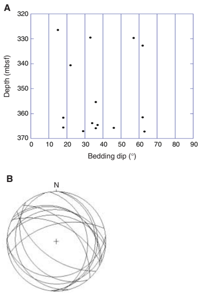

ding and fissility dips are varied, indicating heterogeneous deformation (Fig. F26A), but paleomagnetic reorientation of the features, where possible (Fig. F26B), shows that they consistently dip northeast or southwest, parallel to the trench strike. The entire recovered section from 319.30 to 367.96 mbsf is characterized by intense deformation. A comparison with less-deformed sediments away from the fault zone was not possible because coring was only conducted in the fault zone. There are, however, small changes with depth in the fault zone that define a detailed structural "stratigraphy" and distinguish different subdomains within it (Fig. F23). The heterogeneity of the deformation is the most striking feature (Fig. F23), and the degree of brecciation, usually associated with a strong foliation, allows division of the recovered interval into two zones. The upper zone from 319.30 to 328.90 mbsf is characterized by generally increasing brecciation with depth, with breccia fragments <0.3 cm. One exception is in the interval between 323.76 and 324.15 mbsf (interval 205-1254A-11R-4, 23–62 cm), where there are fragments up to 5 cm (Fig. F27). Foliation is common throughout Core 205-1254A-11R, resulting in a clear alignment of clasts, except for the above-mentioned zone with larger fragments that are equidimensional but internally strongly foliated.

F27. Equidimensional breccia, p. 68.

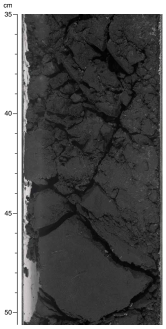

Below 324.15 mbsf (Core 205-1254A-12R), deformation sharply decreases and consolidated and coarsely brecciated (fragments >10 cm) sand layers are common. These sandstone layers contain dipping lamination and rare web structures. This well-defined change in deformation intensity marks the top of a relatively less deformed rock volume, which can be interpreted in two ways: (1) it may mark a basal décollement zone starting at 338.5 mbsf, underlying a separate fault identified at a depth of 319.30–328.90 mbsf. This interpretation suggests a more articulated geometry for the décollement system than that described at Site 1040 (Kimura, Silver, Blum, et al., 1997; Tobin et al., 2001). (2) Alternatively, this horizon of less-deformed sand layers could reflect rheologic differences between the different lithologies within a single, thicker décollement zone—although sand-rich sections of cores have been strongly deformed deeper in the fault zone, suggesting that this interpretation is less plausible (Fig. F23).

Following interpretation 1 above, the upper boundary of the décollement zone is defined by increasing deformation intensity beginning in Core 205-1254A-13R at 338.5 mbsf. The exact location of the décollement upper boundary is difficult to place, mainly because the deformation gradually increases in intensity toward zones of concentrated shear and no sharp discontinuity is observed between Cores 205-1254A-12R and 13R.

The décollement zone itself is heterogeneous, with a general downward increase in brecciation intensity, breccia fragment aspect ratio, and hardening of the sediments. Despite the high recovery, spiraliferous drilling disturbance affects the cores, although less extensively than at Site 1040. Unlike Site 1040, a concentration of spiraliferous disturbance is not present in the lowermost part of the décollement zone. In zones of intense brecciation, breccia fragments are characterized by polished surfaces; the development of scaly fabric is probably precluded by the abundant silt and sand in the sediments. From 354.78 to 355.86 mbsf, sandstone layers are brecciated and foliated. At 360.60 mbsf, the appearance of diatoms in the sediments marks the lithologic boundary between the prism and the hemipelagic units (Fig. F5). The lithologic boundary underlies 50 cm of finely brecciated sand and 10 cm of highly sheared clay, possibly indicating a surface of ductility contrast that appears as a major structural discontinuity.

The hemipelagic sediments below the lithologic boundary are also deformed and brecciated and contain aligned clasts with a strong internal foliation (Fig. F6). Deformation decreases with depth and becomes discrete at 364.2 mbsf, localized along 3- to 8-cm-thick brittle shear zones characterized by gouges or Riedel shears (Fig. F7). These brittle shear zones consistently exhibit a normal sense of displacement and landward dips when reoriented to true geographical coordinates (Fig. F28). As defined by the criteria discussed above, the hemipelagic sediments above the zone at 364.2 mbsf are also deformed by normal faults, a few of them present as conjugate features. The change in deformation style and intensity within hemipelagic sediments at 364.2 mbsf is interpreted as the base of the décollement zone. The décollement zone at Site 1254 has a vertical thickness of 25.7 m. Because the recovered interval at Site 1254 does not contain intact or mildly deformed sediments, the geometry of any structurally higher faults that may be part of the décollement system in Hole 1254A cannot be determined. The complex geometry of the décollement system at this site contrasts with that described at Sites 1040 and 1043, where the top of the décollement coincides with an increase in brecciation, and the lithologic boundary between the prism and the hemipelagic unit is coincident with the base of the décollement.

F28. Brittle shear zone boundaries, p. 69.

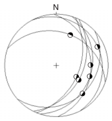

PHYSICAL PROPERTIES

At Site 1254, laboratory measurements were made to provide a profile of physical properties across a fractured interval (150–223 mbsf) and the décollement (300–367 mbsf), both previously cored in Hole 1040C, which is located 15 m to the east. All cores were initially passed through the multisensor track (MST) before being split. Gamma ray attenuation (GRA) bulk density, noncontact electrical resistivity (NCR), and volumetric magnetic susceptibility measurements were taken at 2-cm intervals, with measurements averaged from three separate 1-s data acquisitions for all cores. *P*-wave velocity logger measurements were not taken because of the small and variable diameter of RCB cores that generally leads to poor coupling between the core liner and recovered core. Natural gamma radiation (NGR) was counted every 10 cm for 20-s intervals. Drilling disturbance and gas expansion cracking were noted in all cores and degraded the volumetric magnetic susceptibility and GRA bulk density MST measurements. As at Site 1253, data collected with the NCR instrument exhibited significant scatter, and measured resistivity values were consistently unreasonably low compared to measurements from Leg 170, suggesting a problem with the instrument or its calibration. These data will not be discussed further. No *P*-wave velocity or thermal conductivity measurements were made at this site, because the cores were too fractured and disturbed to obtain *P*-wave arrivals using the *P*-wave velocity sensor system, and the cores were unsuitable for either the full-space or half-space thermal conductivity probes.

Moisture and density samples were selected from undisturbed core at regularly spaced intervals of two per section (75-cm resolution). Measurements of dry volume and wet and dry mass were uploaded to the ODP Janus database and were used to calculate water content, bulk density, grain density, porosity, void ratio, and dry bulk density. Calculated physical property data are available from the ODP Janus database for all MST and moisture and density measurements.

Density and Porosity

In the interval from 150 to 223 mbsf (Cores 205-1254A-1R through 8R), porosity determined from moisture and density measurements decreases from values of 47%–58% near its top to 39%–51% at its base, and bulk densities increase from 1.71–1.88 to 1.82–1.93 g/cm³ (Fig. F29A, F29B). Several porosity and bulk density values at ~200 mbsf deviate significantly from the overall trend in the interval from 150 to 223 mbsf (Fig. F29A, F29B). These porosity and bulk density values can be attributed to error in grain density determinations on these moisture and density samples (see discussion below).

In the interval from 300 to 362 mbsf (Cores 205-1254A-9R through 15R), porosity remains generally uniform but scattered, ranging from 42% to 55%, and increases abruptly to 57%–60% in the interval from 362 to 367 mbsf (Core 16R). Bulk density ranges from 1.87 to 2.05 g/cm³ between 300 and 362 mbsf and decreases to 1.63–1.71 g/cm³ from 362 to 367 mbsf. Both porosity and bulk density values from Site 1254 are consistent with those from Hole 1040C (Leg 170), located 15 m to the east (Fig. F29A, F29B).

When viewed in detail, porosities and bulk densities within the structurally defined décollement zone (338.5–364 mbsf) are scattered but appear to correlate with core observations (Fig. F29C, F29D). In parts of the fault zone characterized by “spiral” drilling-induced fabric, porosity is generally lower (~40%–45%, corresponding to bulk densities of 1.92–2.03 g/cm³) than in portions of the fault zone characterized by brecciation (~50%–55%, corresponding to bulk densities of 1.76–1.84 g/cm³) (see **“Structural Geology,”** p. 20). Porosity also decreases abruptly to ~42% within a small zone at 361 mbsf, identified in the core description as both the lithologic boundary between older prism sediments and Pleistocene diatomaceous claystone (termed Unit “U1” at Sites 1039, 1043, and 1040) (Kimura, Silver, Blum, et al., 1997) and a zone of localized shear (see **“Structural Geology,”** p. 20).

GRA densities show significant scatter throughout both cored intervals, probably a result of core expansion and cracking due to gas. The highest values of GRA density are consistent with those determined from moisture and density properties and exhibit the same sharp decrease at 362 mbsf as seen in moisture and density data (Fig. F30).

Grain densities determined from dry mass and volume measurements generally range from 2.62 to 2.94 g/cm³, which are significantly greater than values of 2.40 to 2.65 g/cm³, measured at Site 1040 (Fig. F31) and also higher than that expected for most marine sediments. Grain densities determined at Site 1254 also show considerably more scatter than those from Site 1040. To evaluate the effect that possibly erroneous grain density determinations had on calculated porosity and bulk density values shown in Figure F29A and F29B, porosity and bulk density were recalculated using a constant grain density of 2.65 g/cm³, the mean value measured in samples from Site 1040 (Fig. F32A, F32B). The general shift in grain densities between Sites 1254 and 1040 and the scatter in grain densities at Site 1254 have a negligible effect on calculated porosity and bulk density values (Fig. F32A, F32B). However, several grain density determinations at ~200 mbsf, with values ranging from 1.70 to 2.25 g/cm³, deviate significantly from values above and be-

F29. Porosity and bulk density, p. 70.

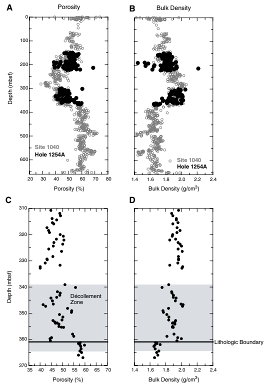

F30. GRA and moisture and density bulk densities, p. 71.

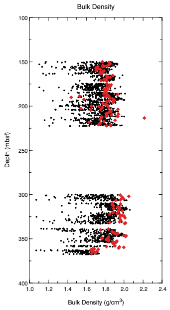

F31. Grain densities, p. 72.

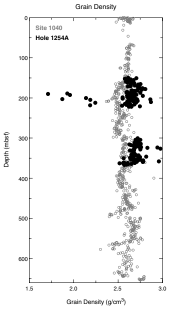

F32. Porosity and bulk density using determinations from Site 1254, p. 73.

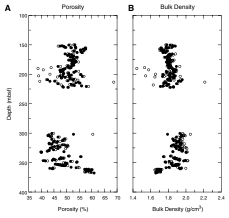

low and do affect calculated porosity and bulk density in this interval (Figs. F29A, F29B, F32).

Dry volumes for the outliers in grain density near 200 mbsf were all measured in the same pycnometer cell, suggesting a probable miscalibration of this cell. The generally high (>2.70 g/cm^3) grain densities at Site 1254 also suggest analytical error, most likely in dry volume measurement, but a specific instrumental problem has not been found.

Natural Gamma Radiation

NGR results are presented in counts per second (cps) (Fig. F33). The background, produced by Compton scattering, photoelectric absorption, and pair production (12.95 cps), was measured at the beginning and during MST runs for each core section and subtracted from the measured gamma ray values to obtain corrected counts. NGR results are relatively uniform and scattered from 9.5 to 20 cps throughout the cored intervals above 362 mbsf, with the exception of three zones characterized by several measurements of significantly higher values (21–32 cps) at 204–207, 218–223, and 300–303 mbsf. NGR values increase abruptly across the lithologic boundary at 362 mbsf, from 9–20 cps above to 18–33 cps below.

F33. Corrected MST NGR measurements, p. 74.

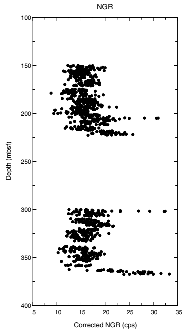

Magnetic Susceptibility

Volumetric magnetic susceptibility measured with the MST shows generally low values from 150 to 223 mbsf, with one excursion toward higher values between 180 and 195 mbsf (Fig. F34). Below 312 mbsf, magnetic susceptibility is highly variable, with two pronounced peaks at 320 and 340 mbsf. Some of the peaks in magnetic susceptibility between 312 and 367 mbsf correspond to sand layers noted in core description (see "Lithostratigraphy," p. 13), whereas others do not.

F34. MST volumetric magnetic susceptibility, p. 75.

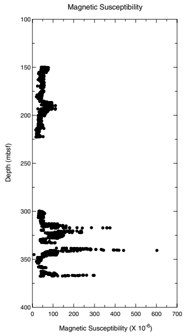

Summary and Discussion

Porosities and bulk densities at Site 1254 exhibit trends similar to those seen in Hole 1040C, located 15 m to the east (Fig. F29A, F29B). Variations in porosity and density within the structurally defined décollement zone correlate with core descriptions: in general, zones of lower porosity (40%–45%) correspond to zones characterized by "spiral" deformation interpreted as drilling disturbance; zones of higher porosity (50%–55%) correspond to zones characterized by brecciation. Porosity is also low (42%–44%) between 358 and 361 mbsf, within and adjacent to a zone of localized shear (see "Structural Geology," p. 20). Porosity increases and bulk density decreases sharply below 362 mbsf across the lithologic boundary between prism sediments and Pleistocene diatomaceous claystone. A systematic error resulting in unreasonably high grain densities, with an average of 2.84 g/cm^3, results in only a small error in calculated porosities and bulk densities (Fig. F32).

MST NGR counts are generally uniform throughout the cored intervals above 362 mbsf and exhibit a sharp increase from 9–20 cps above the lithologic boundary to 18–32 cps below. MST magnetic susceptibility data are generally low and uniform in the interval from 150 to 223 mbsf, with one peak at 180–195 mbsf. In the lower cored interval below 312 mbsf, magnetic susceptibility is characterized by highly variable values and several distinct peaks. Some of these peaks correlate with sand layers noted in core description, but the cause of other peaks in magnetic susceptibility in this interval is unclear.

PALEOMAGNETISM

Paleomagnetic measurements on archive-half sections were routinely performed. After measuring NRM, all sections were continuously demagnetized using alternating-field (AF) demagnetization up to 40 mT in increments of 10 mT at 2.5-cm intervals in order to remove magnetic overprints and to provide reorientation for intact pieces in the sedimentary cores. An AF demagnetization of 5 mT was occasionally applied in the demagnetization sequences to investigate drilling-induced isothermal remanent magnetization.

Two or three discrete samples were collected from each working-half section for analyses of postcruise rock magnetism and paleomagnetism. The samples were picked from intact pieces and in the region of clear sedimentary structures. All discrete samples will also be used to aid in the paleomagnetic interpretation of the archive sections' record of magnetization by providing additional measurements of polarity and basic magnetic characterization. The discrete samples were demagnetized up to 80 mT in 5-mT increments to permit principal component analysis.

Magnetic susceptibility of all archive-half sections were also measured every 2 cm by a point susceptibility sensor on the archive multisensor track (AMST). The "high-resolution mode (0.1 range)" of the point sensor measures susceptibility within short intervals of the sections better than the loop sensor of the MST.

Paleomagnetism

The majority of the NRM measurements for archive sections show steep inclinations of ~60° to ~80°N. These steep inclinations partially disappeared in a weak AF demagnetization level of 5 mT. Then several negative inclinations appear after a demagnetization of 10 mT, which suggests that the NRM inclination represents drilling-induced magnetic overprints (Fig. F35). After AF demagnetization of 40 mT, magnetic inclinations of cored sediments show several polarity changes (Figs. F36, F37) that were compared to previous paleomagnetic results at Site 1040 (Kimura, Silver, Blum, et al., 1997). However, construction of magnetostratigraphy and age identification of magnetic polarities in Hole 1254A is not possible because of high variation of the magnetic inclination. Also, scattered magnetic declination data suggest pervasive drilling disturbance in the sediments (Figs. F36, F37). Structural core observation found "spiral" drilling disturbance in several cores at this site (see **"Structural Geology,"** p. 20). Additionally, previous work in Hole 1040C identified continuous spirals of magnetic declinations within core sections. Therefore, those deformed sediments indicate that RCB drilling caused pervasive disturbance in cores of soft sediment and spirals of the magnetic declination (Kimura, Silver, Blum, et al., 1997). This places severe constraints on paleomagnetic investigations of the cores from this hole.

Although the magnetic inclinations of the archive halves after AF demagnetization of 40 mT are still unclear, several inclinations appear to exhibit negative polarity (Figs. F36, F37). Some significant spikes of the inclination in which the angle shows <0° may reflect true negative polarities, although several scattered spikes reflect disturbed magnetic

F35. NRM inclination and demagnetized inclinations, p. 76.

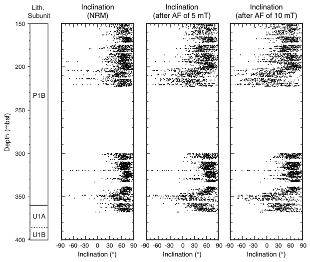

F36. Paleomagnetic results from 150 to 230 mbsf, p. 77.

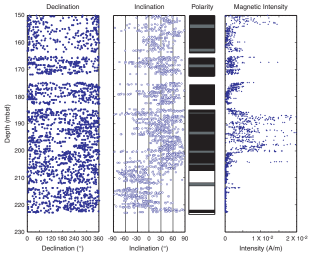

F37. Paleomagnetic results from 300 to 370 mbsf, p. 78.

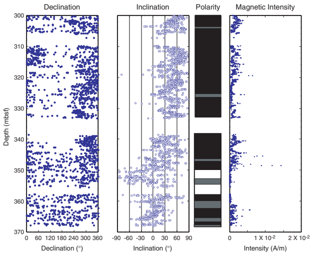

remanence caused by the drilling. However, to exactly separate the drilling-induced disturbances from the true polarities is impossible. Relatively clear negative inclinations in which angles continuously range from –70° to –10°S are observed from ~207 to ~221 mbsf (Cores 205-1254A-7R to 8R) and 350 to ~356 mbsf (Core 14R), suggesting that there may be two major negative polarity chrons. Unfortunately, a comparison of these polarities with the previous paleomagnetic investigation in Hole 1040C is not possible because of poor identification of the magnetic polarities at this time.

Scattered magnetic declinations cannot be used for the paleomagnetic study, but a reorientation of structural direction in each portion of spiraled sedimentary sections using declination data after the demagnetization of 40 mT was mostly successful (see **"Structural Geology,"** p. 20).

Magnetic Intensity

High magnetic intensities of the NRM were observed from 184 to 202 mbsf (Sections 205-1254A-5R-1 through 6R-6) and from 310 to ~350 mbsf (Sections 10R-1 through 14R-2) (Fig. **F38**). Stepwise AF demagnetization revealed that the lower interval has a different magnetic coercivity from the upper one, whereas the maximum values of both NRM intensity anomalies are nearly even.

F38. NRM intensity, magnetic intensity after 20 mT, and the ratio of the magnetic intensity after the demagnetization to the NRM intensity, p. 79.

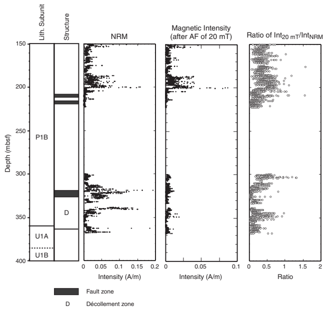

The upper intensity peak is still observed after 20-mT demagnetization. Relatively high intensity ratio of magnetic intensity after the demagnetization (20 mT) to NRM intensity ranges from ~0.5 to 0.8, which indicates that 50%–80% of the magnetization remains after the demagnetization.

The lower intensity peak of the NRM is rapidly demagnetized within weak AF demagnetization levels, and then the peak disappears completely after 20-mT AF demagnetization (Fig. **F38**). The intensity ratio indicates an interval from ~320 to 340 mbsf that exhibits very unstable magnetization, which suggests that the magnetic coercivity of the sediments is extremely weak. Sediments above and below the lower peak show ~0.2–0.7 in the intensity ratio, indicating that 20%–70% of the magnetization still remains after the demagnetization, but it is distinctly higher than that of the lower anomaly (Fig. **F38**).

The fluctuations of magnetic intensity, reflecting the magnitude of magnetization, generally indicate that changes in concentration, grain size, and chemical components of magnetic minerals relate to variability of lithology. Two high-intensity peaks of NRM in the lower anomaly (~320 and 340 mbsf) correspond to sand layers noted in sedimentological observation; however, significant lithologic changes or boundaries of the sedimentary unit were not observed around the other places. As an additional fact, the lower anomaly is overlapping with a fault zone at ~320–330 mbsf and the décollement zone (Fig. **F38**). More rock magnetic data is required to constrain these interpretations, but this suggests that chemical alteration or reducing conditions may have affected the magnetic minerals within the sediment at the fault and the décollement zones.

Magnetic Susceptibility

Magnetic susceptibility of all whole-round cores was measured by a loop susceptibility sensor on the MST unit, and the measurement of all archive-half cores was conducted using a point sensor of the AMST system (Fig. **F39**) (see **"Paleomagnetism,"** p. 21, in the "Explanatory Notes" chapter). Although the magnetic susceptibility measured by the AMST typically shows smaller values than the MST because of the different volume of the archive cores from the whole-round cores, they show almost the same trend in the magnetic susceptibility.

At Site 1254, clear highs in the magnetic susceptibility observed in the intervals from 184 to 202 mbsf (Sections 205-1254A-5R-1 through 6R-6) and from 310 to ~350 mbsf (Sections 10R-1 through 14R-2) correspond to the magnetic intensity peaks. This suggests that the magnetic intensity observed at this hole depends strongly on the magnetic grain mineralogy and concentration. Changes in magnetic susceptibility at Site 1040 also show a slight high from 160 to ~190 mbsf and high susceptibility with high variability below ~275 mbsf. Top depths of both peaks at Site 1040 are ~30 m shallower than those at Site 1254. Additionally, pronounced high variability of the magnetic susceptibilities observed below 275 mbsf at the previous site was not detected in the sedimentary cores at Site 1254. These results indicate that the concentration and distribution of the susceptible magnetic particles around the décollement zone at Site 1254 are different from Site 1040.

F39. Magnetic intensity and susceptibilities in Hole 1254A vs. magnetic susceptibility at Site 1040, p. 80.

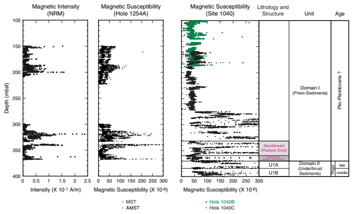

Demagnetization Analyses of Discrete Samples

For analysis of the paleomagnetic investigations, all discrete samples were demagnetized up to 80 mT in increments of 5 mT. Some samples show discontinuous demagnetization curves for both inclination and declination on the Zijderveld diagram (Fig. **F40A**), which may indicate drilling disturbance of sediments. Samples obtained from sedimentary sections corresponding to relatively low magnetic intensity zones (Fig. **F38**) often show rapid decrease of their magnetization in the early steps of AF demagnetization (Fig. **F40B**). Anomalous demagnetization curves were observed in most samples taken from the sediment exhibiting high magnetic intensity peaks (Fig. **F40C, F40D**). Their declination and inclination curves do not converge to the origin of the Zijderveld diagram, and magnetic intensity increases progressively with an increase in the AF demagnetization levels. This odd behavior is similar to demagnetization curves of greigite on stepwise AF demagnetization. Sediments in lithostratigraphic Subunit U1A show a clear and smooth demagnetization trend during the AF demagnetization (Fig. **F40E**). This suggests that the magnetization of sediments in Subunit U1A is significantly more stable than that of prism sediments.

F40. Zijderveld diagrams and demagnetization plots, Hole 1254A, p. 81.

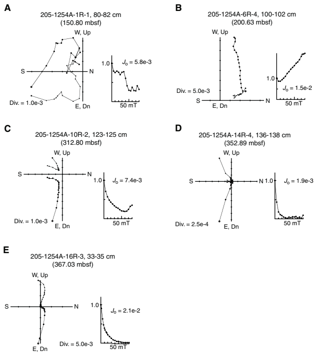

INORGANIC GEOCHEMISTRY

The main objectives for measuring key geochemical parameters of the pore waters at Site 1254 are (1) to determine the chemistry of pore fluid profiles from décollement whole rounds to compare with profiles measured at Site 1040 and to evaluate possible lateral heterogeneity; (2) to determine the composition of fluids and gases along the décollement and evaluate any possible changes through time for hydrologic modeling; (3) to use selected elements, element ratios, and isotopic compositions in the fluids from the décollement and upper fault zone to constrain dehydration reactions at the updip limit of the seismogenic zone; and (4) to determine key depth intervals in which to place the long-term geochemical observatories. These data are important because the escape of fluids to the surface from depth contributes hydrocarbons for gas hydrate formation, affects seawater chemistry for selected elements, supports a deep biosphere, and is intimately linked to deformation, faulting, and the evolution of the décollement. Furthermore, loss of fluid-soluble elements from the shallow slab not only records reactions and processes within the seismogenic zone but also plays a major role in the supply of residual volatiles deeper in the subduction zone and changes the composition of the slab delivered to the depths of magmatism beneath volcanic arcs.

A total of twenty 35- to 45-cm whole rounds were sampled at Site 1254 for pore fluid geochemistry. One to two whole rounds were taken per core from 153.7 to 217.9 mbsf and from 305.7 to 366.4 mbsf; pore water recovery ranged from 3 to 20 mL above 218 mbsf and from 2.5 to 21.0 mL below 305 mbsf. Pore waters were analyzed for Ca, Mg, K, Na, B, Ba, Fe, Mn, Sr, Si, NH_4, and SO_4 concentrations, as well as for salinity by methods described in **"Inorganic Geochemistry,"** p. 24, in the "Explanatory Notes" chapter. Pore water geochemistry data are available in Tables **T11** and **T12.** Because of low pore water recovery at Site 1254, samples were not analyzed for alkalinity and pH.

Real-Time Geochemical Analyses

Lithium, Ca, K, and Na were analyzed aboard ship in real time on the ICP-AES between 305 and 366 mbsf to facilitate identification of the zone of maximum fluid flow within the décollement. Lithium and Ca concentrations at Site 1040 (Leg 170) increased abruptly at the top of the décollement between 330 and 354 mbsf, whereas K concentrations decreased. These constituents showed reverse gradients within the transition from the décollement to the underthrust sediments as observed during Leg 170. The objective of real-time chemical monitoring for these constituents was to quickly identify the depth at which these concentration gradients occur to ensure that the underthrust sediments were not penetrated too deeply during coring so that the long-term observatories will sample décollement fluid and not a mixture of décollement and underthrust fluids. The real-time chemical analyses were very successful.

Pore Water Results

Salinity and Chloride

Salinity is below seawater value in all samples analyzed at Site 1254 (Fig. **F41**) and remains fairly constant above 197 mbsf; however, there is a sharp decrease from 29 at 210 mbsf to 25 (29% lower than seawater salinity) at 218 mbsf. The decrease in salinity is accompanied by a sharp decrease in Cl, K, and Na concentrations (Fig. **F41**) and by more gradual increases in Ca and Li concentrations (Figs. **F42A, F43B**). There is also a sharp decrease in salinity from 31 at 330 mbsf to 25 at 345 mbsf, which is accompanied by an abrupt increase in Li concentrations and a marked decrease in K concentrations similar to those observed at 218 mbsf. A sharp increase in salinity from 27 to 32 (only 9% lower than seawater salinity) occurs between 354.5 and 366.4 mbsf and reflects a transition from sediments of Subunit P1B (wedge sediments) (refer to **"Lithostratigraphy,"** p. 13) to Subunit U1A (underthrust sediments). The salinity in the uppermost underthrust sediments is similar to the uppermost salinity profile at the reference Site 1039 (Leg 170).

T11. Pore water major constituents, Site 1254, p. 107.

T12. Pore water minor constituents, Site 1254, p. 108.

F41. Salinity, Cl, Na, and K profiles, p. 82.

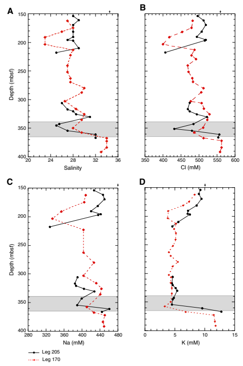

F42. Ca, Mg, Mg/Ca, and Sr profiles, p. 83.

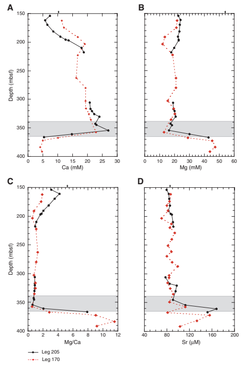

F43. Ba, Li, Si, and B profiles, p. 84.

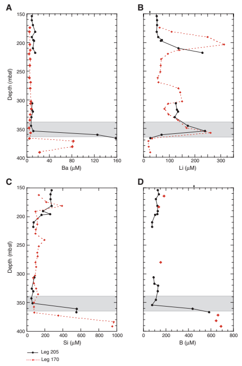

The Cl concentration depth profile (Fig. F41B) divides the sediments cored at Site 1254 into two distinct sections. One is a lower than seawater Cl concentration zone (7%–27% lower) in the deformed wedge sediments with superimposed concentration minima in the décollement and at 218 mbsf and less distinct minima from gas hydrate dissociation. The abrupt decrease in Cl concentration between 197.2 and 218.9 mbsf from 516 to 406 mM is accompanied by sharp increases in Ca and Li concentrations and decreases in Mg and K concentrations. It lies ~20 m below the corresponding Cl concentration minimum observed at Site 1040. Within the décollement, the Cl concentration is ~23% more dilute than seawater value and is also accompanied by abrupt increases in Ca and Li concentrations; however, at the 218 mbsf minimum it is 27% more dilute. The higher dilution at 218 mbsf may be an artifact of gas hydrate dissociation, which also dilutes the other components analyzed by the same proportion. Furthermore, if the Cl minima were due to gas hydrate dissociation alone, then the Na/Cl ratio would not be affected; however, the Cl minima at 218 mbsf and within the décollement are accompanied by Na/Cl minima (Table T11). The second distinct section comprises the underthrust sediments (Subunit U1A), which are typified by near-seawater Cl concentrations (~1% lower than seawater concentration).

Sodium and Potassium

Sodium concentrations are below seawater concentration (between 7% and 32% lower) in Subunit P1B and approach it (4% lower) in the transition between the décollement and underthrust sediments of Subunit U1A (Fig. F41C). There is a sharp decrease in Na concentrations from 435.91 to 328.54 mM between 197.2 and 217.9 mbsf, which is within the same depth interval that both Li and Ca increase and K and Mg concentrations decrease. Sodium concentrations show a similar decrease between 330.1 and 354.5 mbsf from 427.39 to 389.15 mM, respectively. Both of these depth intervals where Na concentrations drop abruptly are accompanied by a decrease in Cl concentrations and salinity. However, in situ production of such a low-salinity fluid from clay minerals or opal-A dehydration at the very low geothermal gradient at this site is implausible. Simple dilution by gas hydrate dissociation would tend to dilute the Ca concentrations, but rather an increase in Ca concentration is observed (Fig. F42A). There are no known diagenetic reactions that involve sodium uptake at the very low temperatures encountered at this site, except for uptake by clay minerals into the interlayer exchange sites or by zeolite formation. The clay uptake happens almost instantaneously upon exposure to seawater, and no zeolite-rich sediments were observed at this site.

Potassium concentrations are similar to seawater concentration at the top of the cored interval at Site 1254 and steadily decrease with depth from 9.28 mM at 154 mbsf to 4.54 mM (43% of seawater concentration) at 218 mbsf. This decrease in K concentrations was also observed at Site 1040 but occurred at ~200 mbsf at ~20 m above the K minimum at this site. There is another, albeit smaller, decrease in K concentrations between 330 and 350 mbsf from 5.40 to 4.51 mM, respectively. This is the same interval where increases in Ca and Li concentrations and decreases in Mg concentrations are observed. Similar decreases in K concentrations were observed at Site 1040; however, the minimum is shifted ~6 m above that at Site 1040. Potassium concentrations increase sharply from 354.5 to 366.4 mbsf from a value of 4.51 to

12.74 mM (22% higher than seawater concentration), which reflects the transition from the décollement sediments to the underthrust sediments (Subunit U1A). The higher K concentrations at the top of the cored section may be, in part, due to the higher NH_4 concentrations at the same depths (Fig. **F44B**). The NH_4 produced may displace K from the clay ion-exchange sites, producing NH_4 clays.

F44. SO_4, NH_4, Fe, and Mn profiles, p. 85.

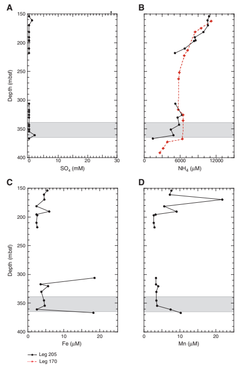

Calcium, Magnesium, and Strontium

Calcium, Mg, Mg/Ca, and Sr concentration depth profiles (Fig. **F42**) divide the sediment column at Site 1254 into three distinct sections: two are in the deformed wedge Subunit P1B, and the third is below the transition between sediments of the décollement to sediments of the underthrust section (Subunit U1A). Calcium concentrations increase from 5.69 to 18.78 mM (78% higher than seawater concentration) between 161.4 and 218 mbsf, whereas Mg concentrations decrease from 24.02 to 17.68 mM within the same interval. These changes are reflected by the decrease from a value of ~4 (seawater value is 5.4) to a value of ~1 in the Mg/Ca depth profile for Site 1254. This increase in Ca concentrations and decrease in Mg concentrations was observed at Site 1040; however, the peak at Site 1254 occurs ~20 m below the peak at Site 1040. The increase in Ca concentrations observed at ~218 mbsf at Site 1254 coincides with a reverse fault identified in the same depth interval (see **"Structural Geology,"** p. 20); however, this geochemical boundary between 161.4 and 218 mbsf appears to be lithologically indistinct (see **"Lithostratigraphy,"** p. 13). At 343 mbsf, Ca concentrations increase sharply from 22.64 to 27 mM (more than twice seawater concentration) at 354.5 mbsf. The increase in Ca concentrations is accompanied by a decrease in Mg concentrations from 20.64 to 16.22 mM within the same interval. This region in the sediment column was interpreted as the top of the décollement at Site 1040, and at Site 1254 it may coincide with a brecciated sandy layer that is moderately indurated (Fig. **F4**). The Mg/Ca ratio remains fairly constant from 306 to 354.5 mbsf and ranges between 0.92 and 0.76. At such low values of Mg/Ca, calcite diagenesis, but not dolomite diagenesis, occurs in the presence of sufficient alkalinity as seen at Site 1040. Also, Ca concentrations are relatively high and Mg concentrations are relatively low within this section. Calcium concentrations decrease sharply at 355 mbsf to 5.39 mM (~50% seawater concentration), whereas Mg concentrations increase to 42.66 mM, representing a transition from Subunit P1B to the underthrust sediments.

Strontium concentrations, unlike Ca concentrations, remain fairly constant above 218 mbsf and range between 79.50 µM at 153.7 mbsf and 91.4 µM at 218 mbsf. Below 306 mbsf, Sr concentrations range between 77.11 µM and 168.18 µM. The highest Sr concentration observed at Site 1254 is at 361 mbsf, which is ~10 m above the Sr peak at Site 1040 and may reflect the transition between the décollement sediments and the underthrust sediments.

Sulfate, Ammonium, and Barium

The SO_4 depletion zone (i.e., $SO_4 = 0$) extends to the depths cored at Site 1254 (Fig. **F44A**) as well as at Site 1040; therefore, any SO_4 analyzed in a sample would indicate drill water contamination. Fortunately, SO_4 concentrations were below the detection limit of the ion chromatograph for all but two samples analyzed at Site 1254. The two slightly contaminated samples occur at 161.4 and 360.9 mbsf and represent 3.7% and 6.6% drill water (seawater) contamination, respectively. These two data points have not yet been corrected for drilling-induced contamination; this does not affect the interpretation of the data obtained at Site 1254. The sediments of Subunit P1B are anaerobic and remain within the zero-sulfate zone; therefore, CH_4 concentrations are high and provide an environment conducive to gas hydrate formation. The SO_4 depletion zone extends below the décollement into the underthrust sediments of Subunit U1A, despite the fact that at Site 1039 the minimum SO_4 concentration encountered at ~24 mbsf is 13.2 mM. This suggests that upon underthrusting, the supply of SO_4 from seawater by diffusion ceased and the underthrust sulfate-reducing bacteria utilized the remaining SO_4 at the top of the section, thereby depleting it to zero concentration, as also observed at Site 1040.

The NH_4 concentration depth profile at Site 1254 is similar to the NH_4 profile observed at Site 1040 (Fig. **F44B**). Intense NH_4 production occurs at zero-sulfate concentrations; therefore, NH_4 concentrations are very high in both Subunit P1B and U1A. Ammonium concentrations generally decrease with depth from 10,796 µM at 153 mbsf to 1,452 µM at 366 mbsf. The very high concentrations in the deformed wedge sediments also suggest that the sediment accumulation rates are similarly high at both Sites 1254 and 1040 and that the pore water system is practically closed. Therefore, the NH_4 produced after exchanging with clay minerals remains buried in the section.

Barium concentrations at Sites 1254 and 1040 remain fairly constant between 154 mbsf and 354.5 mbsf (Fig. **F43A**). Barium concentrations between these depths at Site 1254 range between 8.55 and 14.82 µM. Barium concentrations increase abruptly from 11.17 µM at 354.5 mbsf to 158 µM at 366.4 mbsf and reflect a change in lithology from décollement sediments to underthrust sediments.

Iron and Manganese

Iron and Mn concentration depth profiles are plotted in Figure **F44.** Iron concentrations above 218 mbsf show little variation with depth except for a small increase in concentration from 2.36 µM at 181.3 mbsf to 5.92 µM at 190.6 mbsf. Below this peak, Fe concentrations range between 2.37 and 2.62 µM. Below 306 mbsf, the Fe profile is more variable, containing two distinct peaks at 306 and 366.4 mbsf of 18.51 and 18.28 µM concentrations, respectively. Manganese concentrations above 218 mbsf are variable and range between 2.68 and 21.73 µM. From 306 to 354.5 mbsf, Mn concentrations remain fairly constant and range between 3.29 and 3.62 µM. Below 354.5 mbsf, there is a sharp increase in Mn concentrations to 10.23 µM at 366.4 mbsf, reflecting the transition from décollement sediments to the underthrust sediments. Because SO_4 concentrations are zero within the depths cored at Site 1254, both $Fe(OH)_3$ and MnO_2 have been reduced by bacteria. However, above 354.5 mbsf, Fe and Mn concentrations do not show clear trends and may reflect a lithologic variations or a complex combination of redox processes and reprecipitation of mineral phases.

Lithium, Silica, and Boron

The Li concentration profiles at Site 1254 and Site 1040 are plotted in Figure **F43B.** Lithium concentrations are approximately twice seawater concentration between 153.7 and 190.6 mbsf and range from 50.78 to 57.36 µM. Lithium concentrations increase abruptly from 57.36 µM at 191 mbsf to 229.14 µM (8.5 times seawater concentration) at 218 mbsf. The increase in Li concentrations is accompanied by an increase in Ca concentrations and by decreases in Mg and K concentrations within the same depth interval. This increase in Li was also observed at Site 1040; however, the peak at Site 1254 is ~20 m below the Li spike at Site 1040. There is a small peak in Li concentrations between 306 and 320 mbsf from 125.1 to 133.82 µM, respectively, which may coincide with a brecciated sandy layer within the sedimentary sequence (Fig. F4). There is another abrupt increase in Li concentrations between 345 and 354.5 mbsf from 171.47 to 239.18 µM, respectively. This sharp increase in Li concentrations is coincident with a maximum in Ca concentrations and a minimum in Mg and K concentrations, as well as a sandy more brecciated sedimentary interval (Fig. F4). From this depth to the bottom of the cored section (366.4 mbsf), Li concentrations rapidly decrease to 25.96 µM, which is ~4% lower than seawater concentration. This decrease in Li clearly reflects the transition from sediments of Subunit P1B to the underthrust sediments.

Silica concentrations generally decrease with depth from 274.3 µM at the top of the cored interval to 71.4 µM at 218 mbsf. They remain fairly constant between 306 and 354.5 mbsf and range from 51.4 to 81.4 µM (Fig. F43C), suggesting more mature silicate diagenesis with all the opal-A transformed to the less soluble Si phases. From 351.5 to 366.4 mbsf, Si concentrations increase sharply from 61.40 µM to concentrations of 549.50 µM, which is due to the dissolution of diatoms and radiolarians that are abundant in the underthrust sediments but rare in the décollement sediments.

Boron concentrations at Site 1254 are similar to those observed at Site 1040 (Fig. F43D) and remain fairly constant between 154 and 354.5 mbsf, with concentrations ranging between 76.68 and 137.76 µM. Between 354.5 and 366.4 mbsf, B concentrations increase sharply from 76.68 to 582.67 µM, respectively. The increase in B concentrations within this interval clearly reflects the transition from deformed wedge sediments to sediments of the underthrust section.

Discussion

The geochemical excursions in salinity, K, Ca, Mg, Mg/Ca, Li, and CH_4 between 210 and 218 mbsf (Subunit P1B) occur within a highly fractured interval interpreted as a fault zone, whereas the excursions at ~351 mbsf may coincide with a brecciated sandy interval that is moderately indurated (see **"Structural Geology,"** p. 20, and **"Lithostratigraphy,"** p. 13). Small peaks in Ca, Li, and CH_4 concentrations occur at 330 mbsf and seem to be associated with another sandy brecciated interval that is less indurated than the interval below (Fig. F4). These data suggest that the deep-sourced fluid has migrated along conduits and permeated the lower half of the deformed wedge. Assuming that the geothermal gradient is ~20–30 K/km (see the **"Leg 205 Summary"** chapter), then the source region must occur at >4 km depth because the minimum temperature required for thermogenic gas formation is 80°–90°C. The minima in K concentrations at 218 and 351 mbsf further suggest that the deformed sediments have been permeated by a fluid from an elevated temperature source of 80°–120°C where the illitization reaction is effective, which consumes K. Also, the K-depletion signature of this fluid provides an approximate upper limit to the temperature at the source of ~<150°C. Above this approximate temperature, fluid-rock reactions leach K from the rocks. Lithium, like K, is partitioned into solids at low to moderate temperatures. At higher temperatures, >100°C but <250°C, Li is released into the fluid phase (Chan and Kastner, 2000). The precise threshold temperatures of partitioning into the solid or fluid phases are as yet unknown. Clay (and other silicate) dissolution or alteration releases B into the fluid phase; however, clay, especially illite, formation consumes B and may be responsible for the low B concentrations within the deformed sediments. The deeply sourced fluid, however, is not enriched in dissolved silica. Gas hydrate dissociation is caused by drilling, and core recovery causes other lesser salinity dilution excursions in the pore water concentrations. These excursions, however, are not accompanied by Ca and Li maxima.

Calcium, Li, and CH_4 concentration maxima, as well as K and Mg concentration minima, occur at ~218 mbsf at Site 1254. Similar increases in Ca, Li, and CH_4 concentrations, as well as marked decreases in Mg and K concentrations were observed at Site 1040; however, the geochemical discontinuity at Site 1040 occurred between ~180 and 200 mbsf. Therefore, the geochemical boundary at Site 1254 is ~20 m below the same boundary observed during Leg 170. At Site 1040, a fault zone was interpreted to occur at the geochemical discontinuity at ~180 mbsf because of the presence of deformation structures (Kimura, Silver, Blum, et al., 1997). A similar concentration of deformation structures was observed between 180 and 218 mbsf at Site 1254 (see **"Structural Geology,"** p. 20). The shift in the geochemical anomalies at Site 1254 to 20 m below those observed at Site 1040 suggests that the movement on the fault is reverse.

The geochemical boundary at ~218 mbsf separates pore fluids typical of clay-rich sediments above from those permeated by a fluid from an elevated temperature source and seems to be lithologically indistinct (see **"Lithostratigraphy,"** p. 13). This suggests that the main sediment source has maintained uniform chemical composition throughout the time interval represented by Subunit P1B (see **"Lithostratigraphy,"** p. 13) and that the changes in pore water chemistry result from fluid infiltration into the lower half of the deformed sediment section. The chemical changes observed in the boundary conduit at ~218 mbsf are similar to those observed near the bottom of the décollement zone that are probably associated with the sandy flow conduit. Except for the biogeochemical components, the pore fluid concentration depth profiles of the underthrust section are similar to those at Site 1039. The concentrations themselves can be either lower or higher than those at Site 1039, reflecting the changes in solubilities and dissolution rates of the major sediment components under the new pressure regime. The higher NH_4 concentrations than those at Site 1039 and the zero-sulfate concentrations at the interface between décollement and the underthrust sediments reflect the termination of diffusional communication with bottom seawater. Sulfate reduction, thus, reaches completion in the uppermost few meters of the underthrust hemipelagic section, resulting in somewhat elevated CH_4 concentrations within the zero-sulfate depth interval.

ORGANIC GEOCHEMISTRY

The main objectives for Site 1254 with respect to the organic geochemistry are (1) characterizing the hydrologic system along the décollement and the upper conduit observed during Leg 170 at Site 1040; (2) determining the chemistry and composition of pore fluids and gases from the décollement to compare with profiles measured during Leg 170 and to evaluate possible spatial heterogeneity and any possible changes through time for diagenetic and hydrologic modeling; (3) constraining pathways of fluid return to the surface and to evaluate the effects of this flow system on element fluxes; and (4) determining the horizon for long-term fluid flow monitoring.

Gas Results

Volatile Hydrocarbons

At the prism Site 1254, volatile hydrocarbon gases (primarily methane, ethane, and propane) were sampled by headspace and vacutainer techniques and analyzed by gas chromatography (see **"Organic Geochemistry,"** p. 26, in the "Explanatory Notes" chapter). A major focus was to exactly determine the depths of the two main flow conduits discovered at Site 1040 during Leg 170 (Kimura, Silver, Blum, et al., 1997). The décollement conduit was of special interest for the deployment of the OsmoSampler and for determining where the base of the décollement is (see **"Operations,"** p. 8, and **"Inorganic Geochemistry,"** p. 27). Therefore, samples were taken at a high frequency (i.e., generally three vacutainers and four headspace samples per core) and analyzed as soon as possible to allow for real-time monitoring. Vacutainer results are summarized in Table **T13** and shown in Figure **F45,** whereas headspace data are compiled in Table **T14** and shown in Figure **F46.**

T13. Vacutainer gas composition, p. 109.

F45. Vacutainer gas analyses, p. 86.

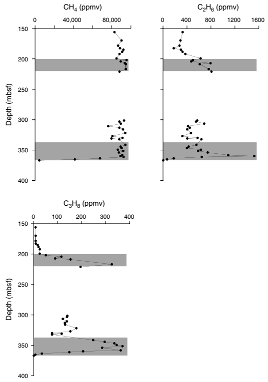

The hydrocarbon concentrations in the vacutainers are significantly higher (up to 99.9 vol%) than those obtained by headspace technique, but both show similar hydrocarbon ratios for equivalent depth intervals as well as similar concentration profiles (Figs. **F45, F46**). The difference between the two data sets is readily explained by the different sampling techniques causing a loss of hydrocarbons, especially the more mobile methane, before the headspace sediment is sealed in the glass vial (Stein et al., 1995). Hence, scattering in the headspace data points occurs more frequently. Vacutainer results were found to show much less scatter. Besides the hydrocarbon concentrations, the fractions of O_2, N_2, and CO_2 in the gas samples are reported in Table **T13** to estimate possible contamination by air during the sampling procedure. This approach is applicable to samples in which methane is the major gas component in the sediments because of production by methanotrophy (e.g., 150–356 mbsf). For the vacutainer plots (Fig. **F45**), data points highly contaminated by air were omitted (see Table **T13**). Therefore, the results of the vacutainer samples are considered more reliable at Site 1254 and are preferred for the discussion.

T14. Headspace gas composition, p. 110.

F46. Headspace gas analyses, p. 87.

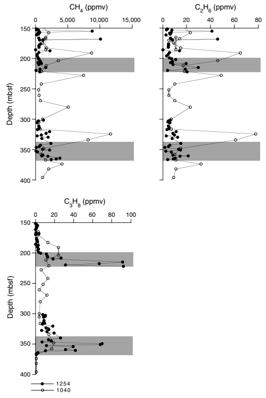

Gas voids were observed throughout the cored sediment section and were sampled with a plastic syringe. The gas in the voids consisted mainly of methane but also showed considerable amounts of higher alkanes up to the homologous pentane. Methane concentrations were very high (7×10^5 to 9×10^5 ppmv in the vacutainers) throughout the cored sediment intervals above and within the décollement and drastically dropped down to 4×10^4 ppmv directly below the décollement at 363 mbsf (Fig. **F45**). Ethane concentrations were significantly lower (~200–800 ppmv) and showed a peak concentration of 1500 ppmv at 360 mbsf. Based on the data from Site 1040 (Kimura, Silver, Blum, et al., 1997), propane was chosen as an indicator for flow conduits because it was absent above the prism fault as well as below the décollement. Its thermogenic origin (80°–120°C) (Claypool and Kvenvolden, 1983) implies that propane is produced in far deeper sediment layers and transported upward through the flow conduit system including the décollement. Propane concentrations show at least two significant peaks, at 216 mbsf and in the décollement at 355 mbsf, with maximum concentrations of 326 and 370 ppmv, respectively. A smaller peak was detected in the décollement zone at 322 mbsf. At these depths also, higher hydrocarbons (i.e., butane, isobutane, and isopentane) were detected in considerable amounts. The three propane concentration peaks correlate with structural and lithologic observations (see **"Structural Geology,"** p. 20). The uppermost peak at ~220 mbsf corresponds to a highly fractured interval that is interpreted as a fault zone, whereas the two lower peaks are connected to the décollement fault zone. The lithology shows a brecciated sandy interval at 345–356 mbsf, near the 370-ppmv propane peak at the base of the décollement, whereas the smaller peak at ~325 mbsf is near a fractured foliated interval just above the décollement (at 320–330 mbsf). These lithologies may act as flow conduits. Compared to the Site 1040 data, propane data at Site 1254 document that the uppermost flow conduit is observed ~20 m deeper. The fluid conduit in the décollement is observed at almost the same depth at Site 1040; the same is true for the lithologic boundary with the underthrust section (see **"Structural Geology,"** p. 20). Overall, the results verify and better define the vertical structure of the flow conduits as determined during Leg 170.

CH_4/C_2H_6 ratios (Table **T13**) show values between 1500 and 2000 in the whole prism section cored (150–360 mbsf), with two minima of 1088 and 586 at the flow conduits, indicating migrating thermogenic hydrocarbons. Below 363 mbsf (i.e., in the underthrust sediments), the methane-to-ethane ratio rapidly increases to ~10,000, indicating methanogenesis as the major source for hydrocarbons.

Sediment Results

Inorganic Carbon, Organic Carbon, and Total Sulfur

The depth distributions of inorganic carbon (represented as calcium carbonate), organic carbon, nitrogen, and sulfur in the solid phase from the cores in Hole 1254A are reported in Table **T15.** The combined concentration-depth data from Sites 1254 and 1040 are plotted for $CaCO_3$, total organic carbon (TOC), and total sulfur in Figure **F47.**

Calcium carbonate concentrations are generally low (<10 wt%), whereas the TOC content fluctuates (typically ~1.0 wt%) and is slightly elevated (up to 1.5–2.0 wt%) at the base of the décollement zone (>330 mbsf). Total sulfur concentrations vary between 0 and 1.5 wt%, similar to the amounts measured in Subunits P1B and U1A during Leg 170 (Kimura, Silver, Blum, et al., 1997). In particular, the higher sulfur concentrations (~1.0–1.5 wt%) are observed at the thrust fault (~220 mbsf) and in the décollement zone (350–360 mbsf), although these observations must be regarded as tentative, given the poor accuracy of the sulfur data.

T15. $CaCO_3$, total carbon, TOC, TN, and total sulfur contents, p. 111.

F47. TOC, $CaCO_3$, and S profiles, p. 88.

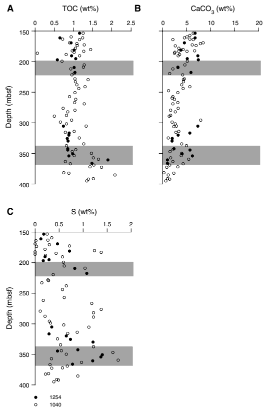

Composition of Organic Matter

To characterize the type of organic matter in the sediments, total organic carbon/total nitrogen (TOC/TN) values and hydrogen index (HI) values from Rock-Eval pyrolysis have been used. Unfortunately, the S_3 channel of the Rock-Eval did not record any data and, hence, no oxygen index (OI) or S_2/S_3 ratio could be calculated (Table T16).

T16. Rock-Eval data, p. 112.

Most of the TOC/TN values range from 4 to 8 (Table T15), which indicate a predominantly marine origin of the organic material (Bordovskiy, 1965; Emerson and Hedges, 1988). In contrast, the generally low HI values (50–120 mg HC/g TOC) (Table T16) suggest a significant input of terrigenous material (Emeis and Kvenvolden, 1986). Whereas the data from Site 1040 (Kimura, Silver, Blum, et al., 1997) also suggested this composition of organic matter, the HI values were significantly higher, suggesting marine-dominated TOC. The elevated OI values (not determined at Site 1254) indicated a significant input of terrigenous organic matter. At Site 1254, the low content of pyrolizable carbon as well as the combination of temperatures of maximum hydrocarbon generation (T_{max}) <440°C and low production indexes (PI < 0.2) reflect organic matter that is immature for oil production. In addition, the PI depth profile shows a distinct peak value of 0.31 in Section 205-1254A-14R-3, which might be interpreted as a sign for migrated hydrocarbons. Although a similar pattern was not reported for Site 1040, the coincidence with the depth of the fluid conduit in the décollement is noteworthy. Furthermore, during whole-round preparation from Cores 205-1254A-13R, 14R, and 15R for the inorganic geochemical analyses, a weak but distinct smell of aromatic compounds (i.e., of oil/gasoline) was noticeable.

MICROBIOLOGY

Twenty 5-cm-long whole rounds were taken adjacent to interstitial water whole rounds, in those sections of the core judged most intact (Table T17). Two samples (5 cm^3 each), from pared biscuits where possible, were frozen at –80°C immediately after collection for postcruise ATP quantification and DNA assessment. A total of 0.5-cm^3 samples from the same locations were fixed in 2% formalin solution for postcruise cell counting. Twice during coring, 40-mL samples of drilling fluid were collected as the fluid escaped the core liner, and these samples were also frozen promptly at –80°C; evaluation of the drilling fluid will constrain estimates of core contamination in terms of real cell numbers.

T17. Microsphere counting results, Hole 1254A, p. 113.

The chemical tracer was not deployed during coring in Hole 1254A because the trace element chemistry of the perfluorocarbon tracer could not be certified and was judged possibly deleterious to postcruise pore fluid geochemical assays. This possibility was subsequently clarified and cleared the use of the chemical tracer. Fluorescent microspheres were deployed in every core and counted using epifluorescence microscopy, as described in **"Microbiology,"** p. 28, in the "Explanatory Notes" chapter. Microsphere counting results are tabulated in Table T17. The results reflect very low to no particulate contamination in the interior of the microbiology whole rounds and document the delivery of microspheres to all except Cores 205-1254A-9R and 16R, albeit in small numbers.

DOWNHOLE MEASUREMENTS

Downhole measurements at Site 1254 consisted of one deployment of the DVTP and two deployments of the DVTPP to determine in situ formation temperatures and pressures. In order to remove possible causes for the disturbed measurements collected at Site 1253, we tried several configurations of measurement times in the sediment, at the bottom of the hole, and the mudline, and we also changed the instrument.

The first measurement was performed at 50 mbsf. The DVTPP records still showed severe disturbances during in situ formation measurements. Because we presumed that the latching system might have been responsible for the vertical movement of the tool, the system that connects the probe to the core barrel head was modified. In order to isolate problems which may be associated with the DVTPP design, we ran the DVTP at 150 mbsf, which showed improvement but still not a clear and undisturbed decay. The DVTPP was used again at 200 mbsf, and the improved data quality of the temperature record allowed for extrapolation of undisturbed sediment temperature.

During all runs, the shipboard active heave compensator was activated after the mudline stop.

Davis-Villinger Temperature-Pressure Probe at 50 mbsf

Temperature

In contrast to the measurements performed at Site 1253, we stopped 5 min at the mudline, 5 min at the bottom of the hole, and 15 min in the formation. The temperature record is illustrated in Figure **F48A** and **F48C.** The temperatures recorded at the mudline (1757–1803 hr UTC) and the bottom of the hole (1805–1810 hr UTC) can hardly be distinguished because of the small depth difference. Both are very close to the bottom water temperature of 1.989°C, determined earlier during this cruise. The penetration into the sediment (1813 hr UTC) is clearly marked, but lacks a decay. Instead, slightly increasing temperatures with significant scatter were recorded; undisturbed sediment temperature cannot be inferred. The strong temperature increase at 1830 hr UTC was caused by pulling the tool out of the sediment.

F48. DVTPP deployment at 50 mbsf, p. 89.

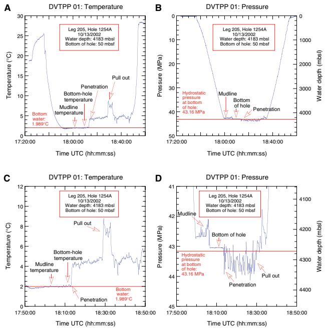

For a thermal gradient of 0.0083 K/m, as calculated from Site 1040 data, and the bottom water temperature of 1.989°C, determined during Leg 205, the expected temperature at 50 mbsf is 2.404°C. This expected temperature is considerably lower than any temperatures recorded during this penetration. It is possible that the movement of the tool created enough frictional heating to prevent a decay to in situ temperatures.

Pressure

The observed pressure increased from ~0.1 MPa at sea level to ~43.05 MPa at the bottom of the borehole (Fig. **F48B, F48D**). During the mudline stop, the high variability of the measured pressure was most likely caused by the vertical heave inducing movement of the tool that acted as a moving piston inside the drill pipe. The same features also occurred in the pressure records at Site 1253 (see **"Downhole Measurements,"** p. 53, in the "Site 1253" chapter). After the active heave compensator was activated, the record at the bottom of the hole did not show significant distortion; however, while the tool was in the formation, the record was strongly disturbed. The penetration itself is clearly marked, but no pressure decay can be observed and large variations, including excursions to pressure values below hydrostatic, suggest vertical tool movement.

A formation pressure cannot be extrapolated from the penetration record, but the expected hydrostatic pressure at bottom of the hole can be estimated. With a constant seawater salinity, temperature, and density increasing linearly with depth (1030 kg/m^3 at the top), the hydrostatic pressure at 50 mbsf is 43.16 MPa, which is close to the observed pressure of 43.05 MPa at the bottom of the hole.

Davis-Villinger Temperature Probe at 150 mbsf

Temperature

The DVTP was chosen for the second deployment at 150 mbsf. Therefore, we obtained only temperature data here, but it is of slightly better quality (Fig. **F49**). This second run was performed without a stop at the bottom of the hole. The mudline temperature was recorded for 5 min prior to penetration (0612–0617 hr UTC) and also after penetration. Prior to penetration, it was not as stable as expected and the measured temperature of 1.85°C was considerably lower than the expected bottom water temperature of 1.989°C. After we pulled the tool out of the sediments, the mudline temperature was more stable and had risen to 1.94°C, which was close to the expected temperature. This effect was probably caused by pumping, which was stopped at 0612 hr UTC on 14 October.

F49. DVTP deployment at 150 mbsf, p. 90.

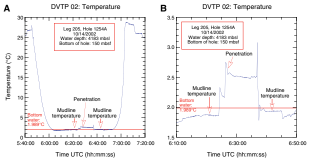

The penetration (0624–0637 hr UTC) consisted of two spikes that indicated that the probe had moved down during the equilibration period. Following the second spike, a decay was seen, but data were still too noisy to be extrapolated using CONEFIT (Davis et al., 1997) software. A visual estimate yielded a temperature of 2.48°C for the formation, which is considerably lower than temperature measurements from Leg 170 (Kimura, Silver, Blum, et al., 1997). The expected temperature at 150 mbsf, calculated from the Site 1040 thermal gradient, would yield a value of 3.234°C. Because the recorded data are reasonable and of presumed higher quality than previous data, this difference in sediment temperatures may be caused by formation cracking during penetration with colder bottom water seeping into the formation. Unfortunately, this hypothesis cannot be tested because the temperature at the bottom of the hole was not measured in this run.

Davis-Villinger Temperature-Pressure Probe at 200 mbsf

Temperature

After modification of the latching system and recording the less disturbed data with the DVTP, we used the DVTPP again for the third measurement. This time, we performed a 5-min stop at the mudline prior to penetration and the temperature at the bottom of the hole and a second mudline measurement were taken after the penetration. We hoped to see less influence of pumping at the mudline. The record is shown in Figure **F50A** and **F50C.**

F50. DVTPP deployment at 200 mbsf, p. 91.

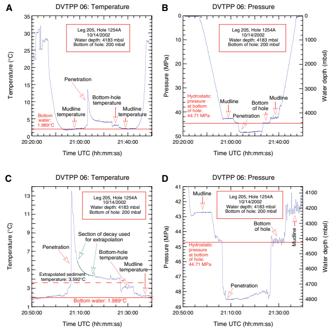

Starting with 1.9°C, the mudline temperature increases from 2053 to 2100 hr UTC by 0.2°C. After the penetration, the mudline temperature is much more stable at 2.19°C, with a scatter of ~0.02°C. Nevertheless, a slight increase with time is still observed, and the measured temperature is higher than expected.

The penetration is clearly marked at 2107 hr UTC and shows a clear decay. Processing using the software CONEFIT was successful and yielded a sediment temperature of 3.592°C. The most undisturbed part of the decay curve from 210900 to 212520 hr UTC was used for this calculation, as marked in Figure **F50C.** The expected sediment temperature using the known gradient of Leg 170 data is 3.649°C (Kimura, Silver, Blum, et al., 1997), which is consistent with the extrapolated value.

Pressure

For the first pressure measurement at the mudline the active heave compensator was already switched on, so we see a very stable pressure record of 42.7 MPa there (Fig. **F50B, F50D**). In contrast to this, the records at the bottom of the hole and the mudline after the penetration show a highly variable pressure, suggesting vertical motion because active heave compensation was switched off directly after pullout. Pressure at the bottom of the hole is almost equal to the expected hydrostatic value of 44.71 MPa.

Although reasonable pressures are recorded at the mudline and the bottom of the hole, the pressure in the formation is unreasonably high. A maximum overpressure equal to the lithostatic load of ~1 MPa is possible at this depth, but the apparent value of 3 MPa observed here is unreasonably high. One explanation for this observation would be that the pressure port was clogged with mud. A decay is also missing so that no in situ formation pressures can be inferred.

Nevertheless, an improvement in data quality is obvious by the significantly lower variability of the pressure measurement in the formation compared to the first run. This improvement was made possible by the modification of the latching system.

REFERENCES

Biscaye, P.E., 1965. Mineralogy and sedimentation of recent deep-sea clays in the Atlantic Ocean and adjacent seas and oceans. *Geol. Soc. Am. Bull.,* 76:803–832.

Bordovskiy, O.K., 1965. Accumulation and transformation of organic substances in marine sediment, 2. Sources of organic matter in marine basins. *Mar. Geol.,* 3:5–31.

Burnham, C.W., and Jahns, R.H., 1962. A method of determining the solubility of water in silicate melts. *Am. J. Sci.,* 260:721–745.

Chan, L.-H., and Kastner, M., 2000. Lithium isotopic compositions of pore fluids and sediments in the Costa Rica subduction zone: implications for fluid processes and sediment contribution to the arc volcanoes. *Earth Planet. Sci. Lett.*, 183:275–290.

Claypool, G.E., and Kvenvolden, K.A., 1983. Methane and other hydrocarbon gases in marine sediment. *Annu. Rev. Earth Planet. Sci.,* 11:299–327.

Cox, K.G., Bell, J.D., and Pankhurst, R.J., 1979. *The Interpretation of Igneous Rocks:* London (Allen and Unwin).

Davis, E.E., Villinger, H., MacDonald, R.D., Meldrum, R.D., and Grigel, J., 1997. A robust rapid-response probe for measuring bottom-hole temperatures in deep-ocean boreholes. *Mar. Geophys. Res.,* 19:267–281.

Emeis, K.-C., and Kvenvolden, K.A., 1986. Shipboard organic geochemistry on *JOIDES Resolution. ODP Tech. Note,* 7.

Emerson, S., and Hedges, J.I., 1988. Processes controlling the organic carbon content of open ocean sediments. *Paleoceanography,* 3:621–634.

Flügel, E., 1982. *Microfacies Analysis of Limestones:* Berlin (Springer-Verlag).

Gambhir, M., Dove, M.T., and Heine, V., 1999. Rigid unit modes and dynamic disorder: SiO_2 cristobalite and quartz. *Phys. Chem. Miner.,* 26:484–495.

Kimura, G., Silver, E.A., Blum, P., et al., 1997. *Proc. ODP, Init. Repts.,* 170: College Station, TX (Ocean Drilling Program).

Middlemost, E.A.K., 1975. The basalt clan. *Earth Sci. Rev.,* 11:337–364.

Mitsui, K., and Taguchi, K., 1977. Silica mineral diagenesis in Neogene Tertiary shales in the Tempoku District, Hokkaido, Japan. *J. Sediment. Petrol.,* 47:158–167.

Miyashiro, A., 1978. Nature of alkalic volcanic rock series. *Contrib. Mineral. Petrol.,* 66:91–104.

Ninkovich, D., Sparks, R.S.J., and Ledbetter, M.T., 1978. The exceptional magnitude and intensity of the Toba eruption, Sumatra: an example of the use of deep-sea tephra layers as a geological tool. *Bull. Volcanol.,* 41:286–297.

Ranero, C.R., and von Huene, R., 2000. Subduction erosion along the Middle America convergent margin. *Nature*, 404:748–752.

Sarna-Wojcicki, A.M., Shipley, S., Waitt, R.B., Dzurisin, D., and Wood, S.H., 1981. A real distribution, thickness, mass, volume, and grain size of air-fall ash from the six major eruptions of 1980. *In* Lipman, P.W., and Mullineaux, D.R. (Eds.), *The 1980 Eruptions of Mount St. Helens, Washington.* U.S. Geol. Surv. Prof. Pap., 577–600.

Shipboard Scientific Party, 1997a. Site 1039. *In* Kimura, G., Silver, E., Blum, P., et al., *Proc. ODP, Init. Repts.,* 170: College Station, TX (Ocean Drilling Program), 45–93.

————, 1997b. Site 1040. *In* Kimura, G., Silver, E., Blum, P., et al., *Proc. ODP, Init. Repts.,* 170: College Station, TX (Ocean Drilling Program), 95–152.

Stein, R., Brass, G., Graham, D., Pimmel, A., and the Shipboard Scientific Party, 1995. Hydrocarbon measurements at Arctic Gateways sites (ODP Leg 151). *In* Myhre, A.M., Thiede, J., Firth, J.V., et al., *Proc. ODP, Init. Repts.,* 151: College Station, TX (Ocean Drilling Program), 385–395.

Tobin, H., Vannuchi, P., and Meschede, M., 2001. Structure, inferred mechanics, and implications for fluid transport in the décollement zone, Costa Rica convergent margin. *Geology,* 29:907–910.

Vannucchi, P., and Tobin, H., 2000. Deformation structures and implications for fluid flow at the Costa Rica convergent margin, Ocean Drilling Program Sites 1040 and 1043, Leg 170. *J. Struct. Geol.,* 22:1087–1103.

Walker, G.P.L., 1971. Grain-size characteristics of pyroclastic deposits. *J. Geol.,* 79:696–714.

Watkins, N.D., Sparks, R.S.J., Sigurdsson, H., Huang, T.C., Federman, A., Carey, S., and Ninkovich, D., 1978. Volume and extent of the Minoan tephra layer from Santorini Volcano: new evidence from deep-sea sediment cores. *Nature,* 271:122–126.

Williams, H., and Goles, G., 1968. Volume of the Mazama ash fall and the origin of Crater Lake Caldera. In *Andesite Conference Guidebook.* Bull.—Oreg., Dep. Geol. Miner. Ind., 16-S:37–41.

Wilson, J.L., 1974. Characteristics of carbonate platform margins. *AAPG Bull.,* 58:810–824.

Figure F1. Drill sites occupied during Leg 205 are shown as yellow circles and those during Leg 170 drill sites as white circles. The segment of multichannel seismic profile BGR 99-44 (red line) across Sites 1254 and 1040 is shown in Figure F2, p. 43. Leg 170 drill sites were based on seismic profile CR-20 (yellow line). Bathymetric map is an integration of the compilation by Ranero and von Huene (2000) and Simrad data from E. Flueh (pers. comm., 2000). The plate convergence direction is N30°E (arrow).

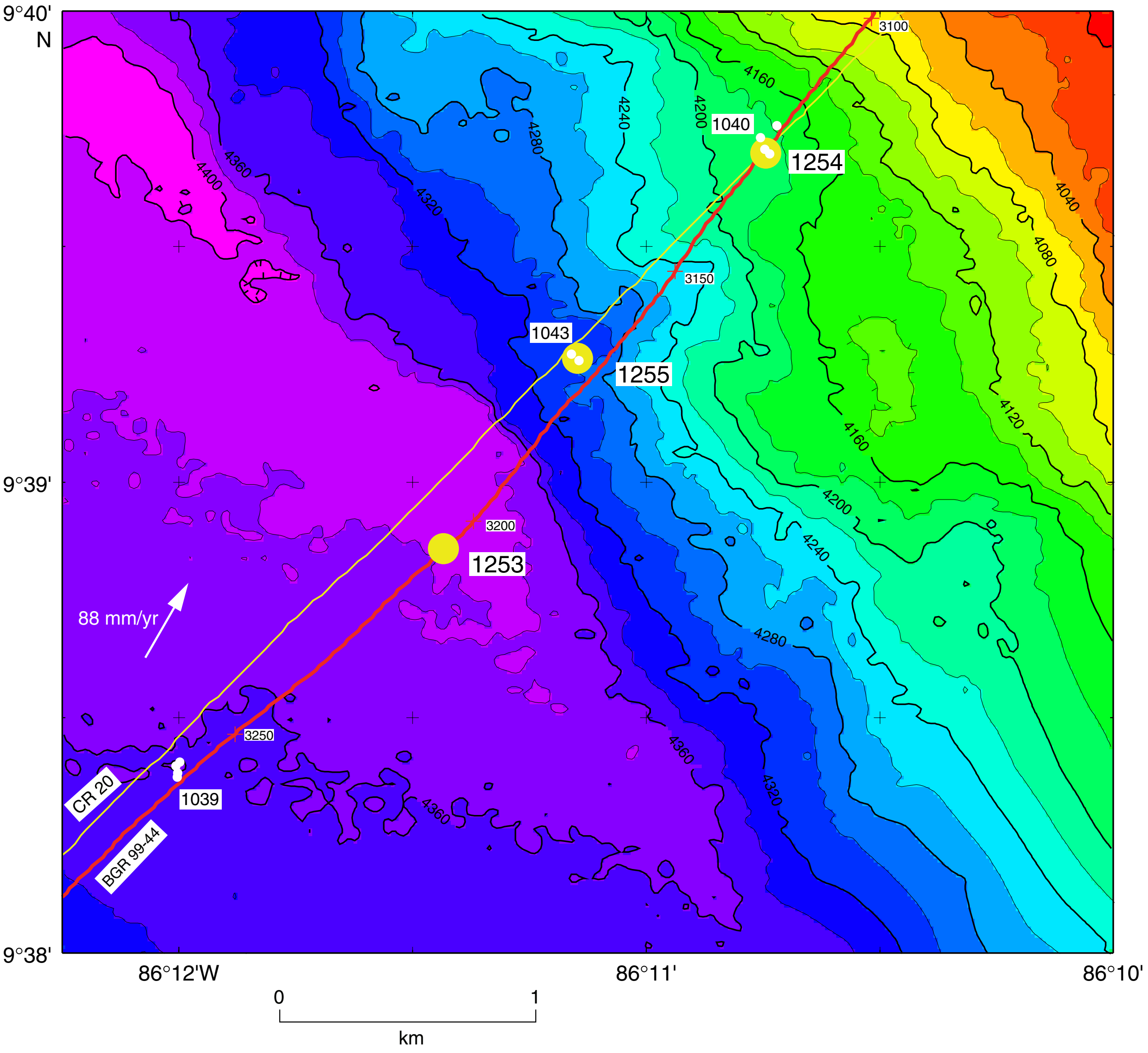

Figure F2. Location of Site 1254. Solid circles = Leg 205 sites, open circles = Leg 170 sites. Bathymetric map is an integration of the compilation by Ranero and von Huene (2000) and Simrad data from E. Flueh (pers. comm., 2000). LWD = logging while drilling.

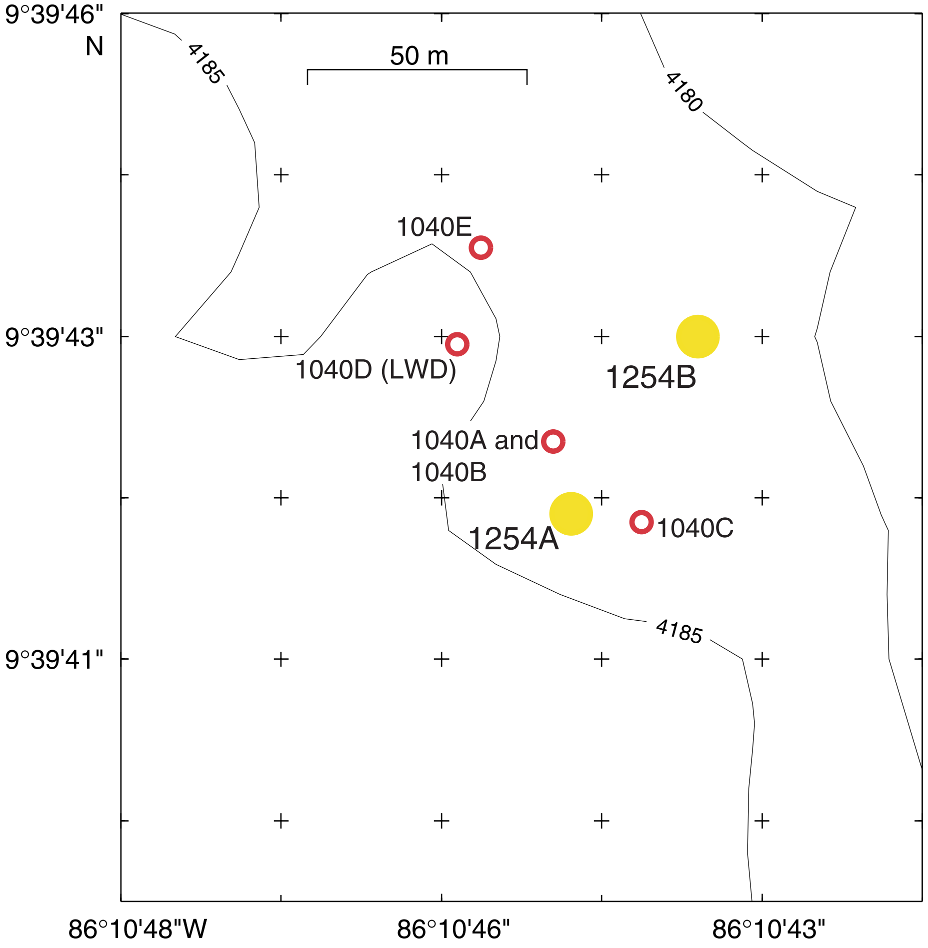

Figure F3. Portion of MCS profile BGR 99-44 across Sites 1254 and 1040. Location of seismic profile is shown in Figure F1, p. 42. Figure F3, p. 44, in the "Leg 205 Summary" chapter, shows the BGR 99-44 seismic profile across all drill sites. Vertical exaggeration = 1.7. CMP = common midpoint.

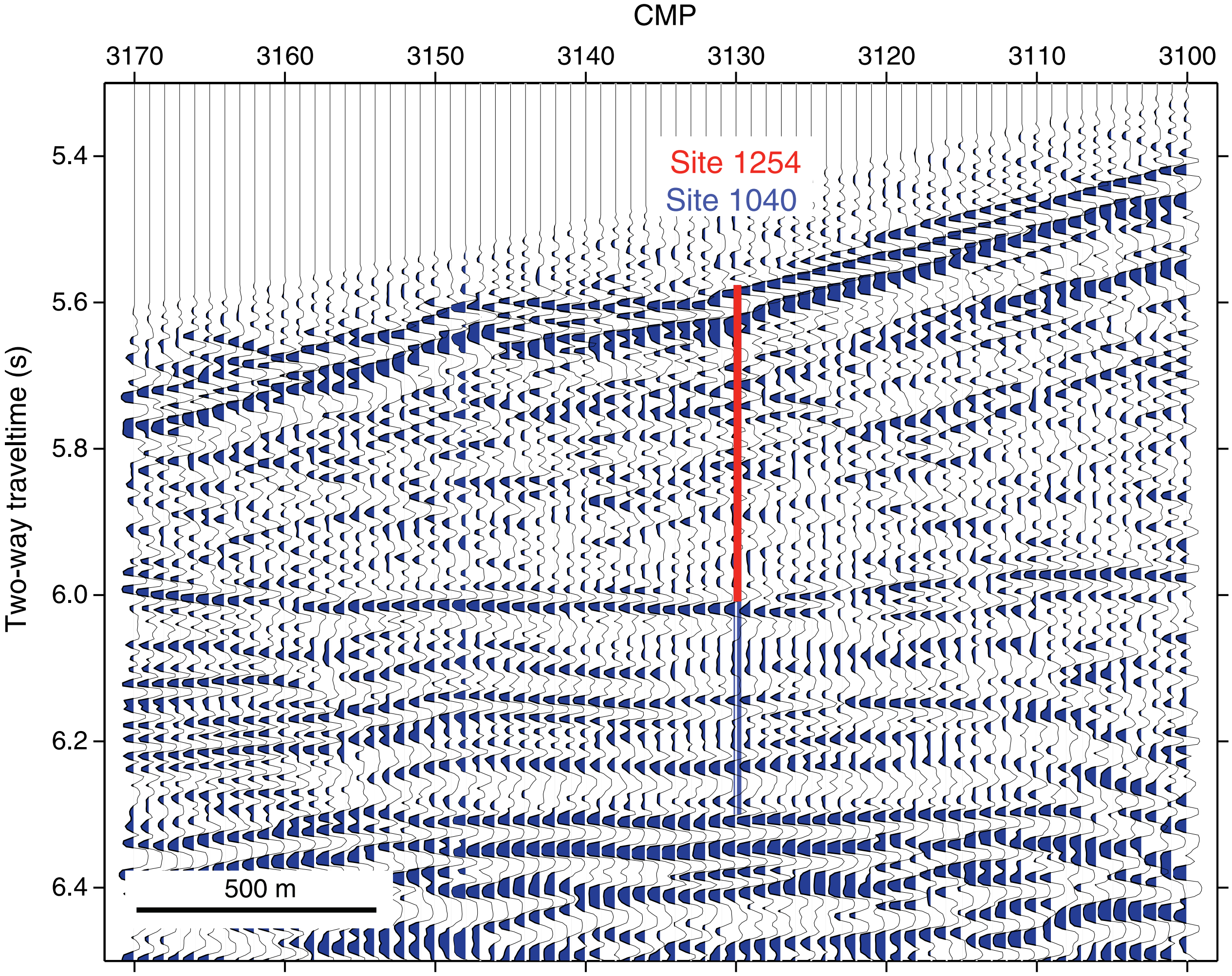

Figure F4. Summary of results from Hole 1254A. Composite view of structural and geochemical results from Hole 1254A with identification of major structural elements.

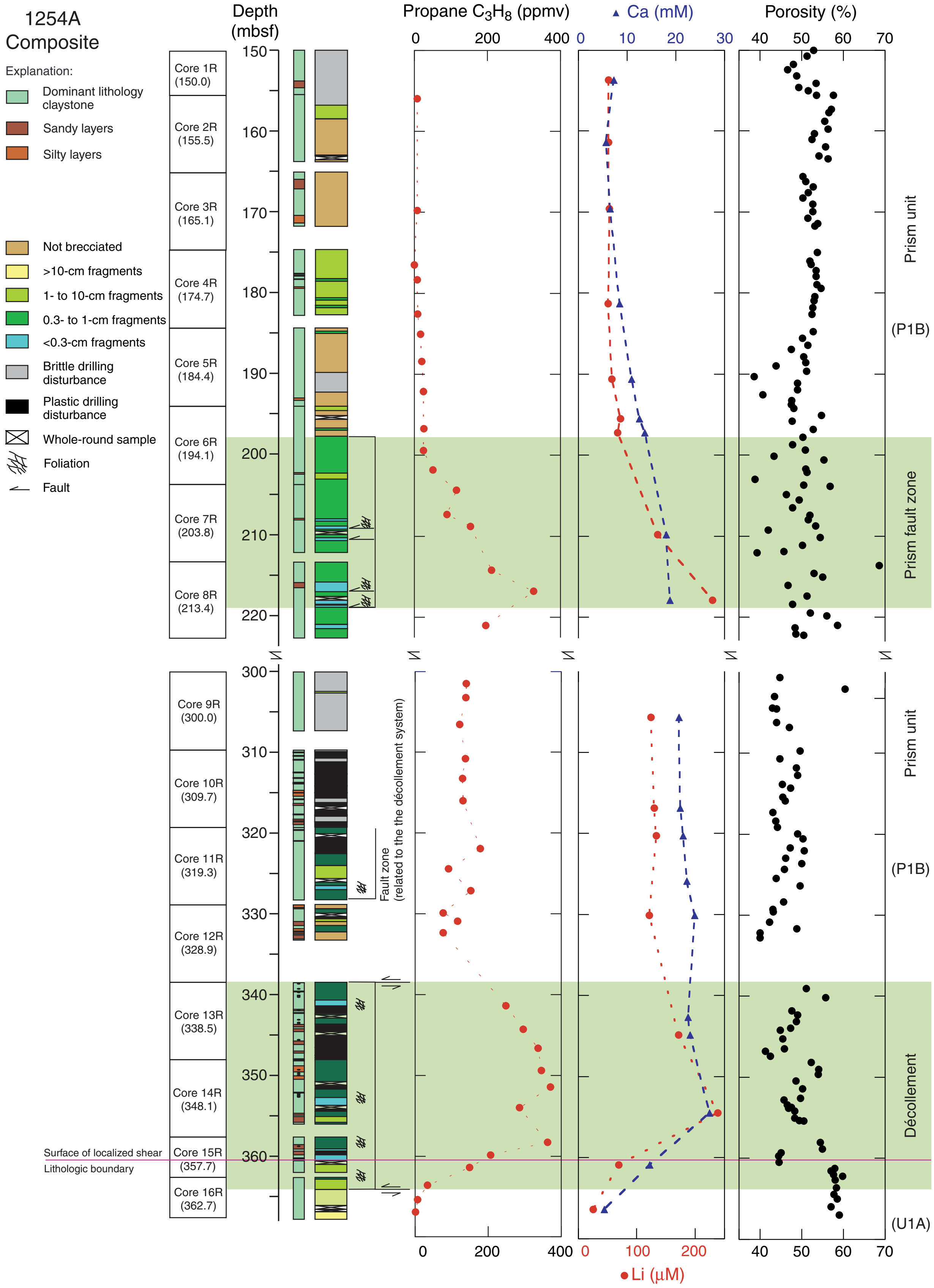

Figure F5. Close-up photograph showing the lithologic boundary between the forearc prism sediment (lithostratigraphic Subunit P1B), represented here as a darker claystone, and the underthrust sediment (lithostratigraphic Subunit U1A), which is seen here as a lighter more silt-rich claystone (interval 205-1254A-15R-2, 128–145 cm; 360.6 mbsf).

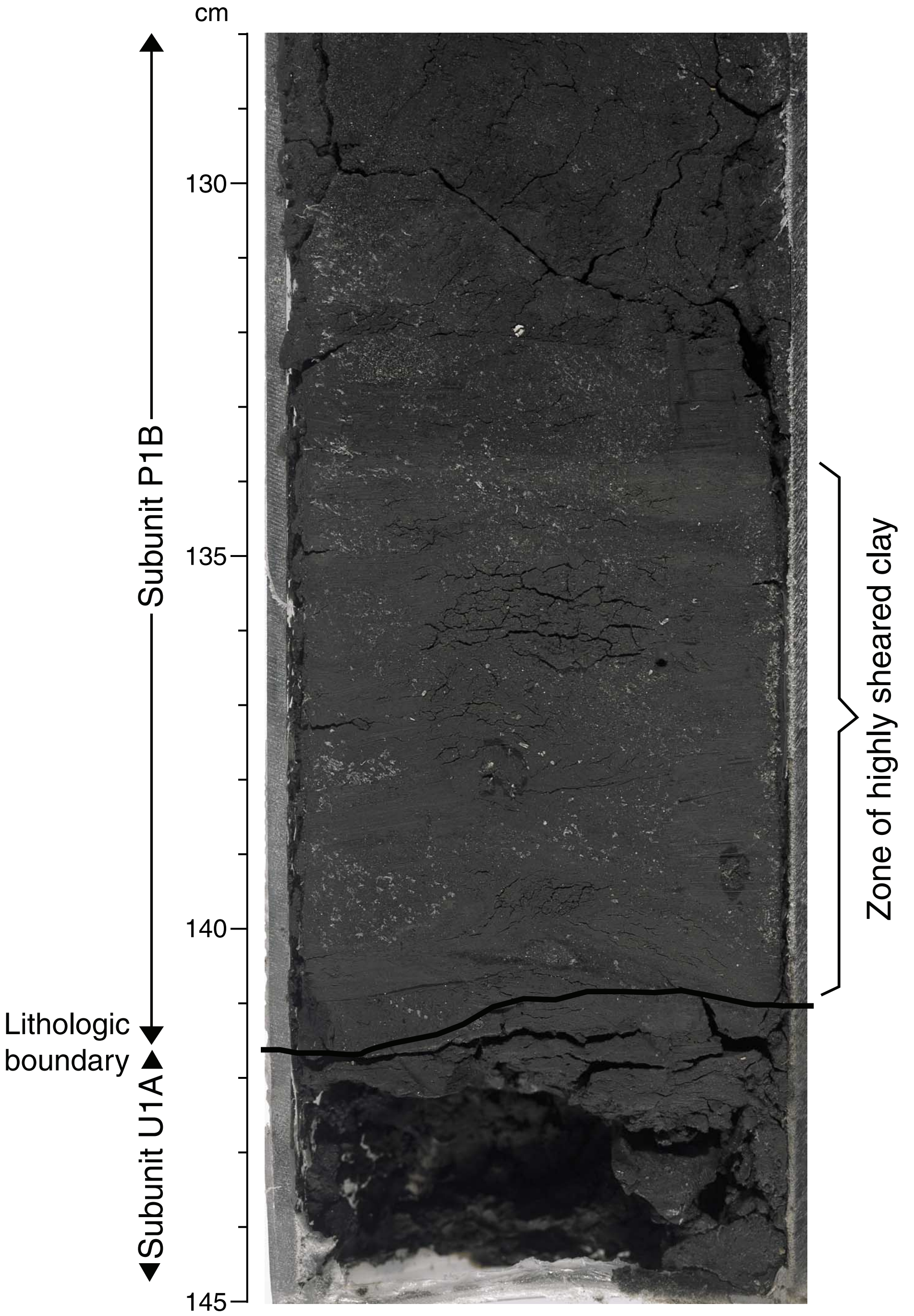

Figure F6. Close-up photograph of the deformed hemipelagic Subunit U1A within the lowermost décollement zone and below the surface of concentrated shear (interval 205-1254A-16R-1, 96–100 cm).

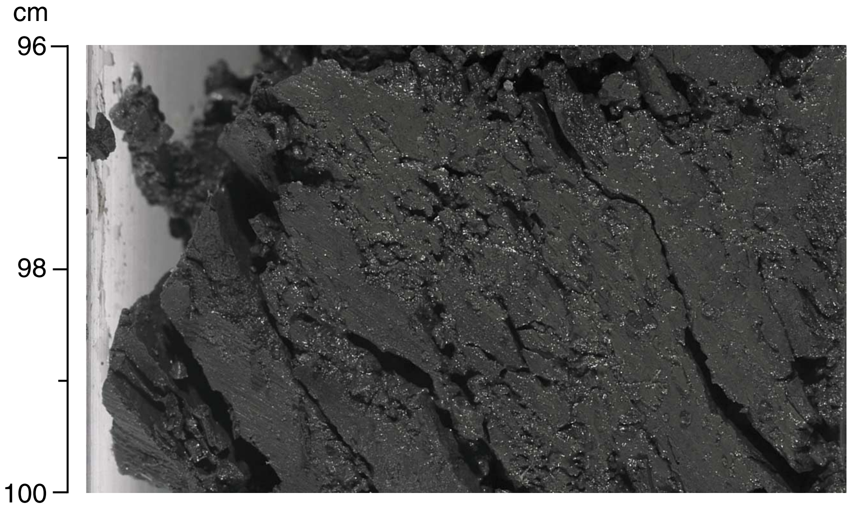

Figure F7. Photograph of a fault gouge (Riedel shear) developed by brittle shearing in a zone of discrete deformation in the hemipelagic sediments of Subunit U1A (interval 205-1254A-16R-2, 20–32 cm).

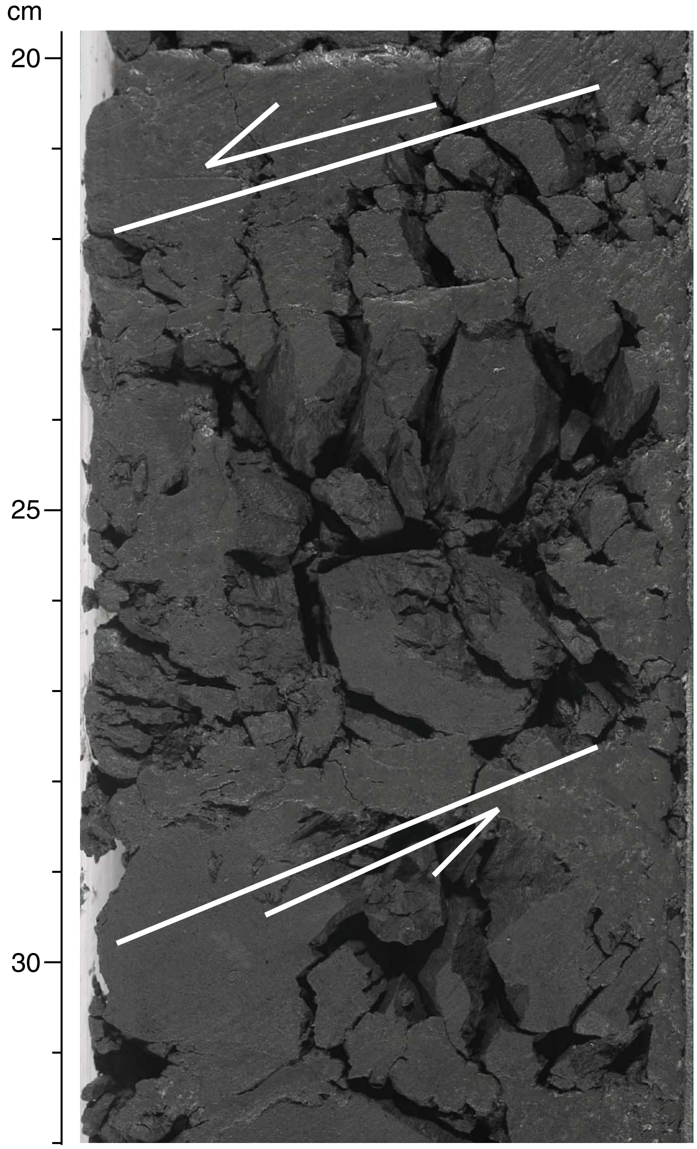

Figure F8. Composite stratigraphic log of the sedimentary section recovered at Sites 1040 and 1254, showing the degree of recovery, the principal stratigraphic units consistent with those defined by the Leg 170 scientific party, and the variation in lightness and chromaticity measured by the archive multisensor track.

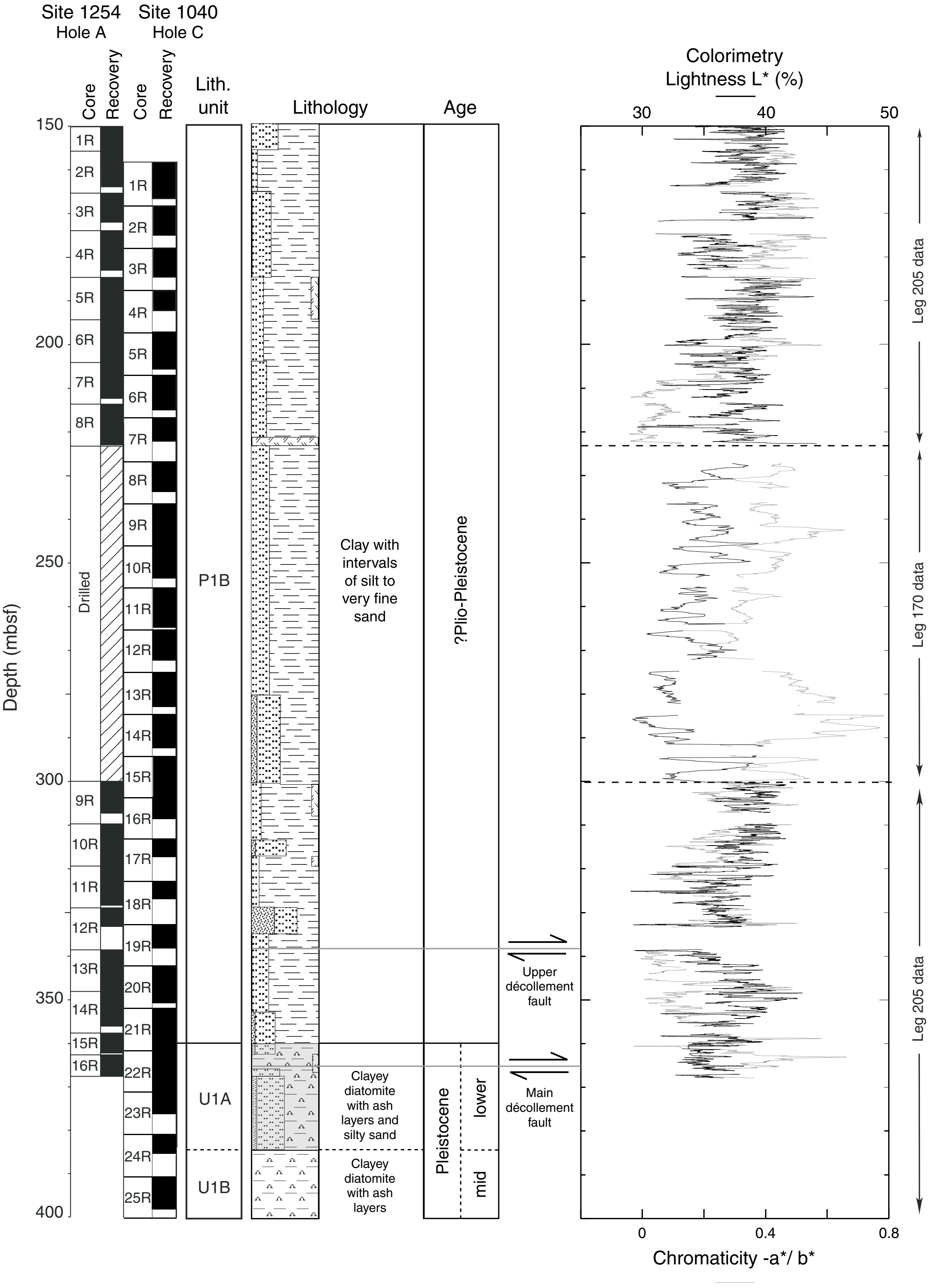

Figure F9. Close-up photograph of interval 205-1254A-3R-3, 45–60 cm. This interval, like much of the sediment at Site 1254, comprises claystone and silt with a diffuse thin interbed of altered volcanic ash seen at 49–47 cm.

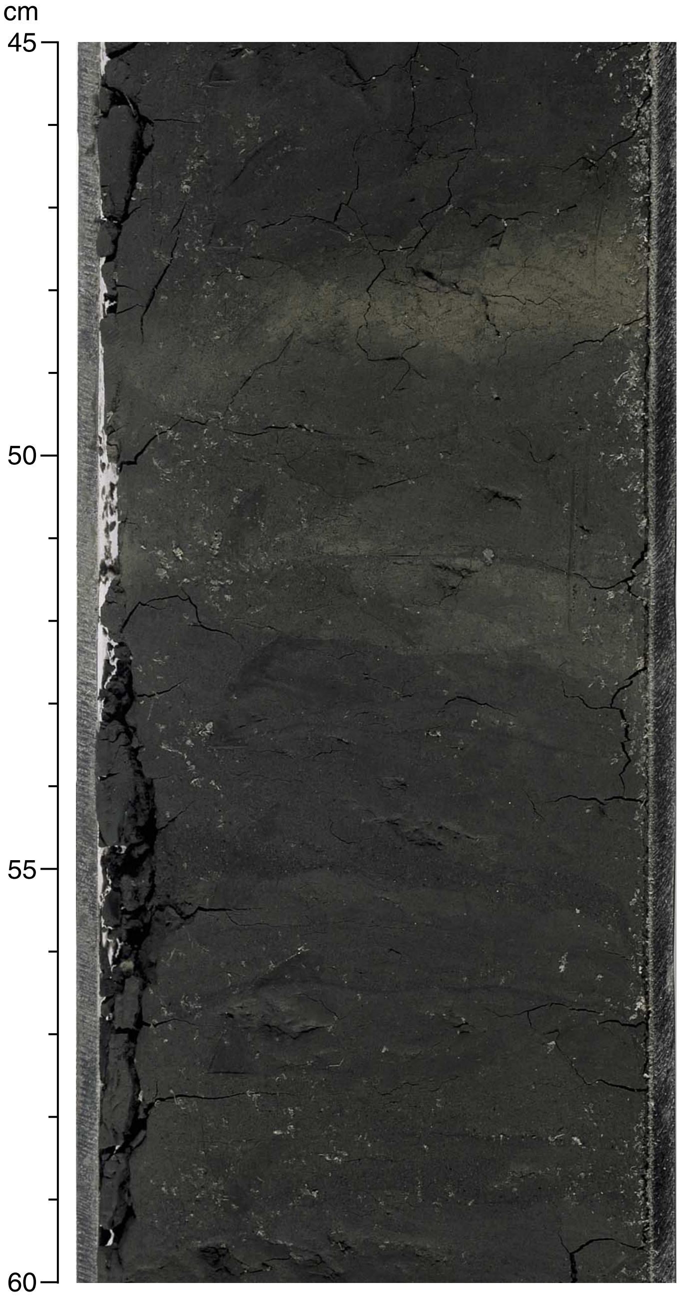

Figure F10. Photomicrographs of sediments recovered at Site 1254. **A.** Silty claystone typical of much of the section (Sample 205-1254A-15R-2, 40 cm). **B.** Volcanic ash (Sample 205-1254A-8R-8, 60 cm) dominated by clear, angular high-silica glass shards (Sample 205-1254A-8R-8, 60 cm). **C.** Volcanic ash-rich siltstone (Sample 205-1254A-4R-3, 25 cm). Note the dark-colored mafic character of the shards. **D.** Claystone with silt bearing minor amounts of diatom and radiolarian tests (Sample 205-1254A-14R-5, 40 cm). **E.** Diatom-rich silty claystone from the underthrust Unit U1 (Sample 205-1254A-15R-4, 50 cm).

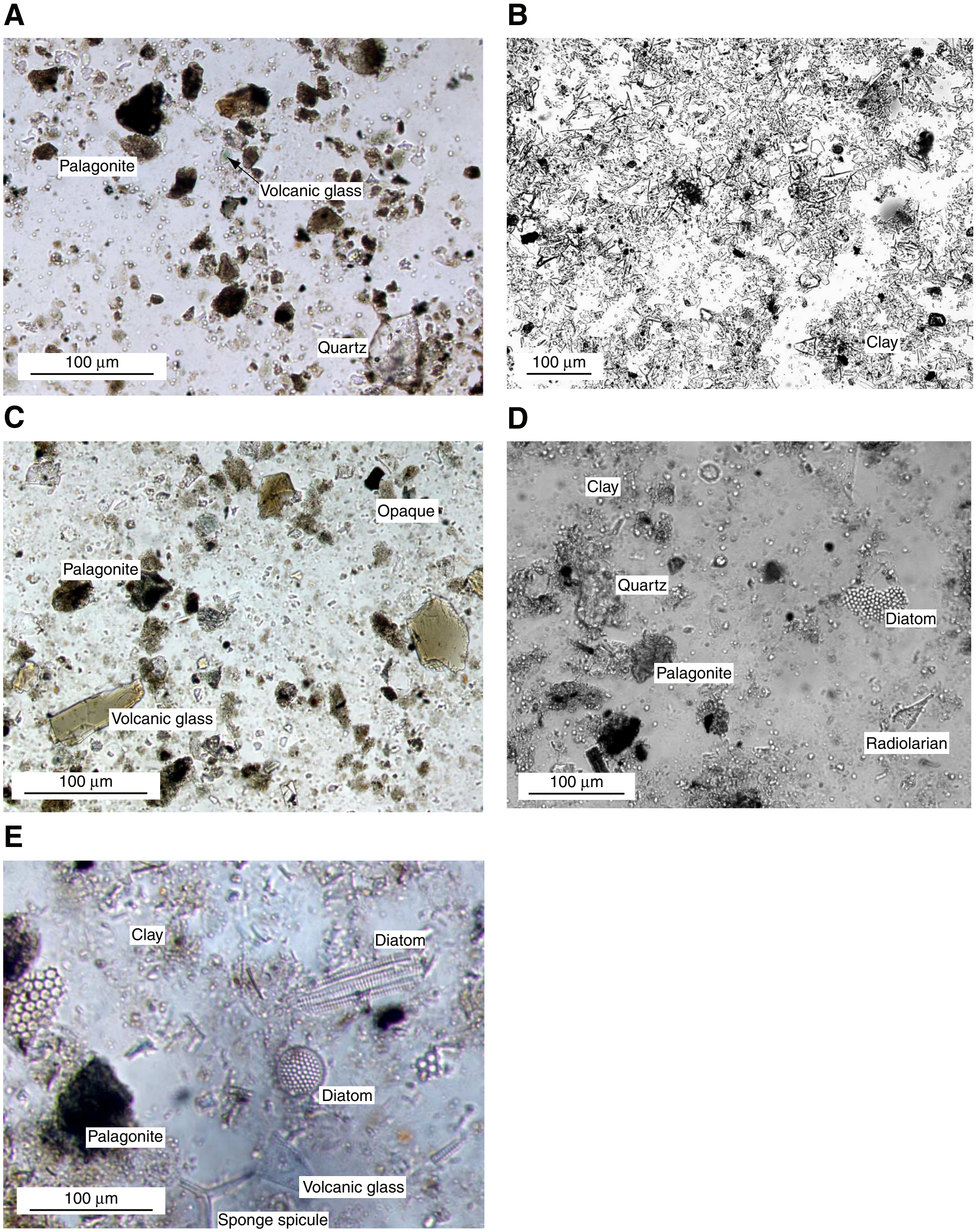

Figure F11. Close-up photograph showing part of a sandy interval located 29 m above the lithologic boundary between Units P1B and U1A (interval 205-1254A-12R-3, 74–91 cm). Sand developed at Site 1254 is typically massive but may have weakly formed parallel laminations as seen here.

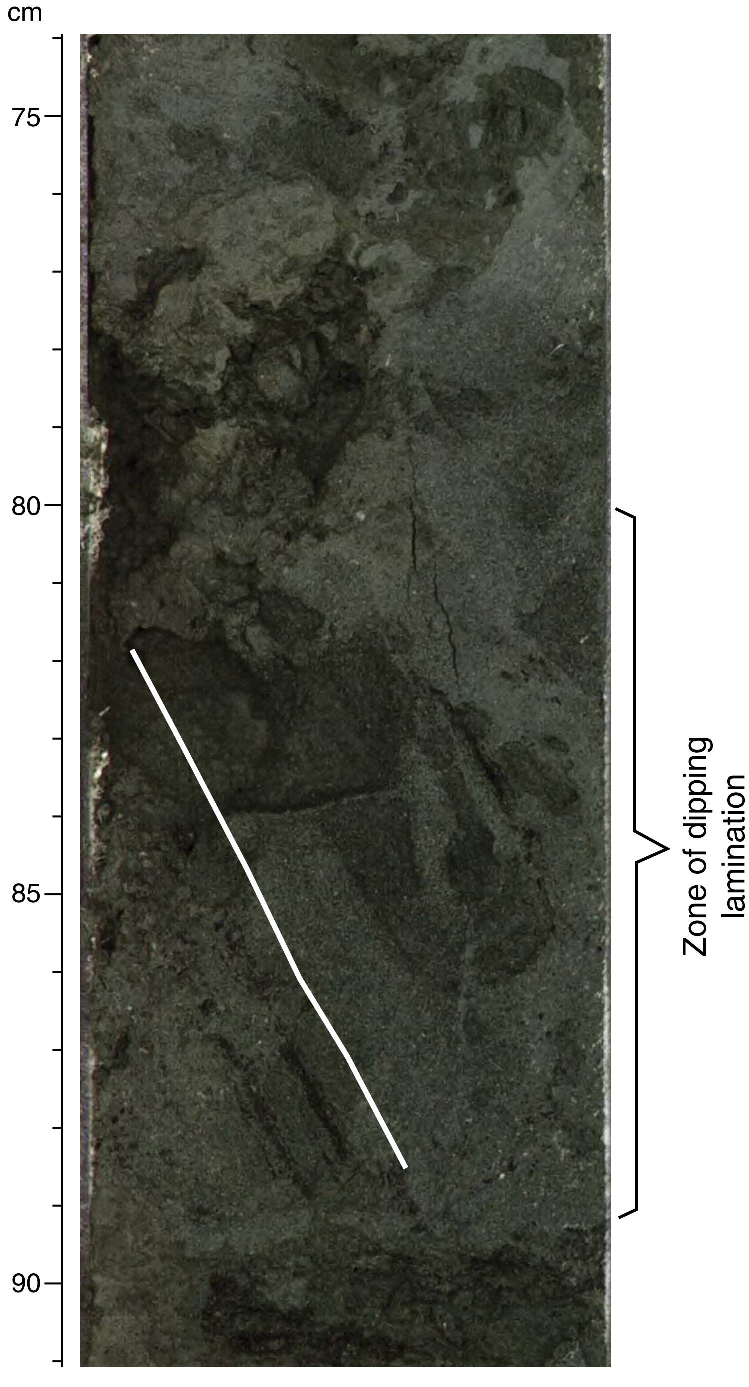

Figure F12. Smear slide data for Sites 1254 and 1040 are reported here from 100 to 400 mbsf. Only abundant (>30%) cases are reported for sand, clay, and volcanic glass; common (>5%) levels of abundance are also included for diatoms and nannofossils. Lithostratigraphic Subunits P1B and U1A were defined at Site 1040 but are adjusted to the depth at which the transition was recorded at Site 1254.

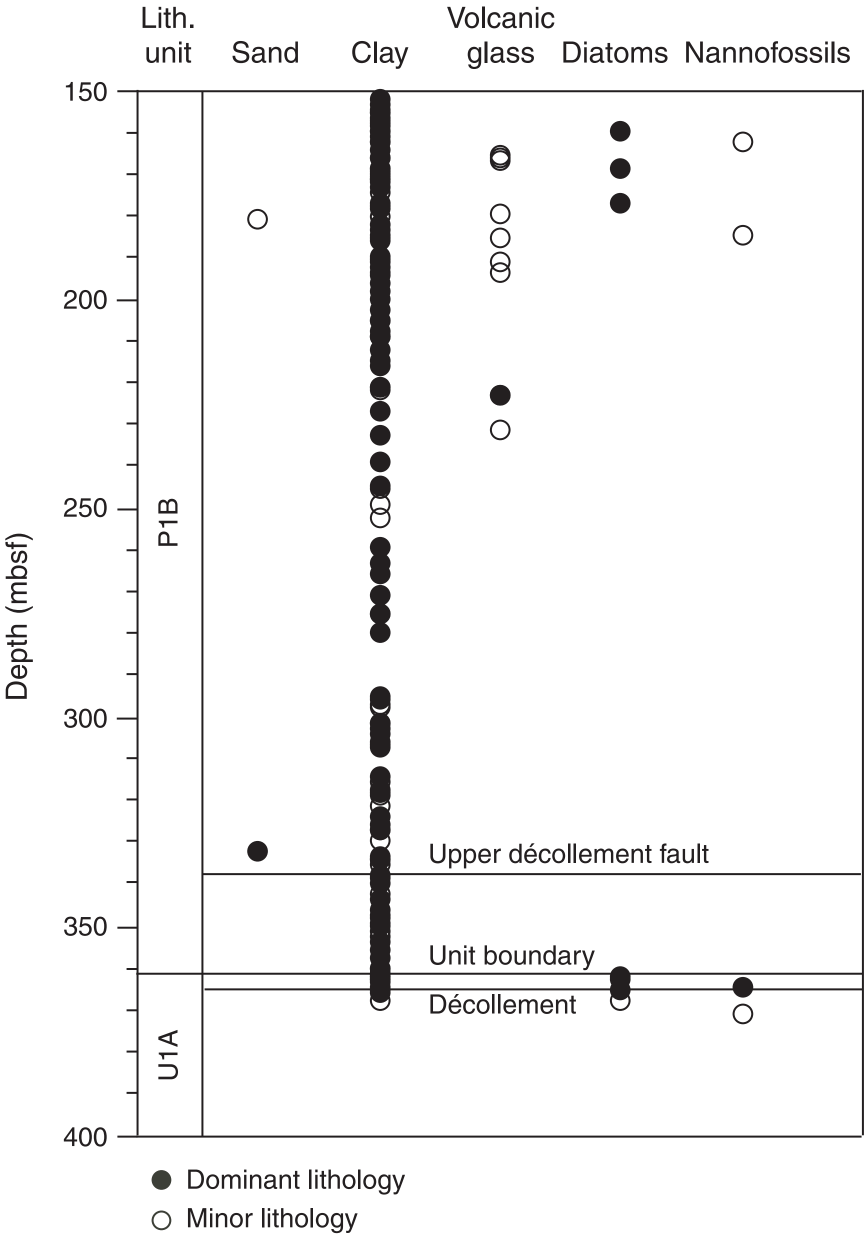

Figure F13. Close-up photograph showing a light tan cobble of limestone, interpreted as a block redeposited into the lower trench slope after sedimentation and lithification close to the coast (interval 205-1254A-7R-4, 49–57 cm). The cobble is brecciated around the edge because of fracturing during drilling recovery.

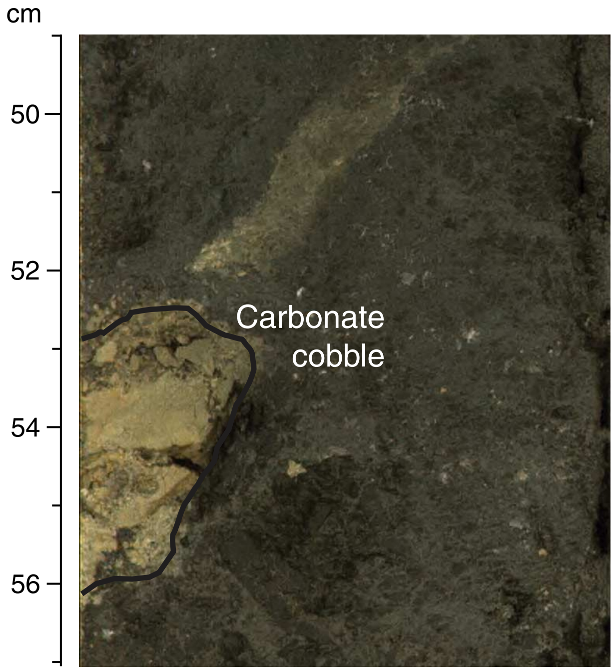

Figure F14. Photomicrographs of a thin section cut from a cobble of carbonate (Sample 205-1254A-14R-CC, 24 cm). **A.** Pelsparite limestone, which is a carbonate facies typically associated with deposits in shallow-shelf, relatively high energy marine conditions. **B.** Test of a bivalve surrounded by a micritic sandstone that has grains dominated by altered volcanic rock and quartz. **C.** Close-up of the sparry calcite cement found between the peloids of the limestones. Note the radiating fans associated with precipitation in a fully marine environment. **D.** A small gastropod within micritic sandstone.

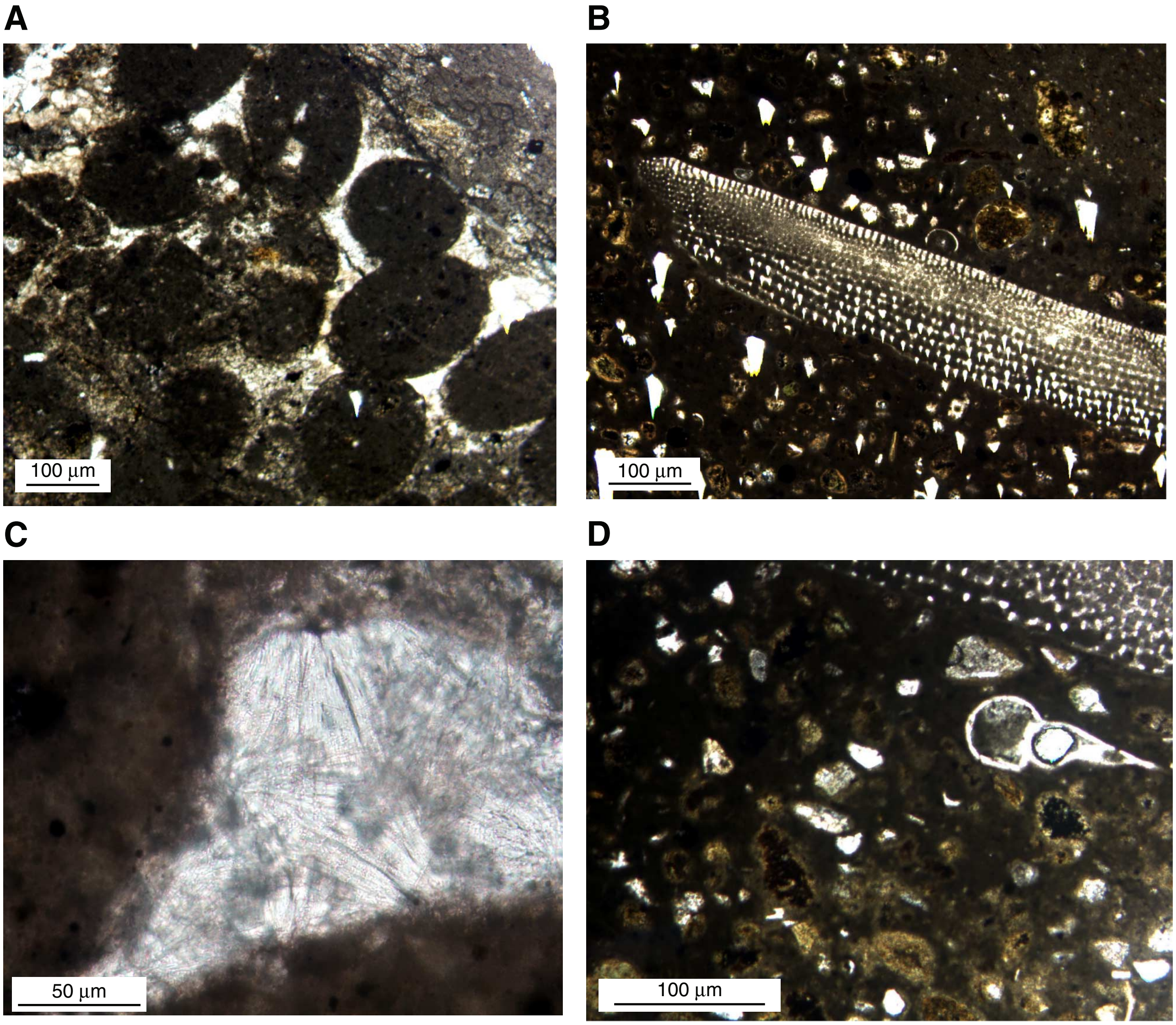

Figure F15. Close-up photograph showing the only major siliceous tephra layer found at Site 1254 (interval 205-1254A-8R-8, 20–66 cm). The bed displays a reverse grading and has sharp contact with the overlying claystone.

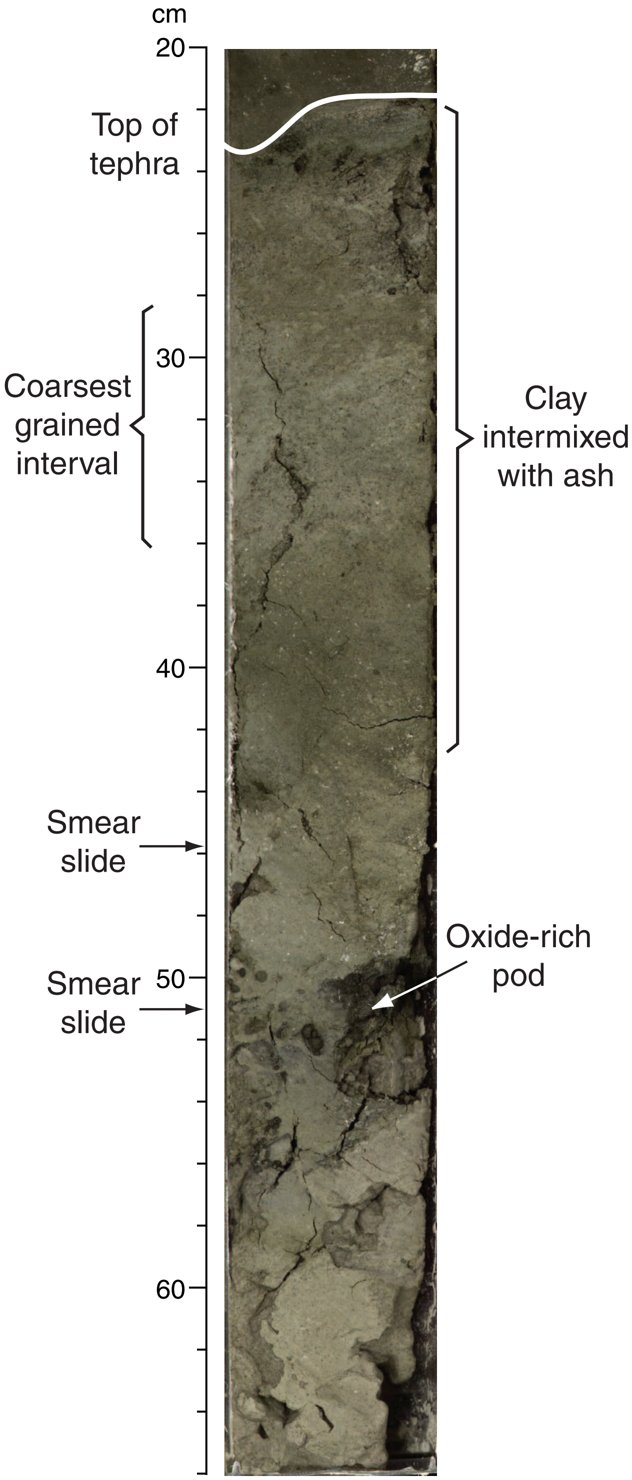

Figure F16. A. Figure (modified after Ninkovich et al., 1978) showing the relationship between tephra maximum grain size in a series of major eruptions compared to the tephra in Sample 205-1254A-8R-8, 22–65 cm. **B.** Median diameter of the particles from the coarsest part of the tephra in Sample 205-1254A-8R-8, 22–65 cm, compared to that found in Sample 205-1253A-4R-3, 85–93 cm, and the limits defined by Walker (1971) from his compilation of tephra data.

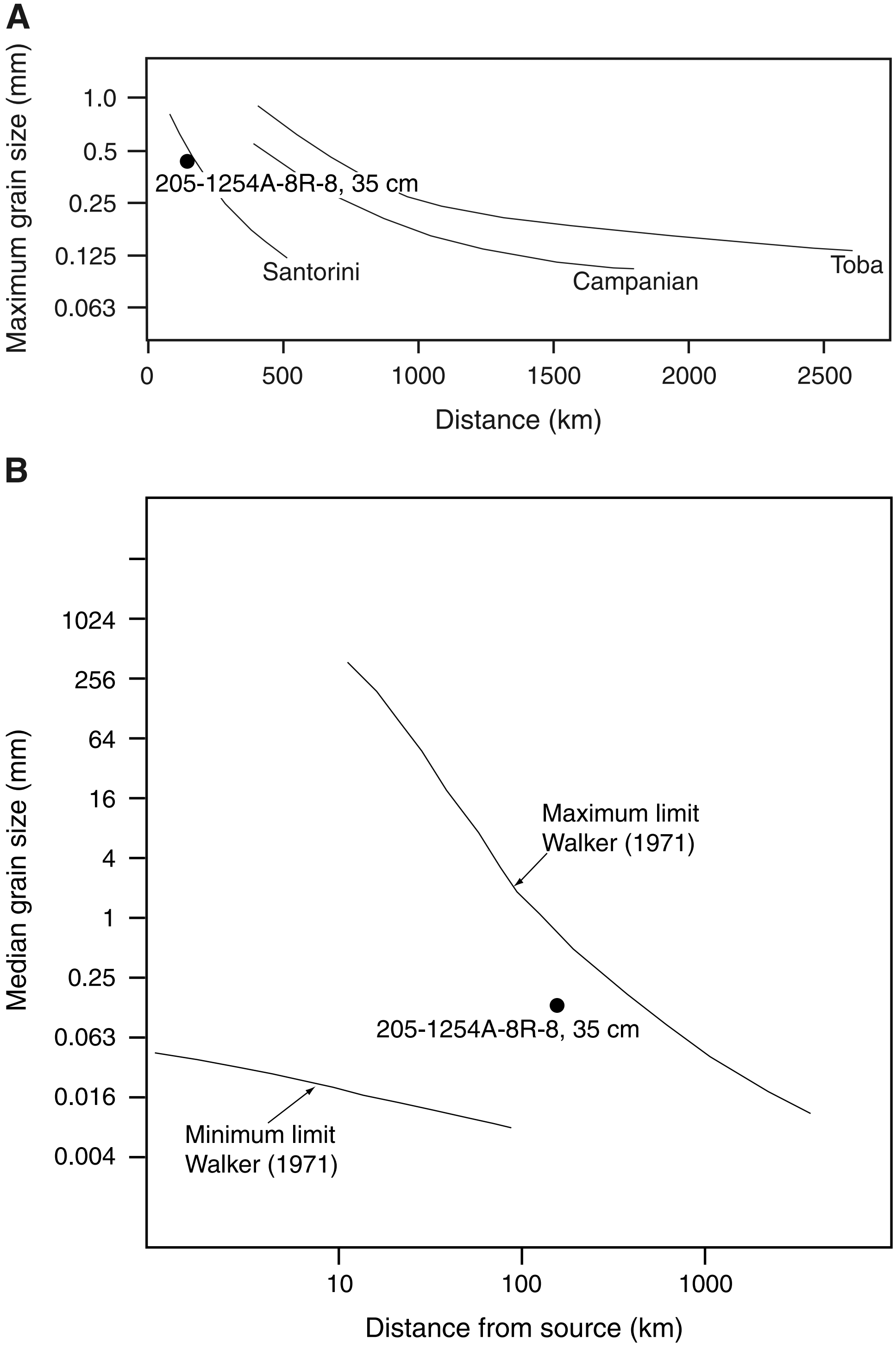

Figure F17. Diagrams showing the variations in elemental concentrations vs. depth for bulk sediment at Site 1254 for (**A**) TiO_2, (**B**) Al_2O_3, (**C**) SiO_2, and (**D**) Ti/Al. Black circles = sediments, open circles = a tephra layer.

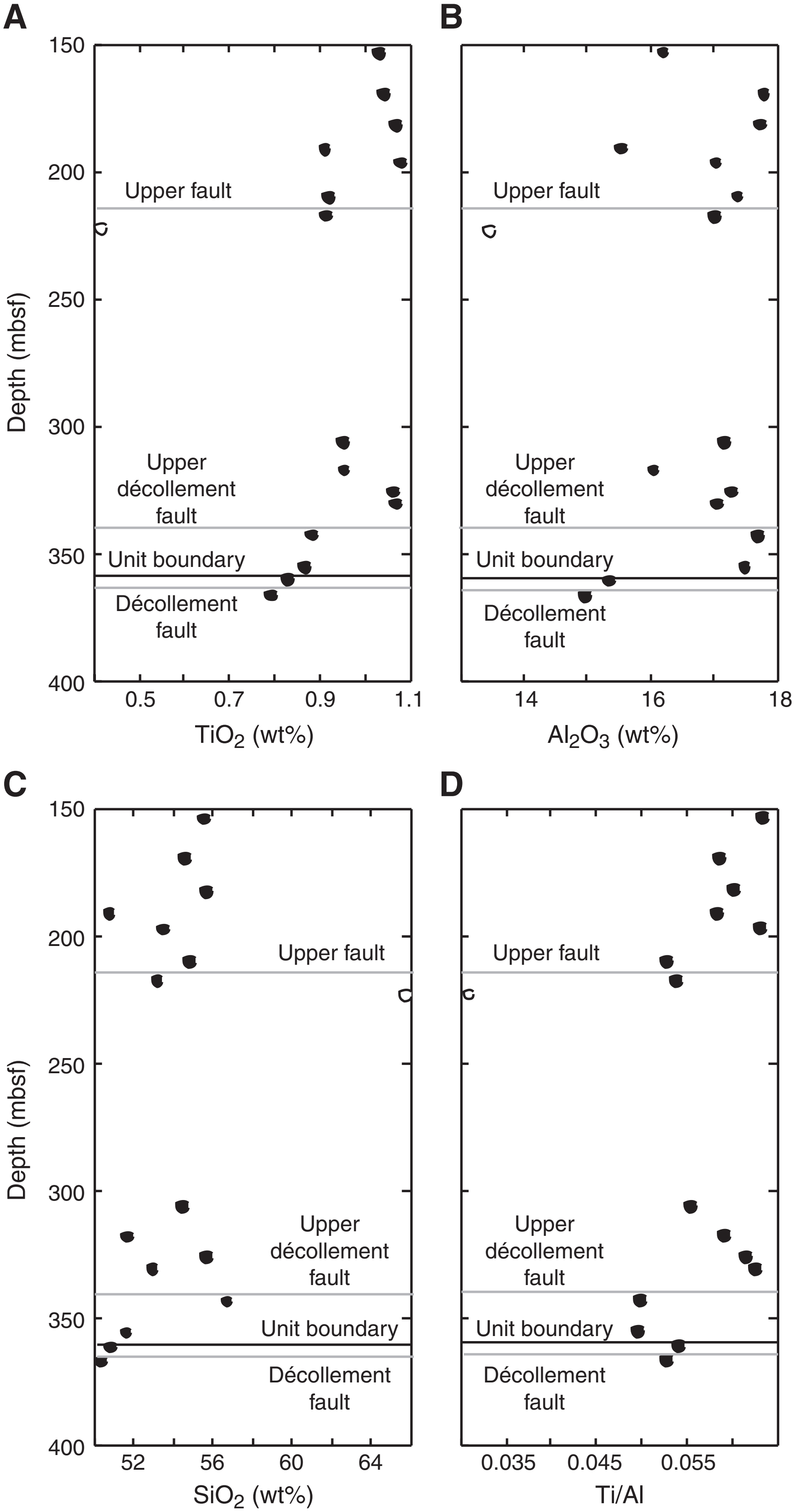

Figure F18. Depth profiles of (**A**) Na_2O and (**B**) K_2O concentrations at Site 1254. Black circles = sediments, open circles = a tephra layer.

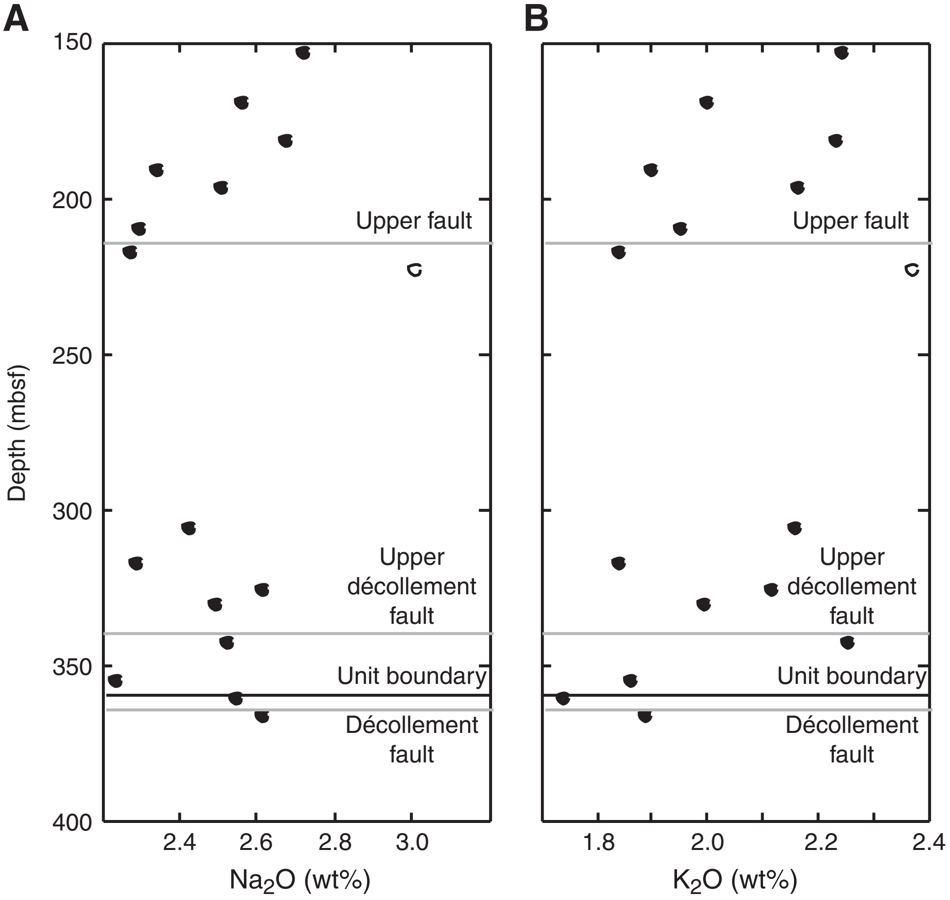

Figure F19. Depth profiles of (**A**) CaO, (**B**) MgO, (**C**) Sr, and (**D**) Ba concentrations at Site 1254. Black circles = sediments, open circles = a tephra layer.

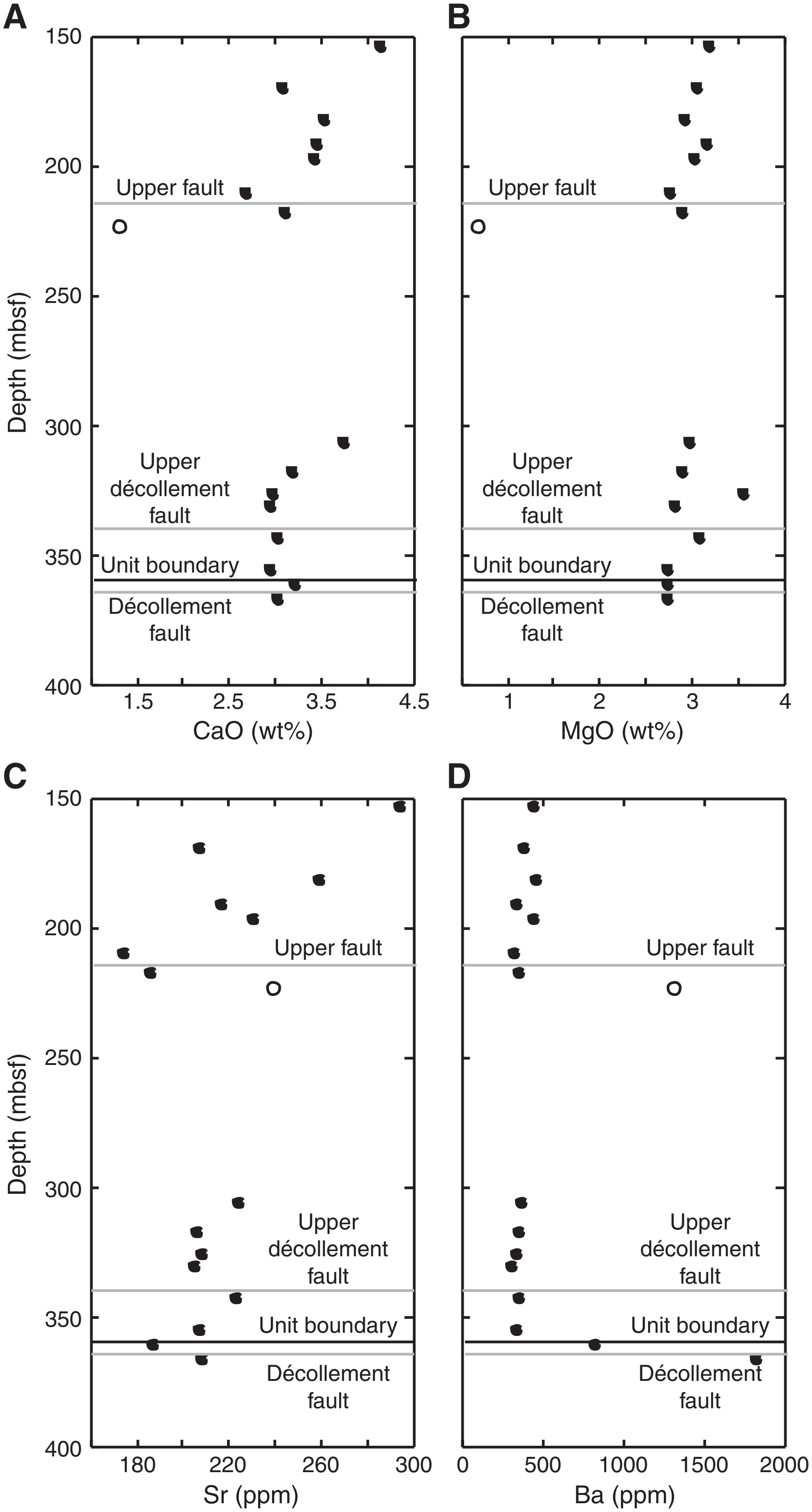

Figure F20. Discrimination plots (from Middlemost, 1975) showing (**A**) the classification of the tephra from Sample 205-1254A-8R-8, 22–65 cm, as tholeiite, whereas (**B**) shows that this tephra is derived from a medium-K liquid.

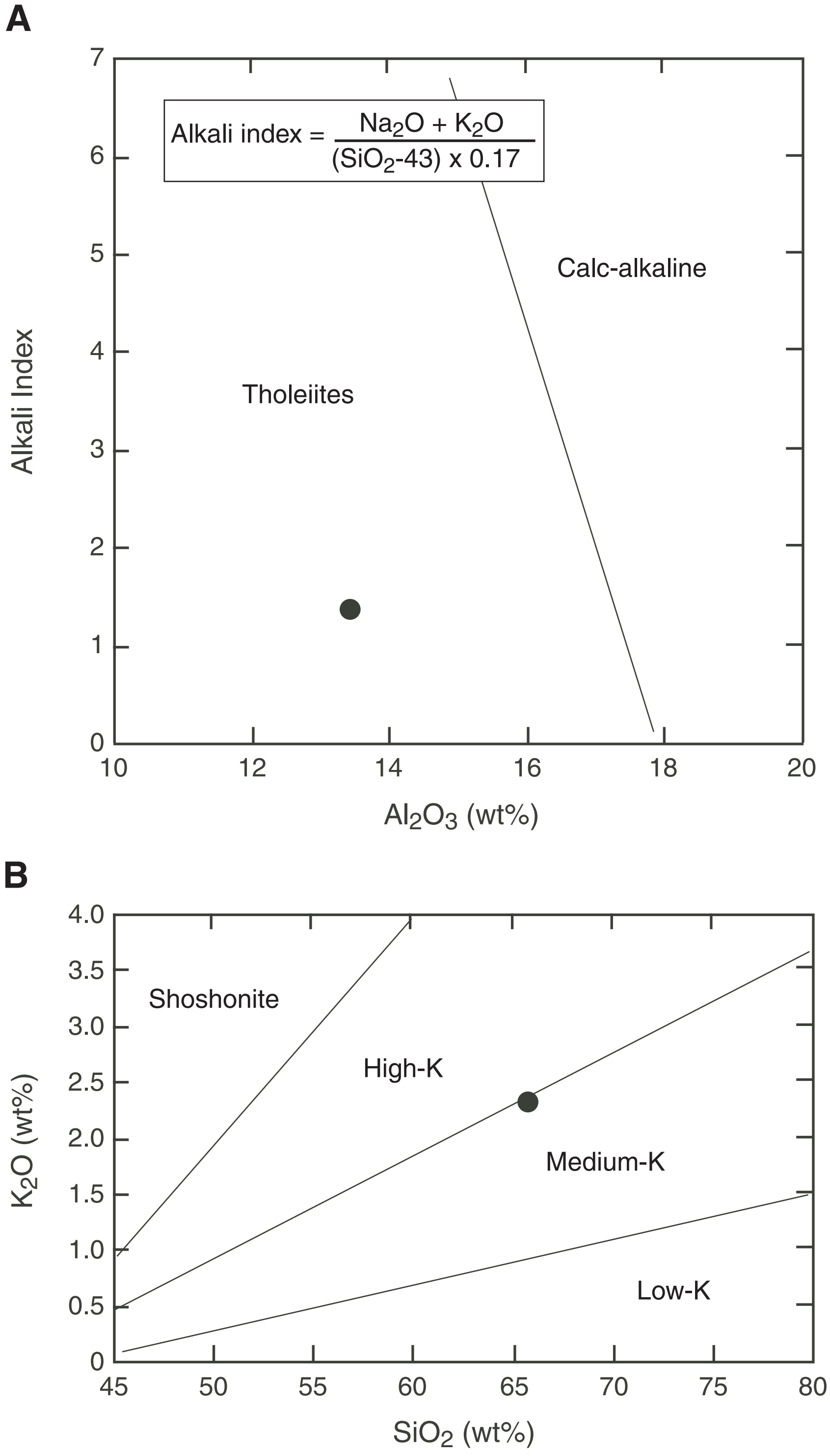

Figure F21. Close-up photograph showing the development of light tan-colored carbonate concretions within the dominant claystone lithology (interval 205-1254A-8R-1, 43–54 cm).

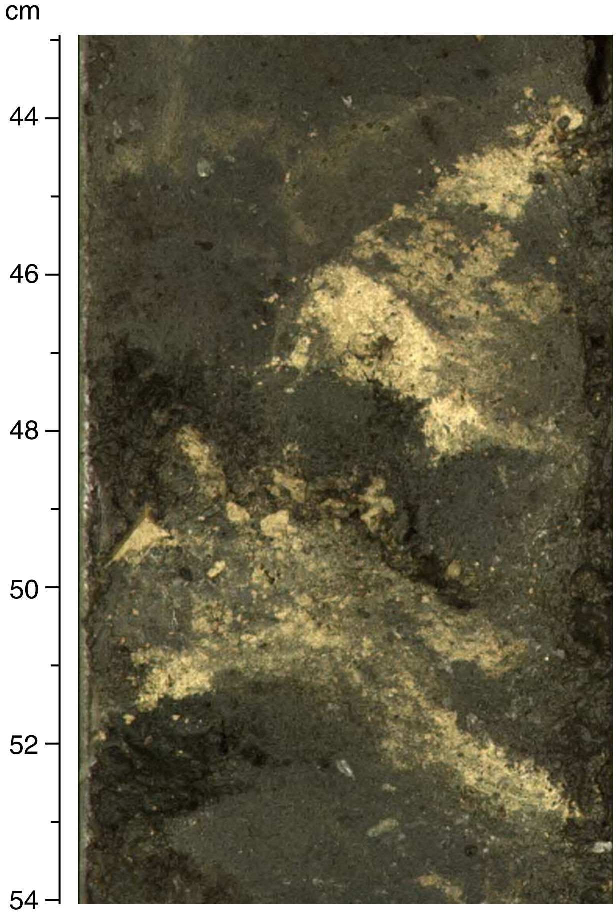

Figure F22. Calculated relative abundances of smectite, illite, and kaolinite/chlorite in selected intervals from Hole 1254A based on X-ray diffraction analyses of oriented aggregate clay slides. Solid circles = smectite, solid squares = illite, solid triangles = kaolinite.

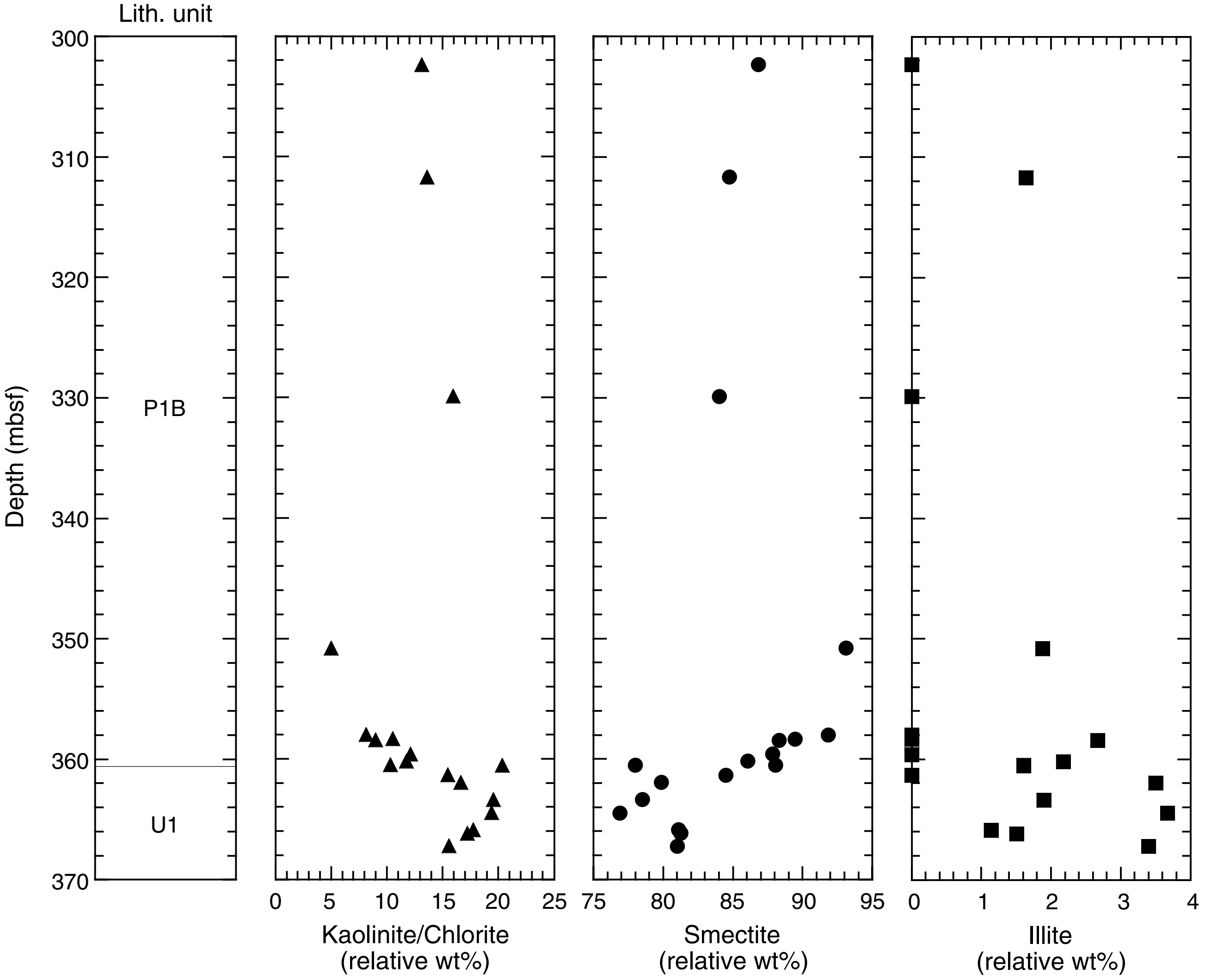

Figure F23. Structural and lithologic summary across the décollement zone. The density of fracturing is shown by the nature and size of the brecciated fragments. Most of the fracture surfaces are slickensided and slickenlined. Note the trend of increasing fracturing downward through the décollement zone, peaking a few meters above its base.

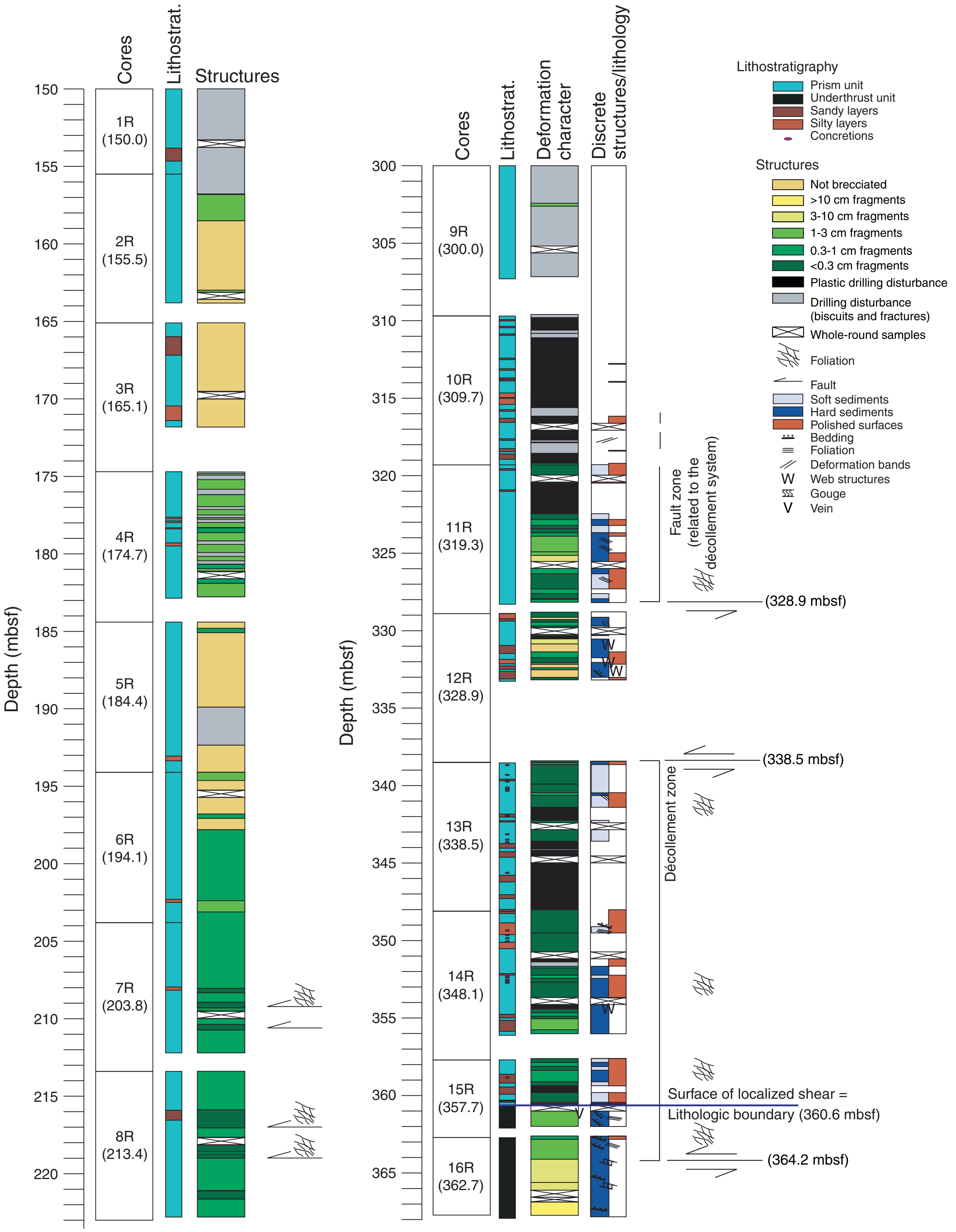

Figure F24. (**A**) Distribution of bedding dips and (**B**) stereographic projection (equal area and lower hemisphere) of bedding azimuth in the prism fault zone.

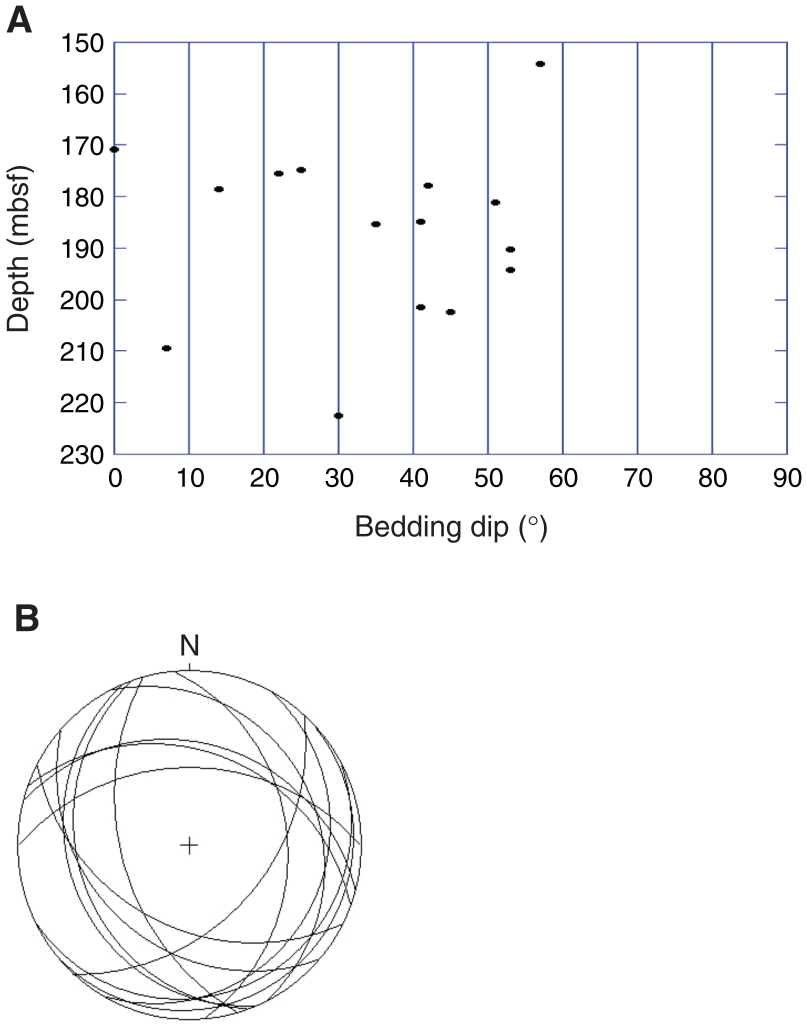

Figure F25. Stereographic plot (equal area and lower hemisphere) of the foliation and Riedel shear surfaces defining the reverse faults in the interval 205-1254A-8R-5, 0–24 cm. The black-and-white split symbols indicate the sense of movement along the plane (black = down, white = up).

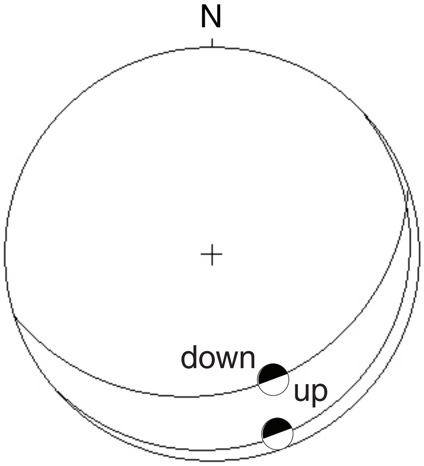

Figure F26. (**A**) Distribution of bedding dips and (**B**) stereographic projection (equal area and lower hemisphere) of bedding azimuth in the décollement zone.

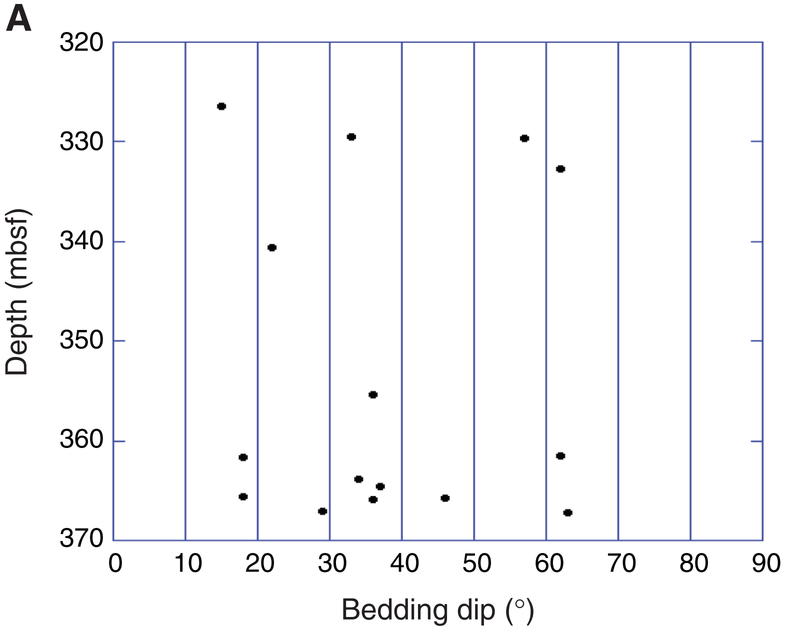

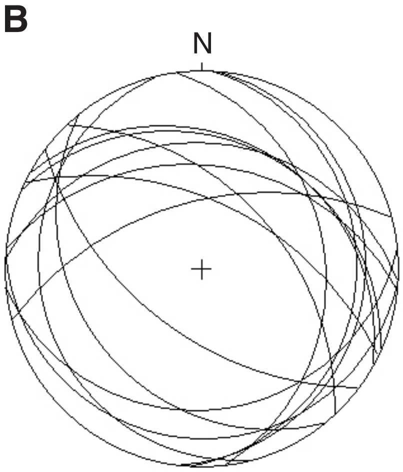

Figure F27. Close-up photograph of the equidimensional breccia (interval 205-1254A-11R-5, 35–50 cm).

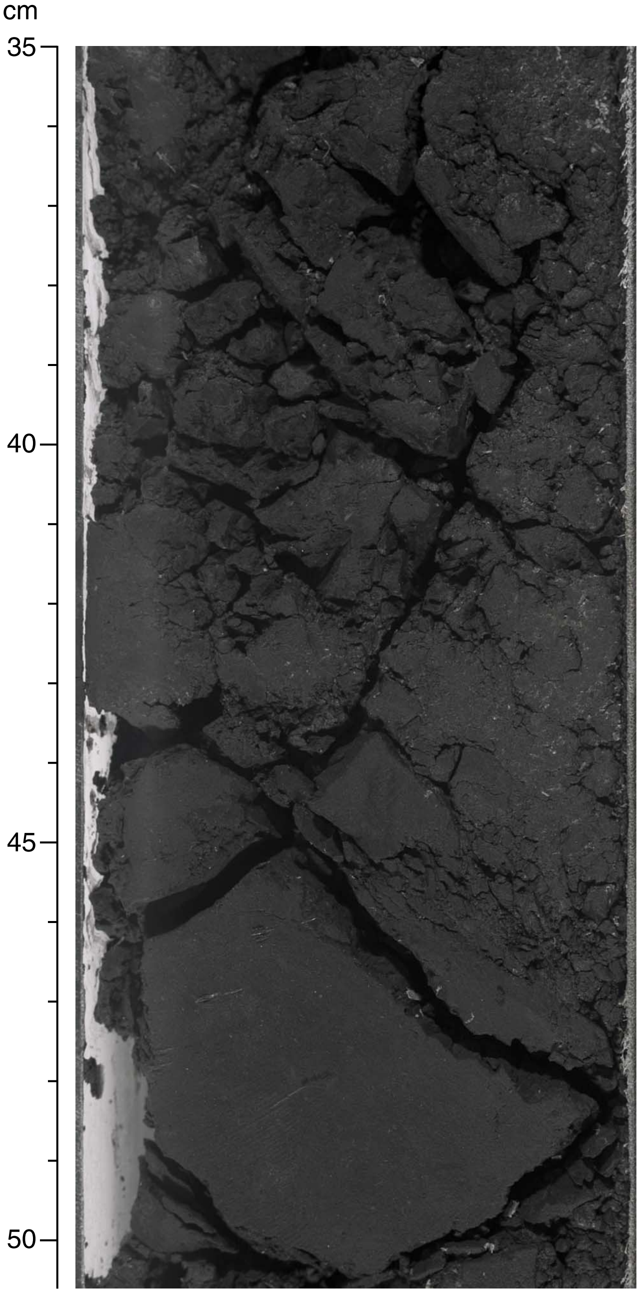

Figure F28. Stereographic projection (equal area and lower hemisphere) of brittle shear zone boundaries in the zone of localized deformation below the décollement zone.

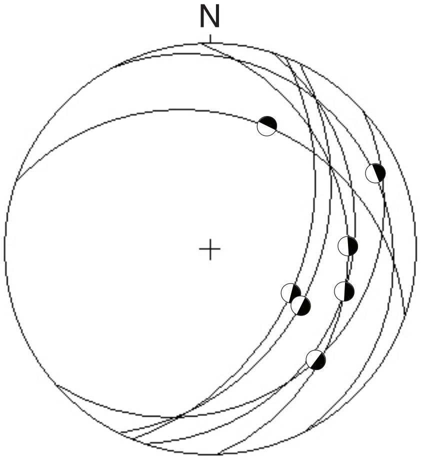

Figure F29. **A.** Porosity calculated from wet and dry mass and volume measurements. **B.** Bulk (wet) density. **C.** Close-up of porosity through décollement zone. **D.** Close-up of bulk density through the décollement zone. Gray shading = the structurally defined décollement zone.

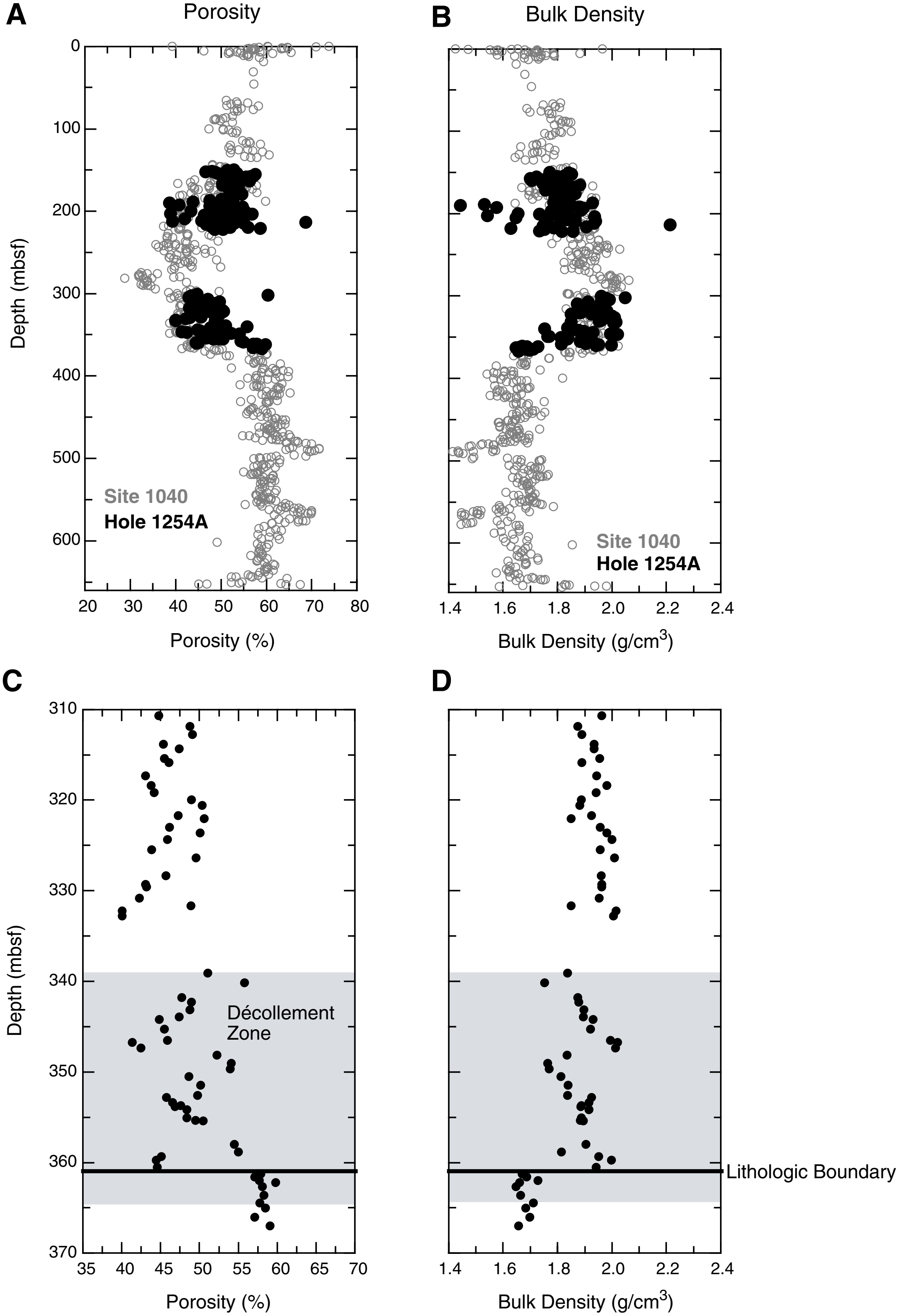

Figure F30. Corrected GRA bulk density (black symbols) and moisture and density bulk density (red symbols).

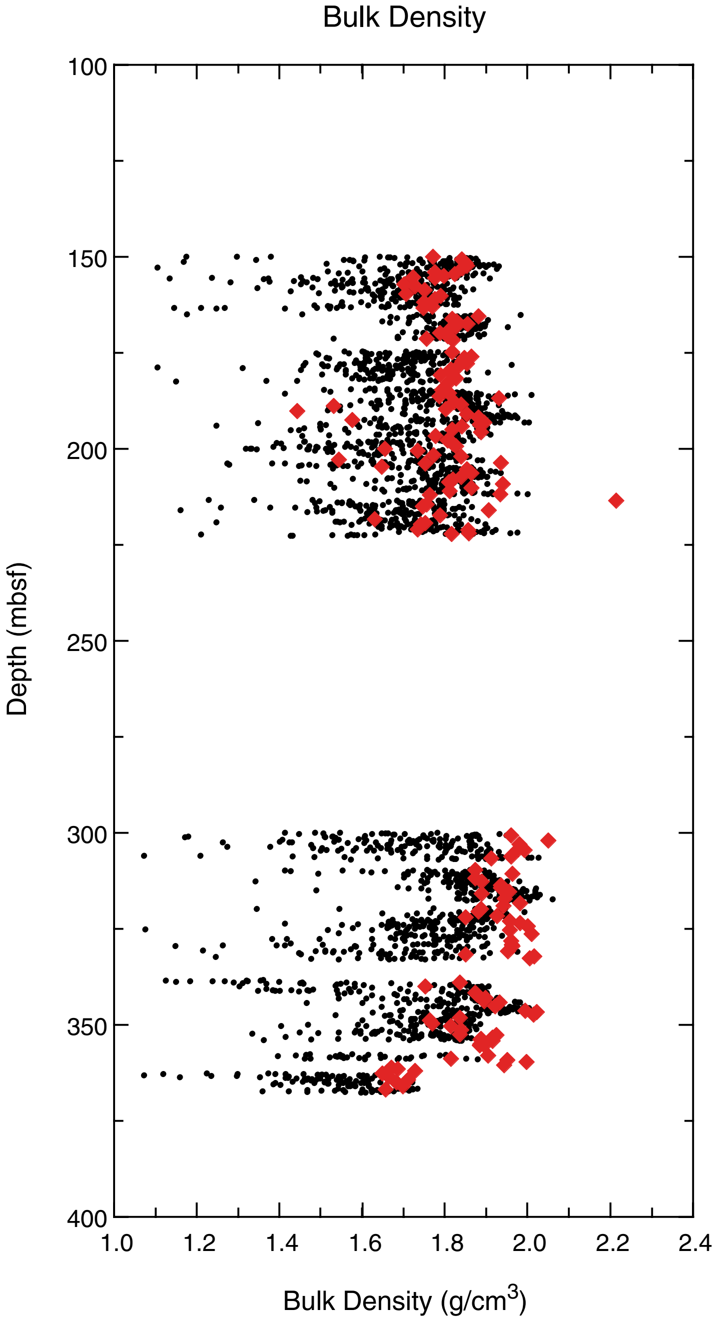

Figure F31. Grain densities determined from dry mass and volume measurements.

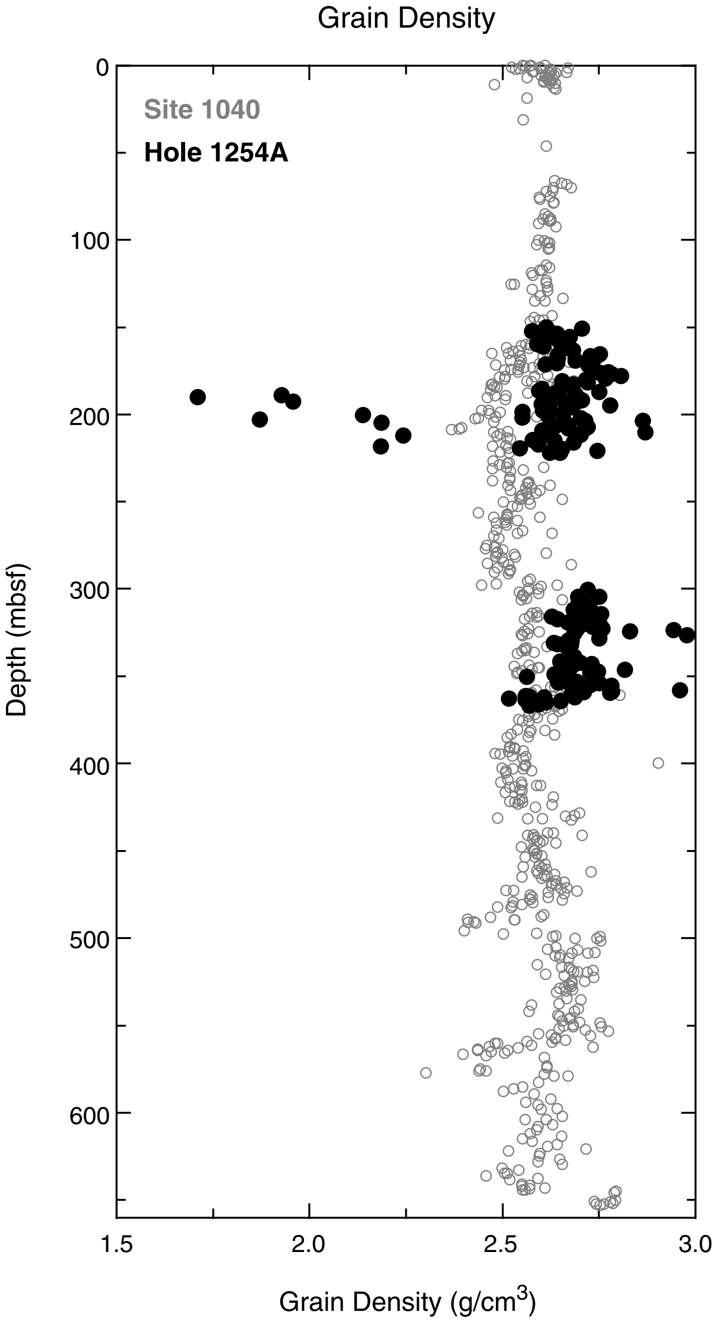

Figure F32. **A.** Porosity calculated from wet and dry mass measurements and a constant grain density of 2.65 g/cm³ (solid circles) and calculated from wet and dry mass and volume measurements at Site 1254 (open circles), as shown in Figure F29A, p. 70. **B.** Bulk density calculated using a constant grain density of 2.65 g/cm³ (solid circles) and using determinations from Site 1254 (open circles).

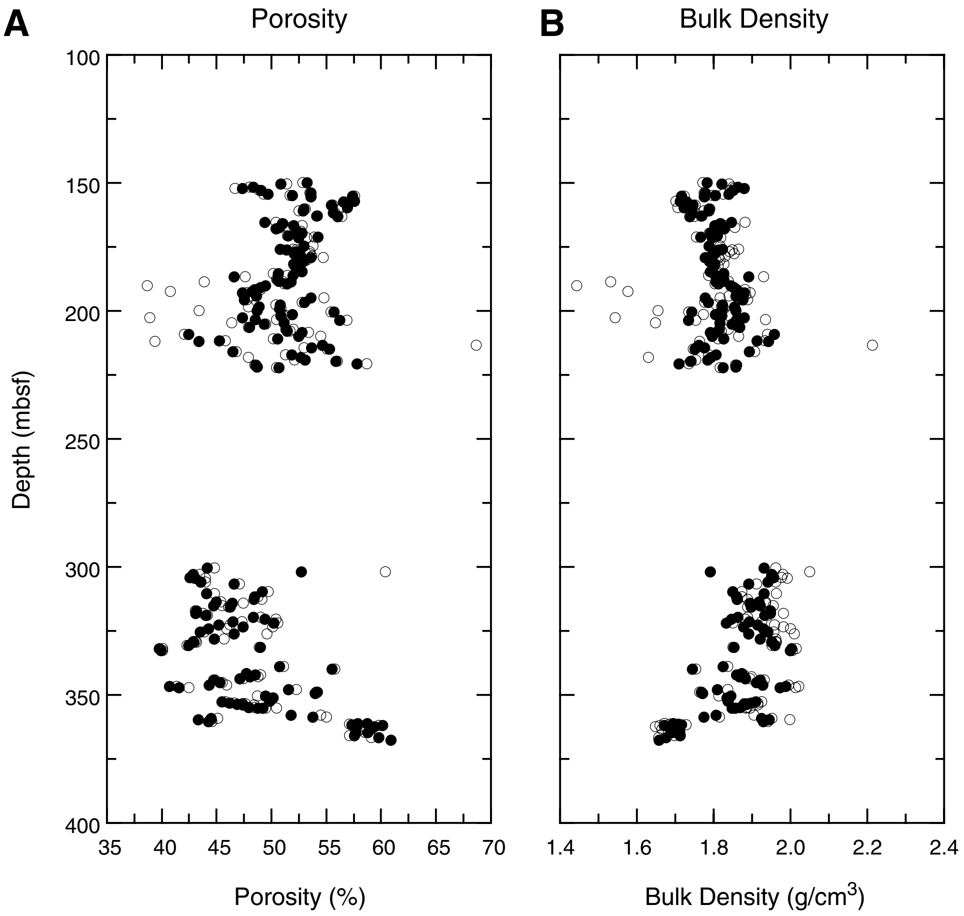

Figure F33. Corrected MST natural gamma ray (NGR) measurements.

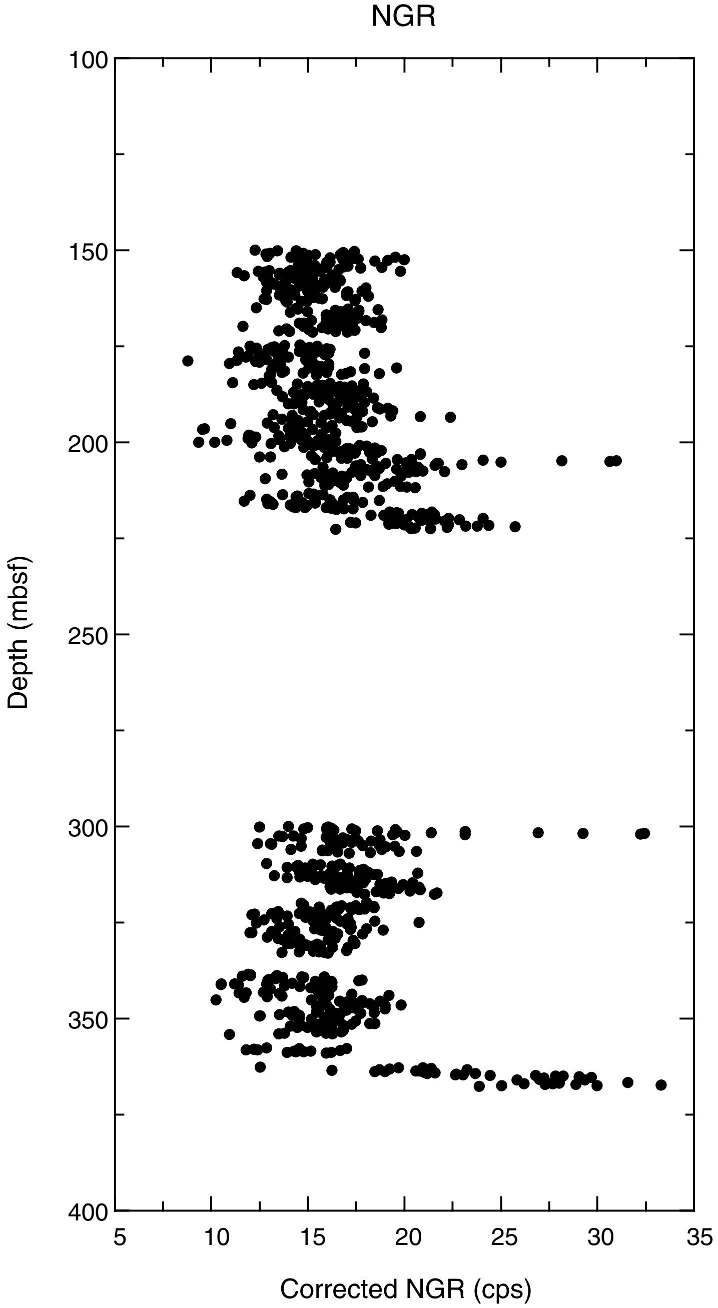

Figure F34. MST volumetric magnetic susceptibility (dimensionless).

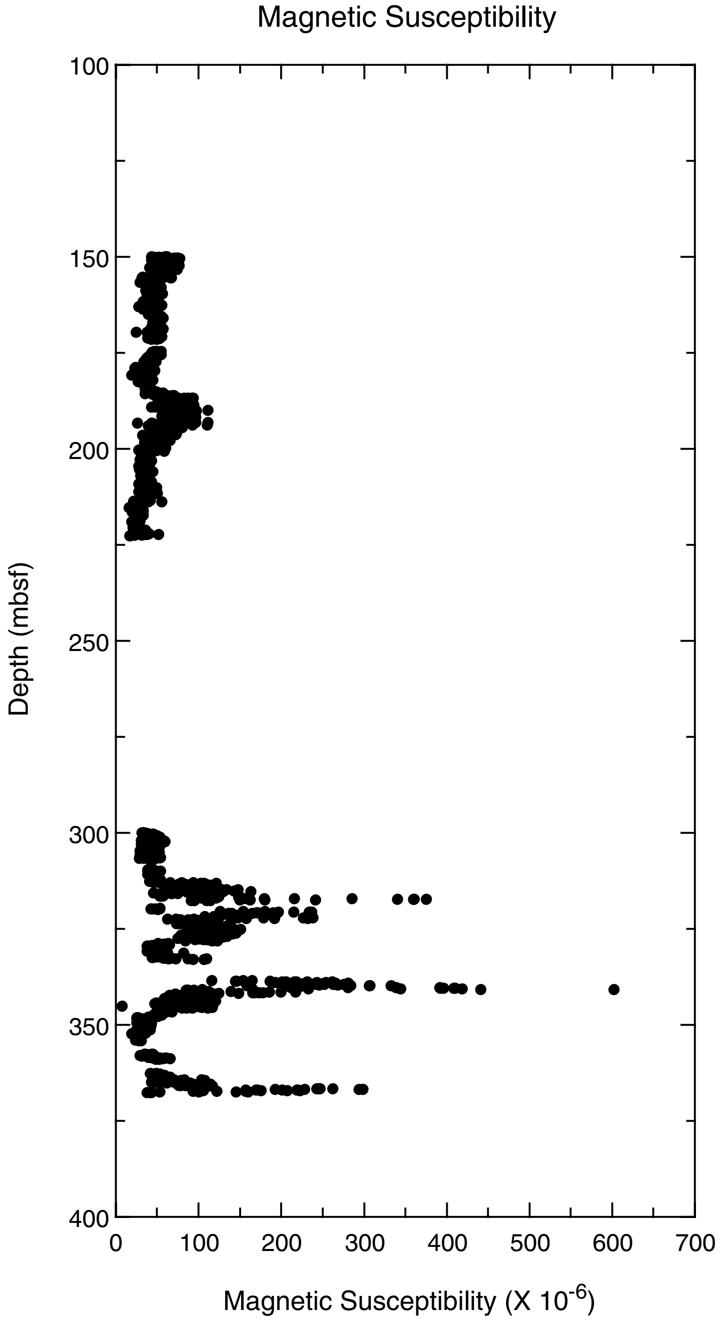

Figure F35. Natural remanent magnetization (NRM) inclination and demagnetized inclinations observed in archive-half samples after alternating-field (AF) demagnetization of 5 and 10 mT.

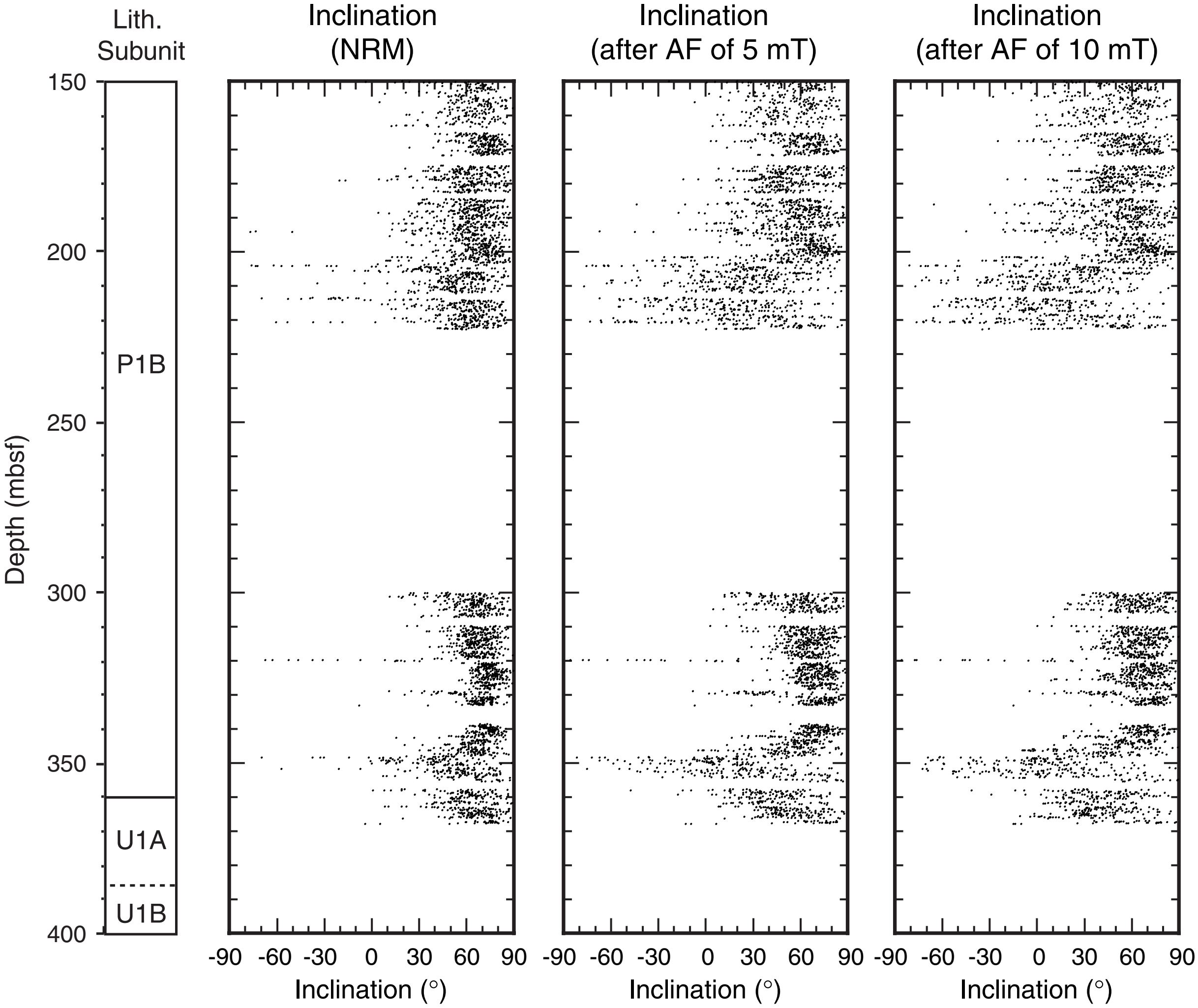

Figure F36. Paleomagnetic results of archive halves from 150 to 230 mbsf (Cores 205-1254A-1R through 8R) after AF demagnetization of 40 mT. Note that magnetic polarity change includes drilling disturbances. Gray zone in polarity column = unclear negative inclination.

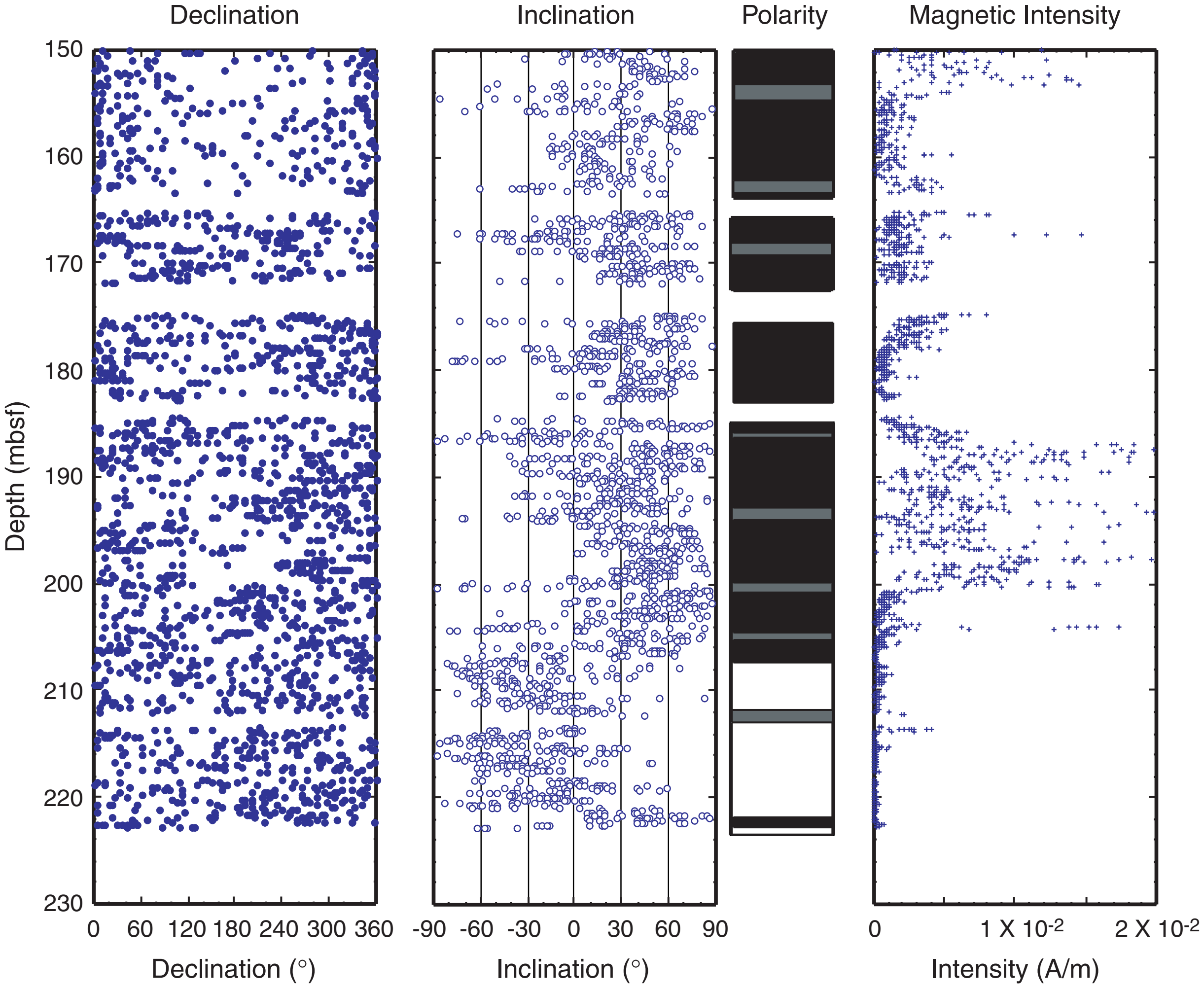

Figure F37. Paleomagnetic results of archive halves from 300 to 370 mbsf (Cores 205-1254A-9R through 16R) after AF demagnetization of 40 mT. Note that magnetic polarity change includes drilling disturbances. Gray zone in polarity column = unclear negative inclination.

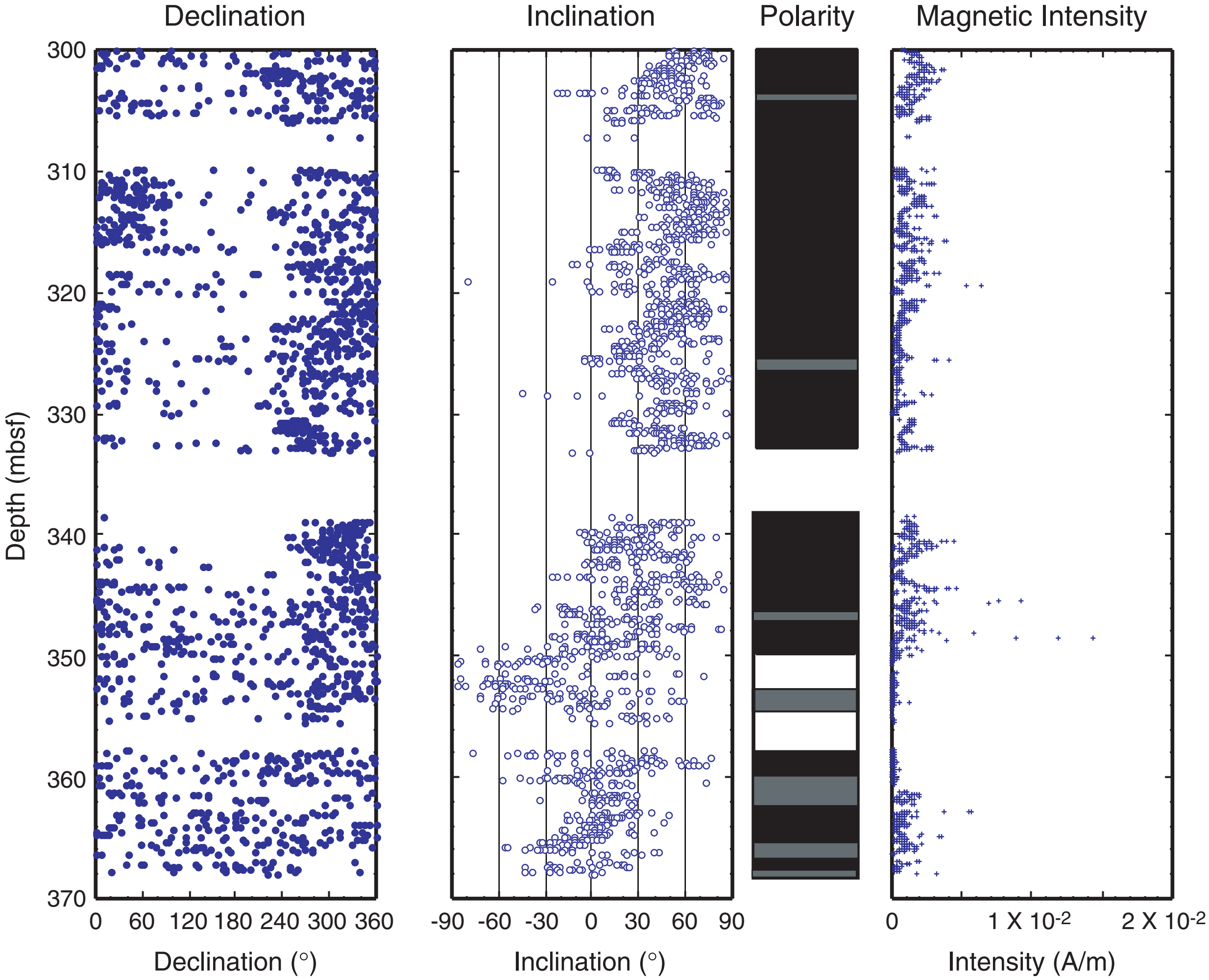

Figure F38. Natural remanent magnetization (NRM) intensity, magnetic intensity after 20 mT, and the ratio of the magnetic intensity after demagnetization to the NRM intensity.

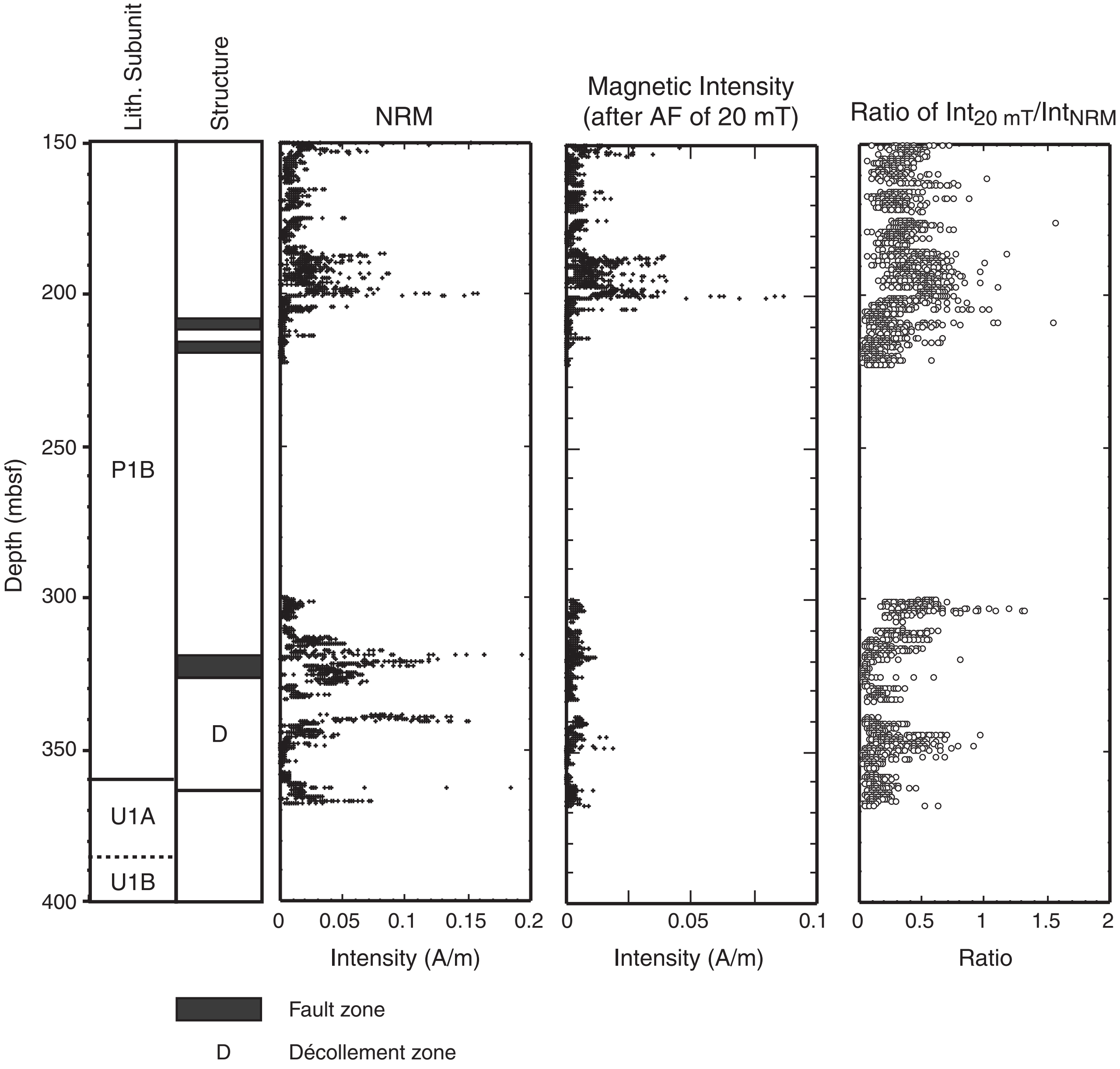

Figure F39. Comparison of magnetic intensity and susceptibilities in Hole 1254A to magnetic susceptibility at Site 1040. NRM = natural remanent magnetization. MST = multisensor track, AMST = archive multisensor track.

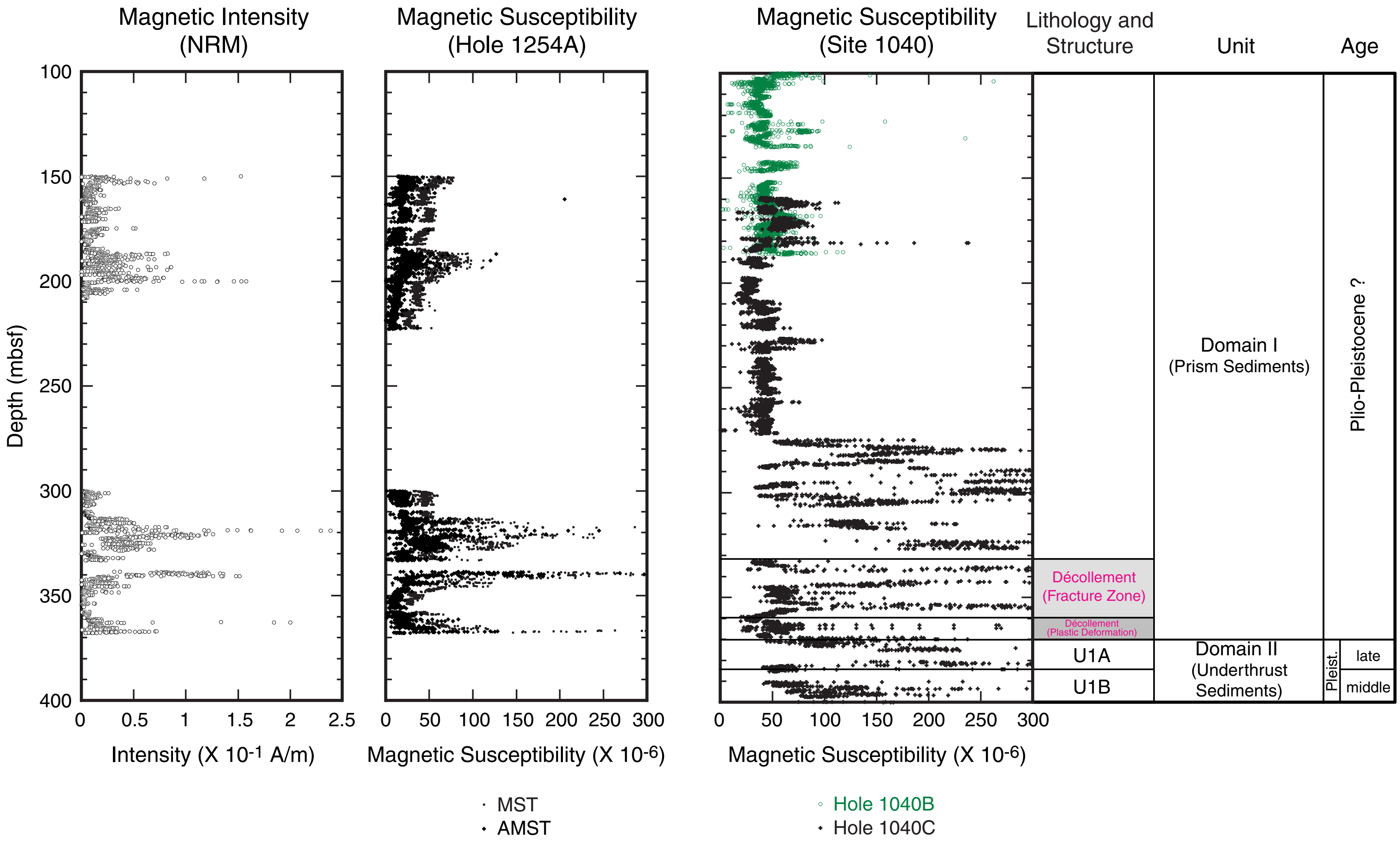

Figure F40. Zijderveld diagrams and demagnetization plots for discrete samples obtained from several intervals in Hole 1254A. **A.** Sediment from above the high-intensity anomaly at ~180 mbsf. **B, C.** Samples obtained from the sediment corresponding to the first and second anomalies (see **"Demagnetization Analyses of Discrete Samples,"** p. 27, in "Paleomagnetism") of the magnetic intensity. **D.** Sample showing low magnetic intensity ratio below the lower anomaly of the magnetic intensity. **E.** Sample from lithostratigraphic Subunit U1A.

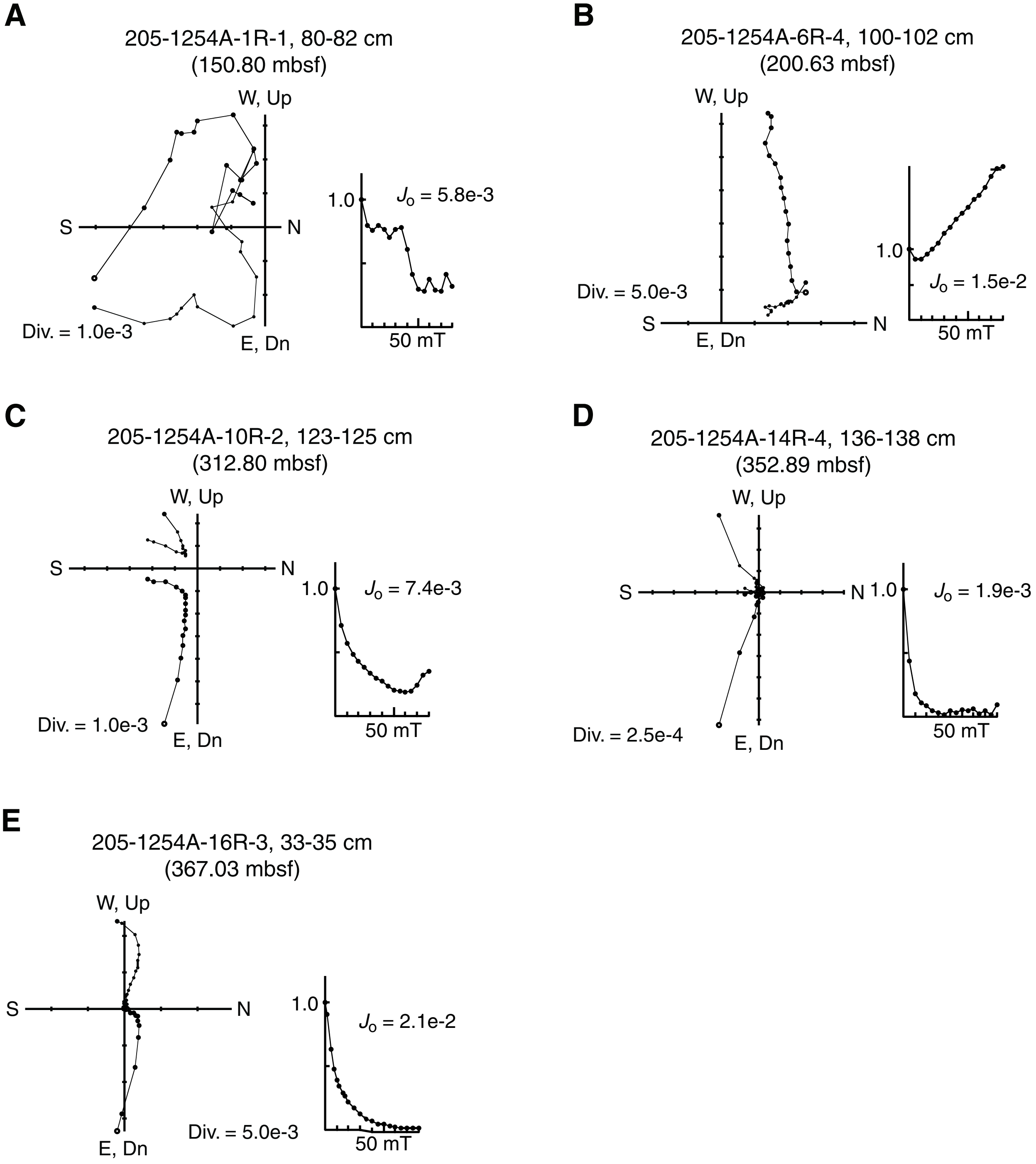

Figure F41. Depth profiles of (**A**) salinity, (**B**) Cl, (**C**) Na, and (**D**) K. Arrows = seawater concentration. Shaded area = the décollement at Site 1254. Error bars are smaller than or comparable to symbol size (see **"Inorganic Geochemistry,"** p. 24, in the "Explanatory Notes" chapter).

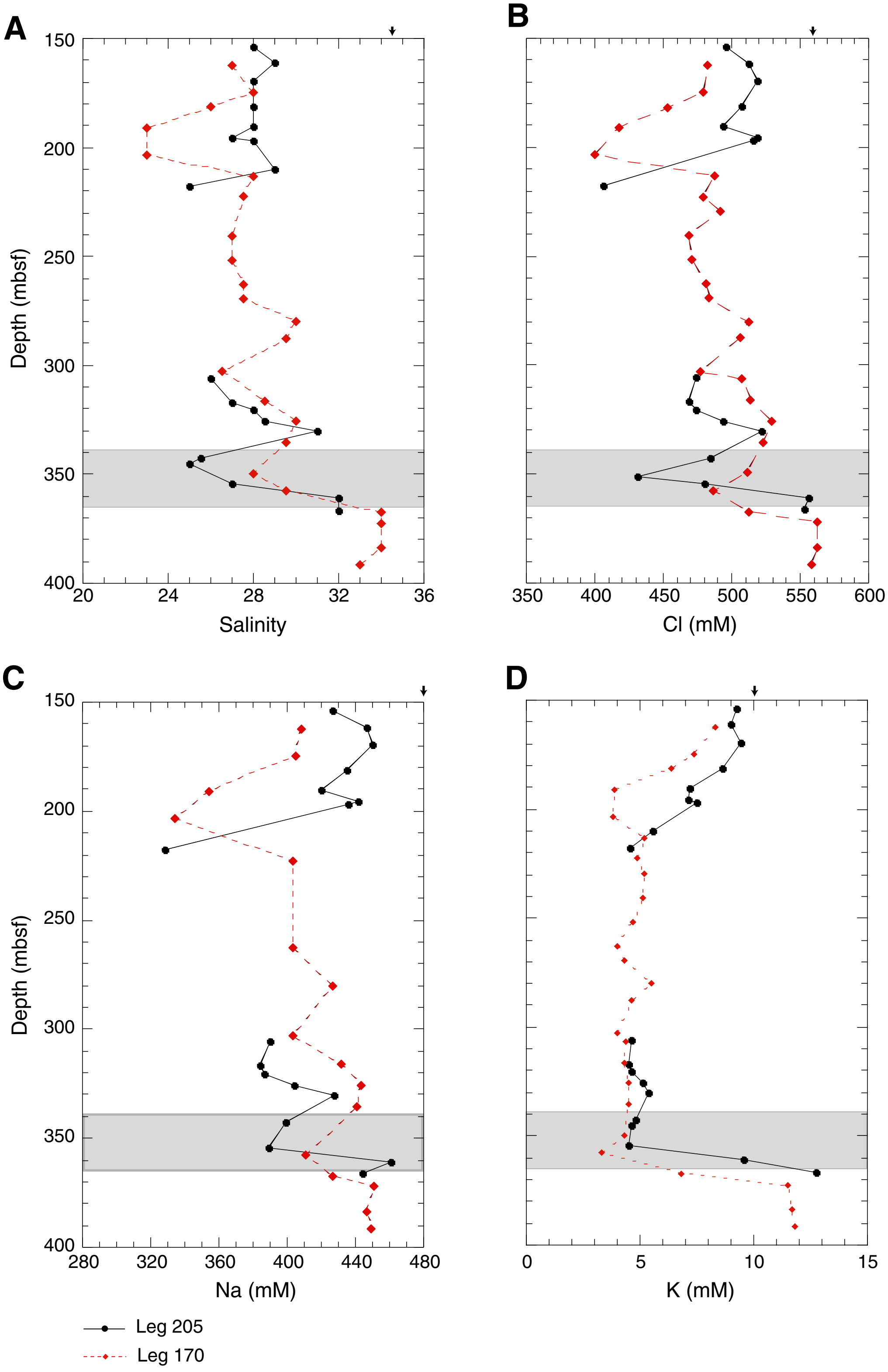

Figure F42. Depth profiles of (**A**) Ca, (**B**) Mg, (**C**) Mg/Ca, and (**D**) Sr. Arrows = seawater concentration. Shaded area =the décollement at Site 1254. Error bars are smaller than or comparable to symbol size (see **"Inorganic Geochemistry,"** p. 24, in the "Explanatory Notes" chapter). Leg 170 Sr data are provided by M. Kastner (pers. comm., 2002).

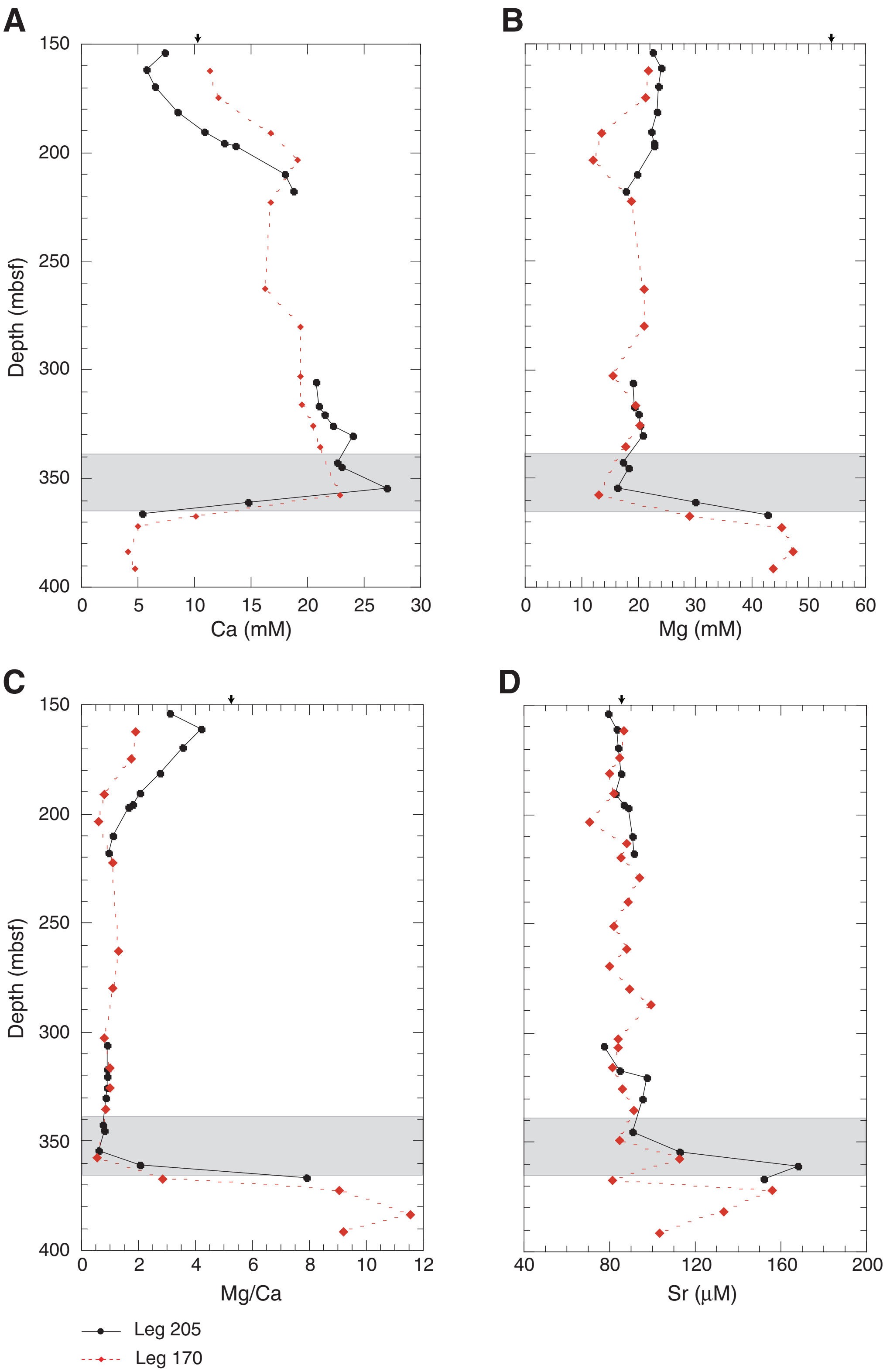

Figure F43. Depth profiles of (**A**) Ba, (**B**) Li, (**C**) Si, and (**D**) B. Arrows = seawater concentration. Shaded area = the décollement at Site 1254. Error bars are smaller than or comparable to symbol size (see **"Inorganic Geochemistry,"** p. 24, in the "Explanatory Notes" chapter). Leg 170 Li data are from Chan and Kastner (2000). Leg 170 B data are provided by M. Kastner (pers. comm., 2002).

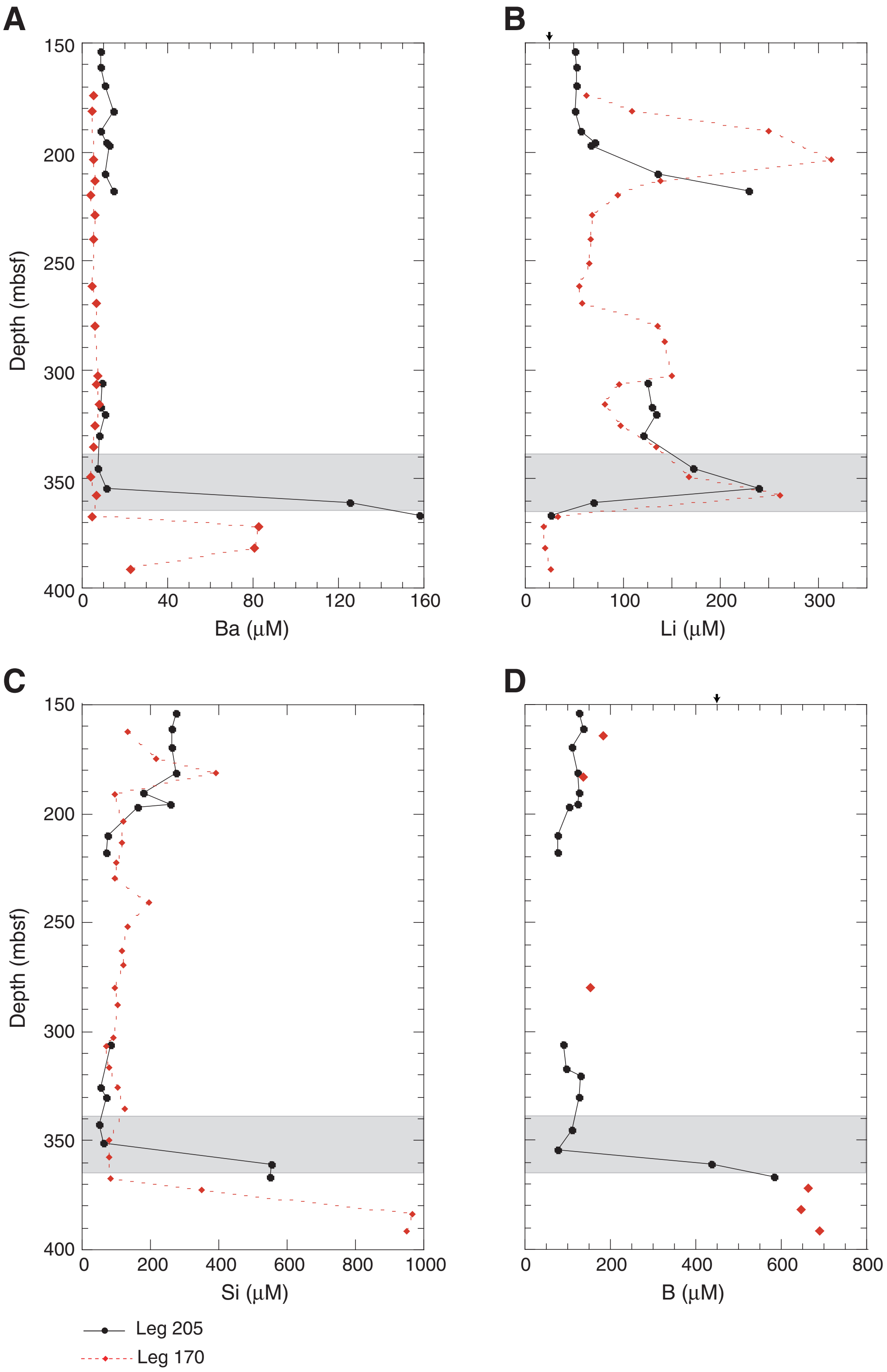

Figure F44. Depth profiles of (**A**) SO_4, (**B**) NH_4, (**C**) Fe, and (**D**) Mn. Arrows = seawater concentration. Shaded area = the décollement at Site 1254. Error bars are smaller than or comparable to symbol size (see "Inorganic Geochemistry," p. 24, in the "Explanatory Notes" chapter).

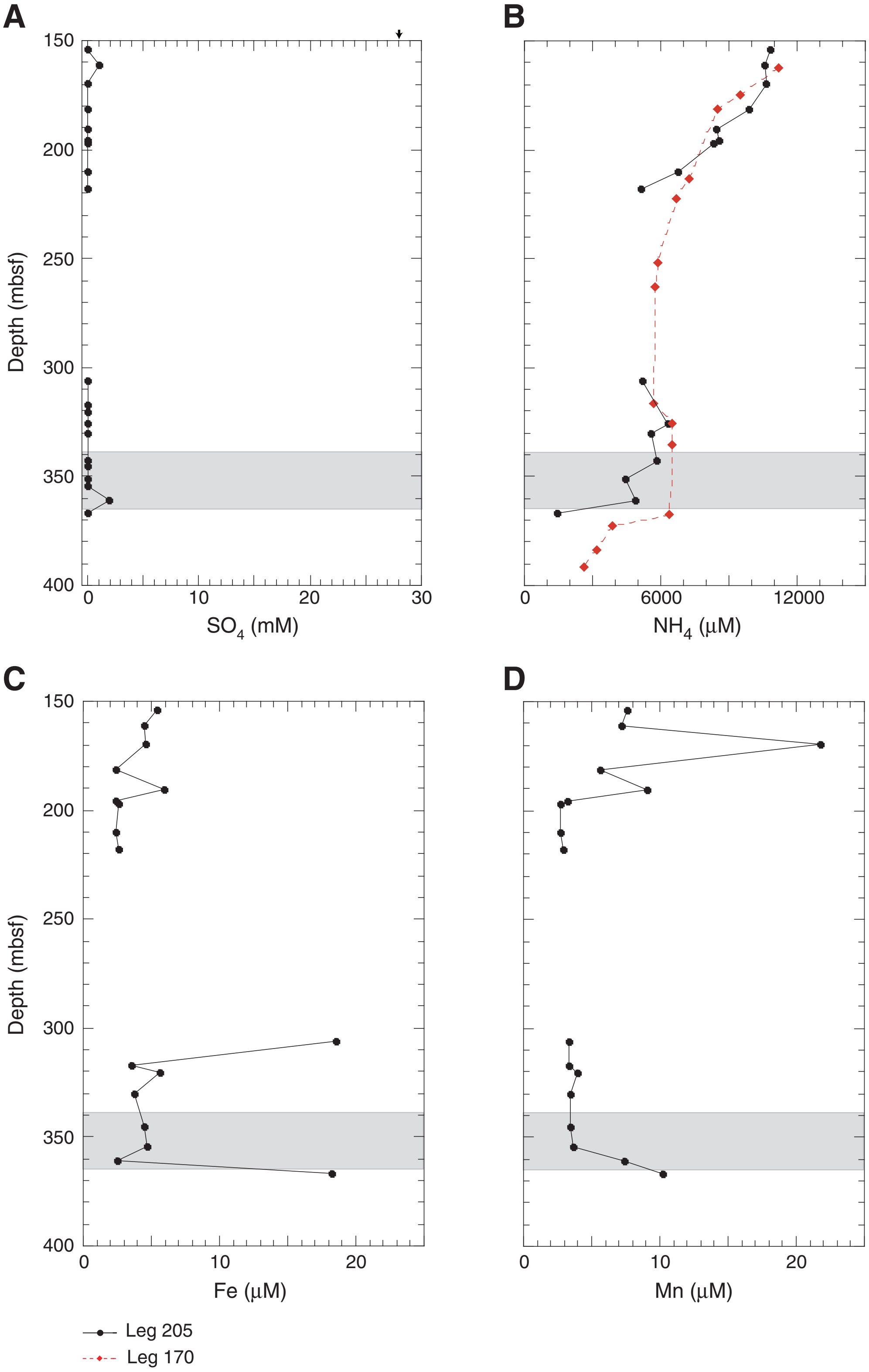

Figure F45. Results of vacutainer gas analyses for methane, ethane, and propane at Site 1254 (solid circles). The gray shaded areas = the upper fault zone and the décollement, respectively, as determined in **"Structural Geology,"** p. 20.

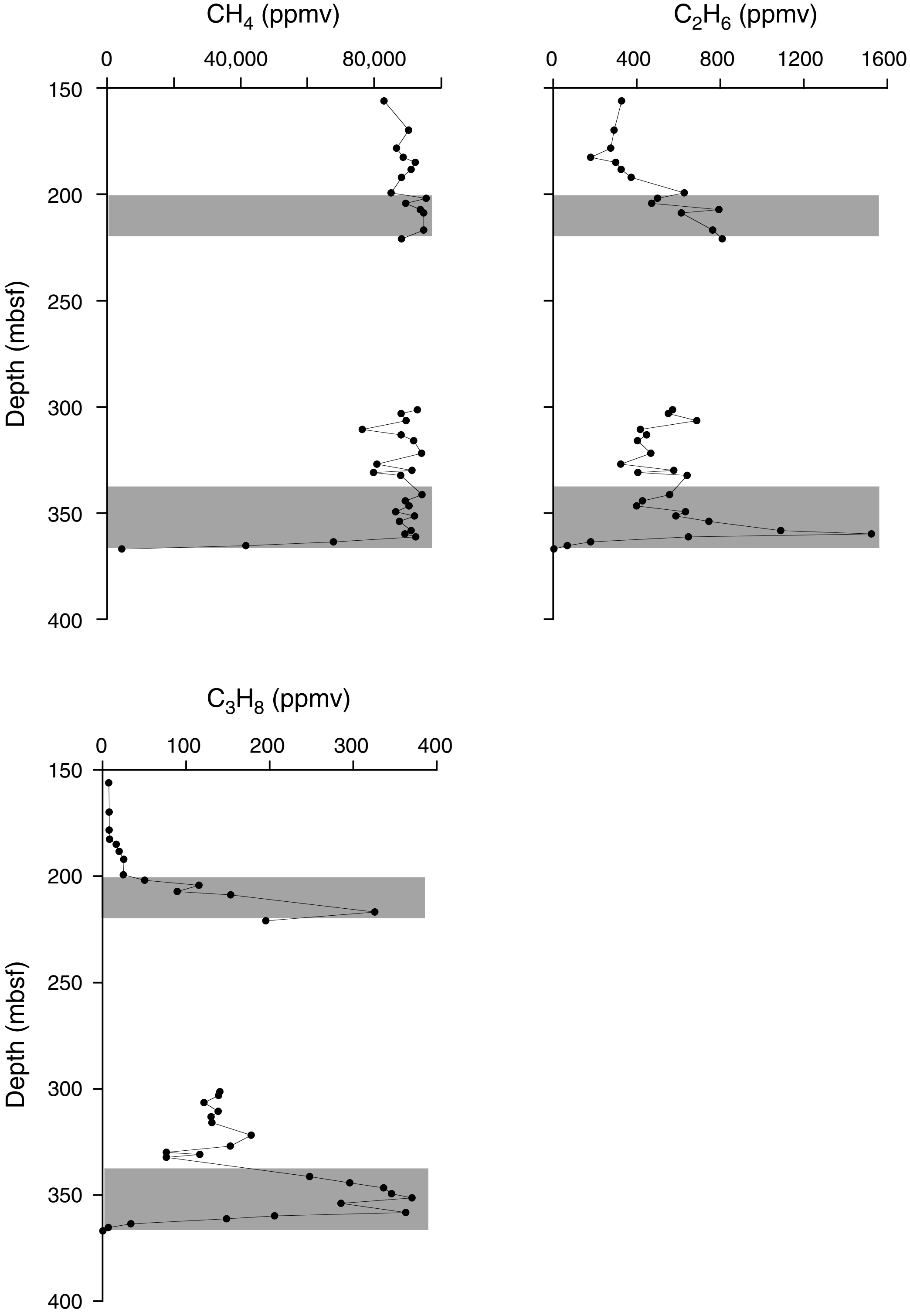

Figure F46. Results of headspace gas analyses for methane, ethane, and propane at Sites 1254 (solid circles) and 1040 (open circles). The gray shaded areas = the upper fault zone and the décollement, respectively, as determined in **"Structural Geology,"** p. 20.

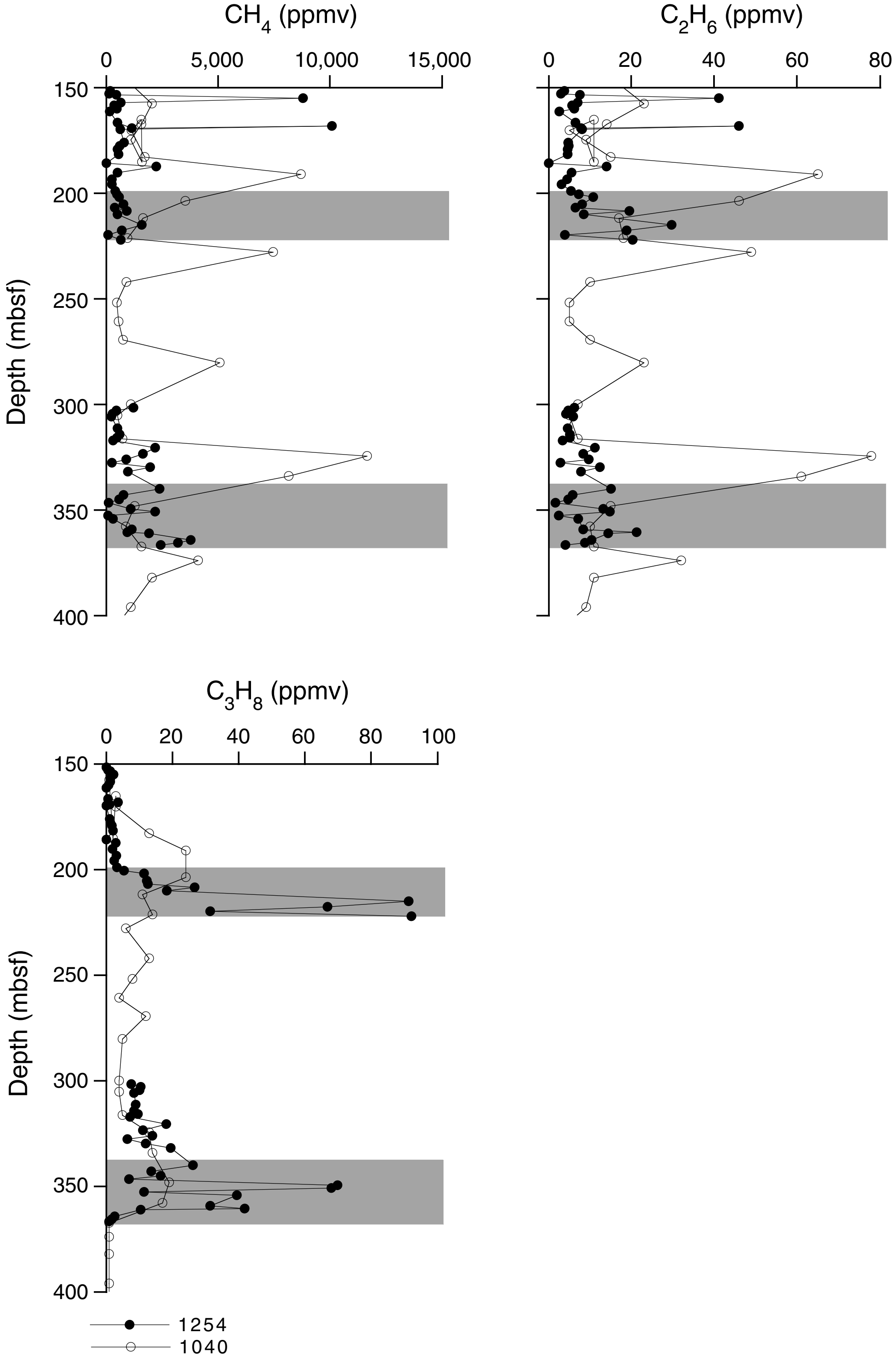

Figure F47. Depth profiles of (**A**) total organic carbon (TOC), (**B**) calcium carbonate, and (**C**) sulfur at Sites 1254 (solid circles) and 1040 (open circles). The gray shaded areas = the upper fault zone and the décollement, respectively, as determined in "**Structural Geology,**" p. 20.

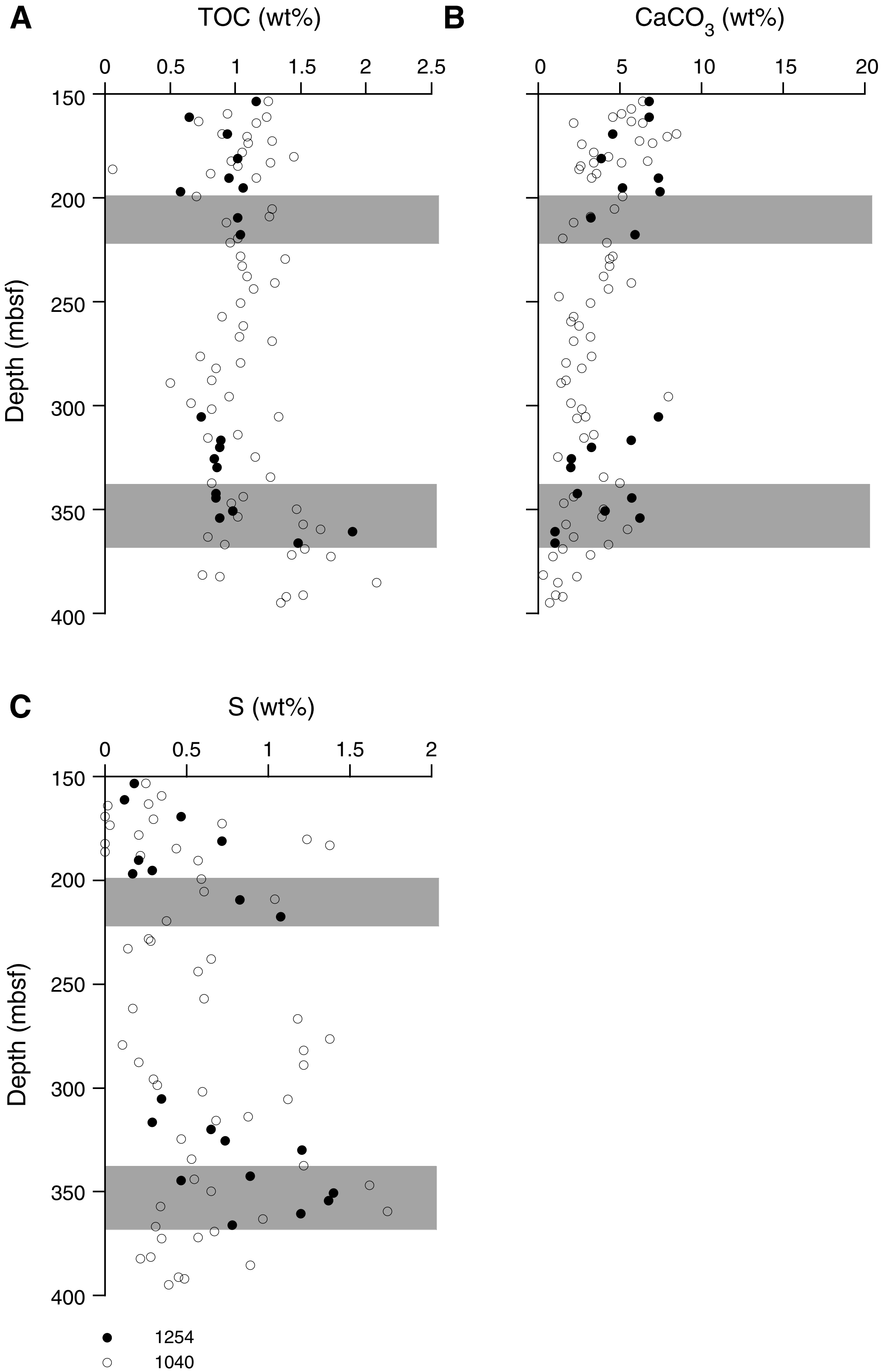

Figure F48. DVTPP deployment at 50 mbsf. **A.** DVTPP 01: complete temperature record. **B.** DVTPP 01: complete pressure record. **C.** DVTPP 01: enlargement of the temperature record around the penetration. **D.** DVTPP 01: enlargement of the pressure record at the same timescale as the temperature.

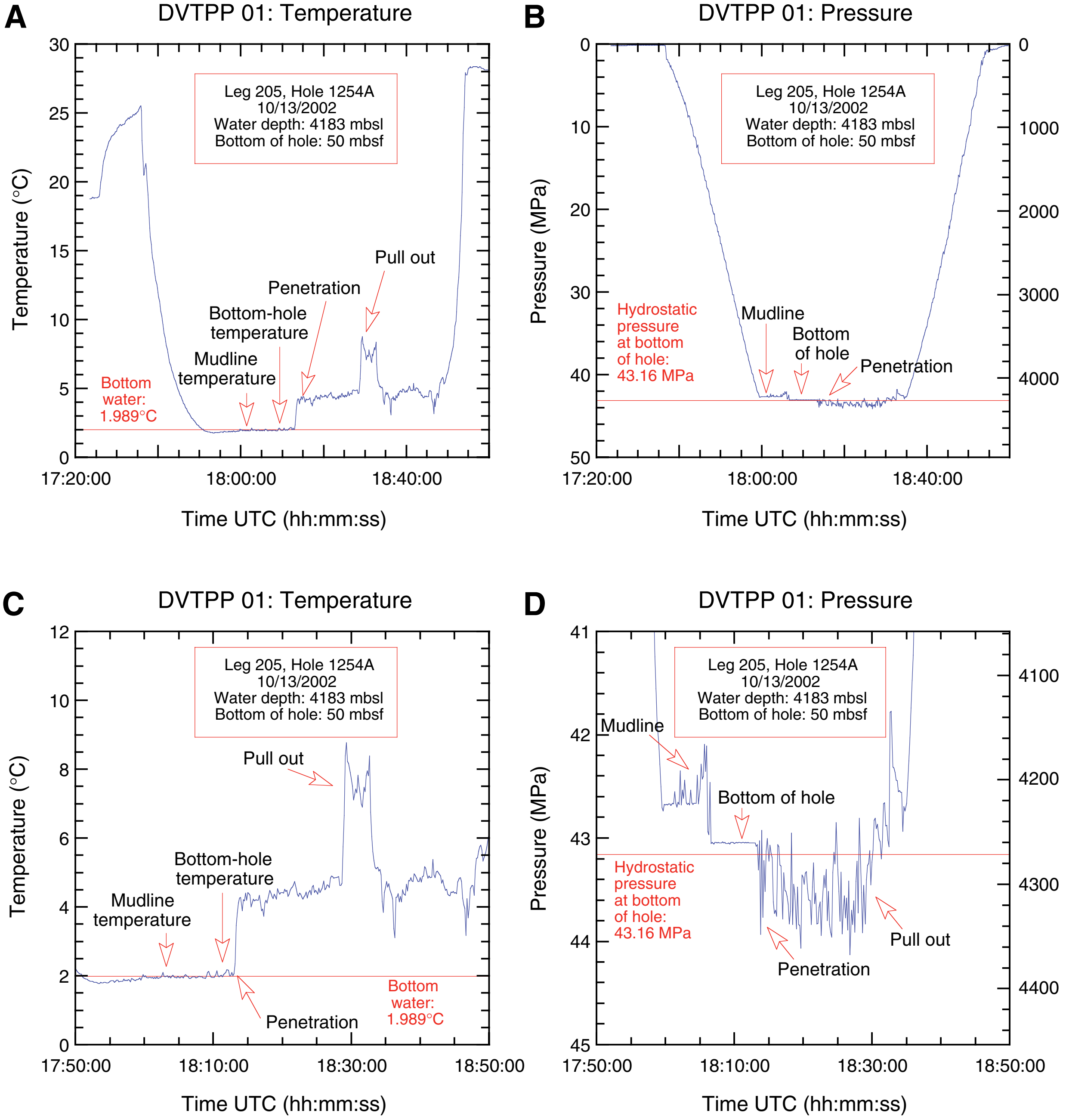

Figure F49. DVTP deployment at 150 mbsf. **A.** DVTP 02: complete temperature record. **B.** DVTP 02: enlargement of the temperature record around the penetration.

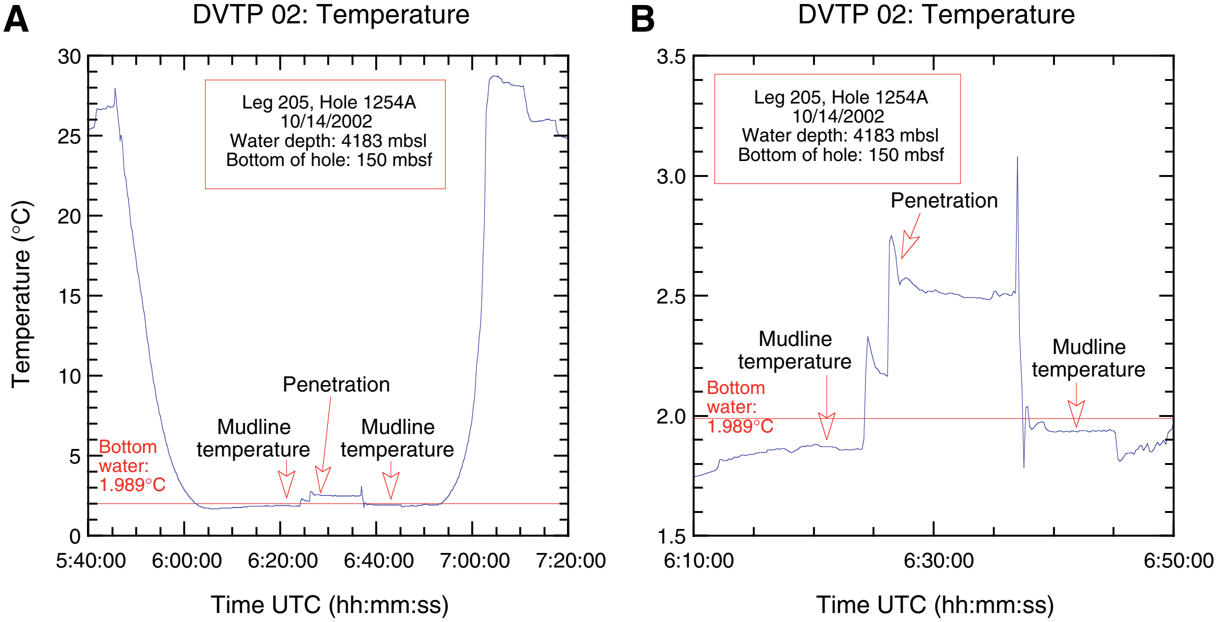

Figure F50. DVTPP deployment at 200 mbsf. **A.** DVTPP 06: complete temperature record. **B.** DVTPP 06: complete pressure record. **C.** DVTPP 06: enlargement of the temperature record around the penetration and the extrapolated sediment temperature. **D.** DVTPP 06: enlargement of the pressure record at the same timescale as the temperature.

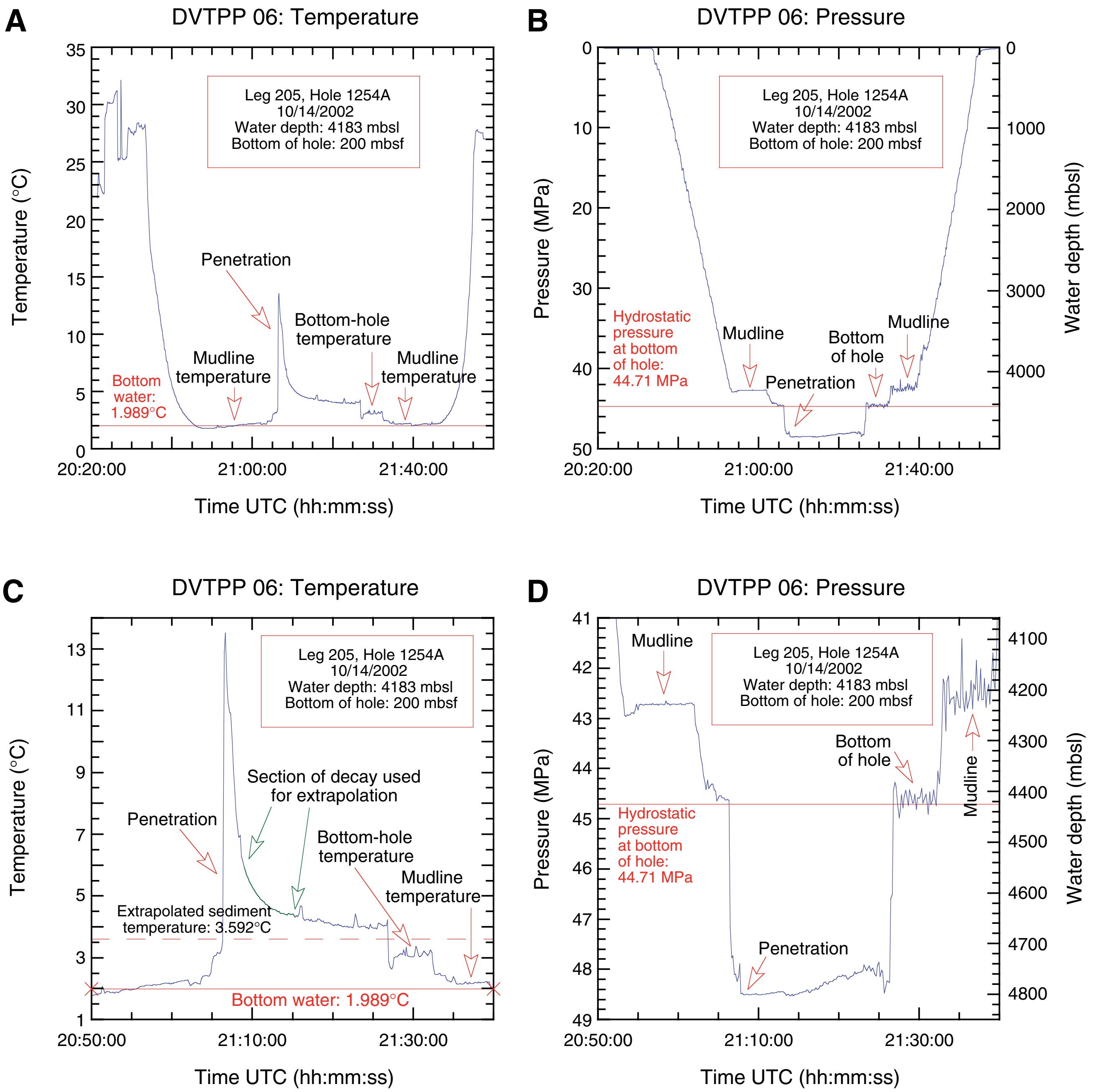

Table T1. Coring summary, Site 1254.

Hole 1254A

Latitude: 9°39.6989′N
Longitude: 86°10.7435′W
Time on site: 367.2 hr
Time on hole (hr): 191.58 (0945 hr, 11 Oct–0920 hr, 19 Oct 2002)
Seafloor (drill pipe measurement from rig floor, mbrf): 4194.0
Distance between rig floor and sea level (m): 11.20
Water depth (drill pipe measurement from sea level, m): 4182.8
Total depth (drill pipe measurement from rig floor, mbrf): 4561.5
Total penetration (meters below seafloor, mbsf): 367.5
Total length of cored section (m): 140.5
Total length of drilled intervals (m): 227.0
Total core recovered (m): 125.0
Core recovery (%): 89
Total number of cores: 16
Total number of drilled intervals: 3

Hole 1254B

Latitude: 9°39.7187′N
Longitude: 86°10.7274′W
Time on hole (hr): 7.31 (0920 hr, 19 Oct–1645 hr, 26 Oct 2002)
Seafloor (drill pipe measurement from rig floor, mbrf): 4187.0
Distance between rig floor and sea level (m): 11.4
Water depth (drill pipe measurement from sea level, m): 4175.6
Total depth (drill pipe measurement from rig floor, mbrf): 4465.0
Total penetration (meters below seafloor, mbsf): 278.0
Total length of drilled intervals (m): 278.0
Core recovery: NA
Remark: This hole was intended to emplace the downhole CORK-II/OsmoSampler. Only drilling/casing was done, and no core was taken in this hole.

Core	Date (Oct 2002)	Ship local time* (hr)	Depth (mbsf)		Length (m)		Recovery (%)	Remarks
			Top	Bottom	Cored	Recovered		
205-1254A-								
			*****Drilled from 0.0 to 50.0 mbsf*****					DVTPP at 50 mbsf; AHC
			*****Drilled from 50.0 to 150.0 mbsf*****					DVTP at 150 mbsf; AHC
1R	14	0415	150.0	155.5	5.5	5.99	108.9	Whirl-Pak
2R	14	0625	155.5	165.1	9.6	8.30	86.5	Whirl-Pak
3R	14	0825	165.1	174.7	9.6	6.71	69.9	Whirl-Pak
4R	14	1025	174.7	184.4	9.7	8.16	84.1	Whirl-Pak; AHC
5R	14	1250	184.4	194.1	9.7	9.76	100.6	Whirl-Pak; AHC
6R	14	1510	194.1	203.8	9.7	9.86	101.7	Whirl-Pak; AHC; DVTPP at 203.8 mbsf
7R	14	1930	203.8	213.4	9.6	8.41	87.6	Whirl-Pak; AHC
8R	14	2145	213.4	223.0	9.6	9.40	97.9	Whirl-Pak; AHC
			*****Drilled from 223.0 to 300.0 mbsf*****					
9R	15	1125	300.0	309.7	9.7	7.30	75.3	Whirl-Pak
10R	15	1355	309.7	319.3	9.6	9.98	104.0	Whirl-Pak
11R	15	1625	319.3	328.9	9.6	9.20	95.8	Whirl-Pak
12R	15	1900	328.9	338.5	9.6	4.40	45.8	Whirl-Pak
13R	15	2115	338.5	348.1	9.6	9.68	100.8	Whirl-Pak
14R	15	2310	348.1	357.7	9.6	8.01	83.4	Whirl-Pak
15R	16	0120	357.7	362.7	5.0	4.58	91.6	Whirl-Pak
16R	16	0320	362.7	367.5	4.8	5.26	109.6	Whirl-Pak
				Cored totals:	140.5	125.00	89.0	
				Drilled totals:	227.0			
				Total:	367.5			

Notes: * = Ship local time is Universal TIme Coordinated – 5 hr. DVTPP = Davis-Villinger Temperature-Pressure Probe, DVTP = Davis-Villinger Temperature Probe. Whirl-Pak = microbiology microsphere contamination testing. AHC = active heave compensation. NA = not applicable.

Table T2. Location of the major tephra layers identified, Site 1254.

Core, section, interval (cm)	Depth to top of layer (mbsf)
205-1254A-	
2R-1, 61–74	156.11
2R-1, 80–87	156.30
2R-2, 105–108	158.05
3R-3, 78–84	168.88
3R-4, 106–109	170.81
5R-3, 31–35	187.71
5R-3, 40–43	187.80
5R-3, 136–140	188.76
5R-5, 26–31	189.16
5R-6, 123–128	192.08
5R-6, 133–139	192.18
5R-6, 142–145	192.27
5R-7, 65–66	193.00
7R-5, 27–28	209.48
7R-6, 53–55	210.53
8R-1, 80–85	214.20
9R-1, 138–145	301.38
14R-2, 25–30	349.85

Table T3. Bulk geochemical analysis of sediments and tephra, Hole 1254A.

Core, section, interval (cm)	Depth (mbsf)	Major element oxide (wt%)										Ti/Al	Total
		SiO_2	TiO_2	Al_2O_3	Fe_2O_3	MnO	CaO	MgO	Na_2O	K_2O	P_2O_5		
Tephra:													
205-1254A-													
8R-8, 22–65	222.37	65.65	0.41	13.42	5.12	0.11	1.30	0.66	3.01	2.37	0.08	0.03	92.15
Sediments:													
205-1254A-													
1R-3, 52–87	153.52	55.49	1.03	16.20	8.69	0.07	4.13	3.16	2.72	2.24	0.21	0.06	93.93
3R-3, 125–165	169.35	54.49	1.04	17.80	9.46	0.09	3.07	3.03	2.56	2.00	0.15	0.06	93.69
4R-5, 45–90	181.11	55.61	1.07	17.73	8.43	0.07	3.53	2.89	2.67	2.23	0.12	0.06	94.35
5R-5, 50–90	190.40	50.72	0.90	15.51	9.13	0.07	3.45	3.14	2.34	1.90	0.22	0.06	87.39
6R-2, 125–166	196.97	53.43	1.07	17.05	8.59	0.06	3.42	3.00	2.50	2.16	0.12	0.06	91.40
7R-5, 34–74	209.55	54.77	0.92	17.39	8.06	0.05	2.69	2.75	2.29	1.95	0.13	0.05	91.00
8R-4, 0–45	217.65	53.23	0.91	16.98	8.36	0.06	3.11	2.87	2.27	1.84	0.15	0.05	89.78
9R-5, 0–40	305.50	54.41	0.95	17.17	9.13	0.09	3.75	2.96	2.42	2.16	0.20	0.06	93.22
10R-6, 0–40	316.73	51.66	0.95	16.04	8.28	0.07	3.18	2.87	2.28	1.84	0.16	0.06	87.33
11R-5, 63–103	325.67	55.62	1.06	17.26	9.54	0.05	2.97	3.54	2.62	2.12	0.11	0.06	94.88
12R-1, 101–141	329.91	52.94	1.06	17.04	8.39	0.05	2.96	2.80	2.49	1.99	0.10	0.06	89.83
13R-3, 100–145	342.50	56.75	0.88	17.69	8.42	0.04	3.03	3.05	2.52	2.25	0.11	0.05	94.74
14R-6, 52–97	354.28	51.62	0.86	17.48	8.36	0.10	2.95	2.72	2.23	1.86	0.12	0.05	88.30
15R-3, 0–44	360.65	50.72	0.83	15.33	8.41	0.09	3.22	2.71	2.54	1.74	0.13	0.05	85.71
16R-3, 49–89	366.19	50.29	0.79	14.97	7.36	0.07	3.04	2.72	2.61	1.89	0.11	0.05	83.84

Table T3 (continued).

Core, section, interval (cm)	Depth (mbsf)	Trace element (ppm)								
		Ba	Cr	Sr	V	Y	Zr	Sc	Mo	Cu
Tephra:										
205-1254A-										
8R-8, 22–65	222.37	1303	8.35	239	44.1	27.6	162.1	12.37	556	
Sediments:										
205-1254A-										
1R-3, 52–87	153.52	427.93	86.1	294	166	20.7	98.2			79.7
3R-3, 125–165	169.35	371.71	75.4	207	171	21.2	110.9			80.0
4R-5, 45–90	181.11	442.84	84.2	260	165	21.4	109.5			81.4
5R-5, 50–90	190.40	323.08	75.5	216	171	20.0	93.4			77.8
6R-2, 125–166	196.97	430.48	86.4	230	176	19.3	98.6			81.1
7R-5, 34–74	209.55	305.46	57.8	174	161	19.3	103.1			78.1
8R-4, 0–45	217.65	340.34	58.3	185	153	19.5	98.8			77.1
9R-5, 0–40	305.50	354.39	69.2	224	171	23.4	105.8			78.7
10R-6, 0–40	316.73	336.28	76.4	206	156	19.3	93.9			77.5
11R-5, 63–103	325.67	324.35	106.0	208	184	21.9	103.8			81.3
12R-1, 101–141	329.91	291.23	73.9	205	167	19.3	105.9			80.1
13R-3, 100–145	342.50	344.29	93.1	223	176	18.6	101.8			82.3
14R-6, 52–97	354.28	324.62	35.2	207	147	19.0	92.2			76.7
15R-3, 0–44	360.65	803.88	93.2	187	162	19.9	101.1			75.5
16R-3, 49–89	366.19	1811.51	69.1	208	156	17.7	95.9			74.1

Table T4. Peak intensities and peak areas from X-ray diffraction analysis of bulk-powder sediment samples, Leg 170, Holes 1040A, 1040B, and 1040C. (See table notes. Continued on next page.)

			X-ray diffraction peak intensities (cps)						X-ray diffraction peak areas (total count)					
Hole, core, section, interval (cm)	Subunit	Depth (mbsf)	Composite clay	Quartz (101)	Plagioclase (002)	Calcite (104)	Quartz (100)	Cristobalite (101)	Composite clay	Quartz (101)	Plagioclase (002)	Calcite (104)	Quartz (100)	Cristobalite (101)
170-														
1040B-1H-1, 140	P1A	1.40	102	440	192	57	93	49	3,872	5,552	2,007	783	1,312	627
1040A-1H-2, 140	P1A	2.90	109	548	105	15	99	80	3,526	6,829	870	95	1,395	966
1040B-1H-3, 135	P1A	4.35	69	305	971	58	60	71	2,746	4,600	9,315	804	1,046	885
1040B-1H-5, 140	P1A	6.66	107	509	179	73	123	54	3,555	6,553	2,067	859	1,823	624
1040B-2H-2, 135	P1A	8.35	101	456	266	172	121	57	3,563	5,778	3,077	2,294	1,652	643
1040B-2H-5, 135	P1A	12.85	133	375	248	255	89	39	3,603	4,945	2,387	3,166	1,466	449
1040B-4X-1, 110	P1A	19.10	100	461	153	33	76	74	3,557	6,045	1,771	363	992	919
1040B-5X-1, 135	P1A	28.35	135	162	481	119	48	97	5,021	1,939	5,047	1,910	639	1,396
1040B-6X-1, 130	P1A	37.70	132	182	172	93	50	69	4,817	2,554	1,537	1,325	628	953
1040B-8X-1, 74	P1A	55.94	112	568	180	31	101	64	4,194	7,072	2,188	240	1,514	791
1040B-9X-4, 124	P1A	70.26	130	451	184	37	103	53	4,449	6,232	2,488	483	1,844	881
1040B-10X-1, 130	P1B	75.70	118	528	171	45	114	87	4,052	6,375	2,248	702	1,574	991
1040B-11X-4, 130	P1B	89.80	102	501	197	26	105	64	3,415	6,380	2,313	241	16,28	737
1040B-12X-3, 125	P1B	97.85	103	532	168	45	107	60	3,690	6,611	2,169	547	1,551	875
1040B-13X-4, 33	P1B	103.93	86	433	148	139	86	60	3,176	5,528	1,607	1,958	1,164	956
1040B-14X-2, 120	P1B	106.50	103	464	216	106	94	42	3,282	6,059	2,820	1,509	1,674	606
1040B-15X-4, 125	P1B	119.05	112	520	246	48	136	59	3,874	6,686	2,434	637	1,853	773
1040B-16X-5, 125	P1B	128.45	103	497	136	141	107	1,563	3,491	6,007	1,644	1,702	49	634
1040B-18X-2, 120	P1B	144.90	94	489	198	123	96	55	3,448	6,523	2,208	1,550	1,574	818
1040B-19X-4, 120	P1B	157.35	99	466	94	35	86	57	3,534	6,933	1,966	723	1,364	802
1040C-1R-2, 120	P1B	162.00	92	456	110	57	91	60	3,216	6,042	1,272	823	1,544	870
1040B-20X-2, 120	P1B	164.10	101	495	140	168	93	59	3,607	6,044	1,461	2,036	1,283	739
1040C-2R-4, 115	P1B	174.45	88	488	113	57	88	58	3,385	6,029	1,421	713	1,248	757
1040B-21X-3, 120	P1B	174.57	105	513	125	55	93	61	2,999	6,795	1,252	795	1,224	868
1040C-3R-2, 115	P1B	181.05	91	406	174	90	108	36	3,521	5,143	1,858	1,628	1,407	361
1040B-22X-2, 120	P1B	183.30	119	593	188	43	116	79	3,975	7,625	2,493	527	1,558	1,025
1040C-4R-2, 120	P1B	190.70	129	214	67	0	79	63	4,226	2,607	876	0	949	758
1040C-5R-1, 105	P1B	198.65	124	186	80	9	69	43	4,059	3,181	984	78	933	517
1040C-5R-3, 34	P1B	200.94	147	190	127	17	66	52	4,895	2,533	1,793	247	904	594
1040C-5R-4, 115	P1B	203.25	133	218	165	20	74	56	4,319	2,713	2,120	181	988	675
1040C-5R-5, 102	P1B	204.62	134	222	120	0	77	57	4,026	2,854	1,723	0	1,120	687
1040C-6R-4, 16	P1B	211.96	37	130	50	13	30	17	1,213	1,594	691	152	441	149
1040C-6R-4, 120	P1B	213.00	103	470	218	50	101	80	3,766	5,978	2,874	634	1,412	939
1040C-6R-5, 81	P1B	214.11	101	529	144	36	95	45	3,472	6,465	1,728	471	1,498	554
1040C-7R-4, 15	P1B	221.55	53	254	75	41	79	41	2,084	3,316	853	489	1,012	402
1040C-8R-2, 115	P1B	229.15	101	466	126	66	111	64	3,584	6,085	1,449	865	1,533	964
1040C-9R-3, 115	P1B	240.31	95	524	309	77	95	65	3,078	6,394	3,442	1,051	1,510	790
1040C-10R-4, 115	P1B	251.45	92	398	110	97	83	39	3,212	5,156	1,278	1,245	1,140	446
1040C-11R-5, 115	P1B	261.86	104	468	151	40	109	40	3,679	6,136	1,917	466	1,671	465
1040C-12R-3, 115	P1B	269.25	100	523	136	43	118	34	3,561	6,345	1,581	501	1,516	332
1040C-14R-3, 0	P1B	287.40	93	456	176	79	104	42	3,290	5,839	1,820	1,468	1,410	488
1040C-16R-2, 120	P1B	306.40	95	435	126	95	104	63	3,321	5,608	1,535	1,261	1,383	684
1040C-17R-2, 115	P1B	315.95	86	488	162	131	92	40	3,091	5,956	2,163	1,713	1,304	452
1040C-18R-2, 115	P1B	325.65	75	448	868	43	121	64	2,930	5,568	8,167	483	1,501	942
1040C-19R-2, 115	P1B	335.25	86	509	381	29	115	34	3,171	6,310	4,423	255	1,475	300
1040C-20R-5, 115	P1B	349.35	94	551	169	43	107	45	3,495	6,939	2,098	501	1,454	652

Table T4 (continued).

Hole, core, section, interval (cm)	Subunit	Depth (mbsf)	X-ray diffraction peak intensities (cps)						X-ray diffraction peak areas (total count)					
			Composite clay	Quartz (101)	Plagioclase (002)	Calcite (104)	Quartz (100)	Cristobalite (101)	Composite clay	Quartz (101)	Plagioclase (002)	Calcite (104)	Quartz (100)	Cristobalite (101)
1040C-21R-4, 115	P1B	357.45	97	428	220	21	104	132	3,290	5,423	2,499	200	1,467	1,344
1040C-22R-4, 115	P1B	367.05	83	490	167	80	94	46	2,701	6,123	1,849	1,023	1,224	646
1040C-23R-1, 115	U1A	372.15	74	265	147	23	59	74	2,967	3,458	1,461	298	786	998
1040C-24R-2, 120	U1A	383.30	84	398	136	28	67	89	2,846	4,699	1,554	329	995	1,109
1040C-25R-1, 125	U1B	391.45	85	307	174	43	62	62	3,510	3,768	1,732	451	763	834
1040C-26R-1, 125	U1B	401.05	79	323	108	23	75	74	3,417	3,999	1,144	258	967	992
1040C-27R-3, 125	U1B	413.65	63	215	188	144	42	51	2,255	2,833	1,842	1,833	488	667
1040C-28R-2, 125	U1B	421.85	73	298	103	68	62	66	2,613	3,960	1,127	919	889	828
1040C-29R-2, 118	U2A	431.28	77	303	85	70	73	61	3,136	3,837	965	889	894	753
1040C-30R-2, 125	U2A	440.95	99	325	125	0	66	72	3,435	4,089	1,543	0	867	937
1040C-31R-3, 125	U2A	452.05	81	360	100	61	73	61	3,241	5,020	1,236	734	1,061	840
1040C-32R-3, 125	U2A	461.65	86	331	100	65	64	64	3,261	4,153	1,222	750	869	824
1040C-33R-5, 120	U2B	474.20	89	225	103	31	58	55	3,851	3,003	1,094	326	673	756
1040C-34R-3, 125	U3A	480.95	64	74	89	1,259	22	37	2,487	1,372	1,109	15,285	188	514
1040C-35R-3, 132	U3A	490.69	37	53	57	488	36	48	1,447	606	711	6,301	410	614
1040C-36R-3, 135	U3B	500.35	0	0	0	3,541	0	0	0	0	0	42,005	0	0
1040C-37R-4, 135	U3B	511.32	12	0	0	3,329	0	0	412	0	0	41,029	0	0
1040C-38R-3, 130	U3B	519.60	9	0	0	3,635	0	0	203	0	0	43,365	0	0
1040C-39R-4, 115	U3B	530.55	0	12	0	3,536	0	0	0	131	0	42,954	0	0
1040C-40R-4, 130	U3B	540.30	13	0	6	3,408	0	0	339	0	48	40,794	0	0
1040C-41R-5, 130	U3B	551.40	0	11	0	3,464	0	0	0	92	0	41,603	0	0
1040C-42R-5, 130	U3B	560.80	10	0	0	2,786	0	0	356	0	0	34,290	0	0
1040C-43R-1, 130	U3B	564.70	0	23	0	1,854	0	0	0	232	0	23,322	0	0
1040C-44R-3, 126	U3C	577.36	13	0	0	2,280	0	0	471	0	0	28,207	0	0
1040C-45R-2, 130	U3C	585.50	0	18	0	3,197	0	0	0	187	0	38,356	0	0
1040C-46R-2, 130	U3C	595.10	10	0	5	3,336	0	0	254	0	34	40,166	0	0
1040C-48R-6, 130	U3C	620.40	13	14	7	2,940	0	0	385	101	42	36,316	0	0
1040C-49R-3, 94	U3C	625.14	93	12	18	128	18	0	3,865	106	257	1,837	190	0
1040C-50R-3, 130	U3C	634.90	14	0	7	2,380	0	0	578	0	59	29,610	0	0
1040C-51R-3, 120	U3C	644.60	21	1,035	43	2,474	212	412	675	11,766	540	29,924	2,624	5,319
1040C-52R-2, 125	U3C	652.75	30	2,091	137	1,507	419	95	560	24,442	1,686	18,452	4,705	1,223

Notes: cps = count per second. Numbers in parentheses are Miller indexes.

Table T5. Peak area ratios for dominant minerals, Leg 170, Holes 1040A, 1040B, and 1040C. (**See table notes.** Continued on next page.)

Hole, core, section, interval (cm)	Subunit	Depth (mbsf)	Peak areas relative to quartz (101)			Peak area ratio
			Clay/ Quartz	Plagioclase/ Quartz	Calcite/ Quartz	Cristobalite (101)/ Quartz (100)
170-						
1040B-1H-1, 140	P1A	1.40	0.70	0.36	0.14	0.48
1040A-1H-2, 140	P1A	2.90	0.52	0.13	0.01	0.69
1040B-1H-3, 135	P1A	4.35	0.60	2.03	0.17	0.85
1040B-1H-5, 140	P1A	6.66	0.54	0.32	0.13	0.34
1040B-2H-2, 135	P1A	8.35	0.62	0.53	0.40	0.39
1040B-2H-5, 135	P1A	12.85	0.73	0.48	0.64	0.31
1040B-4X-1, 110	P1A	19.10	0.59	0.29	0.06	0.93
1040B-5X-1, 135	P1A	28.35	2.59	2.60	0.99	2.18
1040B-6X-1, 130	P1A	37.70	1.89	0.60	0.52	1.52
1040B-8X-1, 74	P1A	55.94	0.59	0.31	0.03	0.52
1040B-9X-4, 124	P1A	70.26	0.71	0.40	0.08	0.48
1040B-10X-1, 130	P1B	75.70	0.64	0.35	0.11	0.63
1040B-11X-4, 130	P1B	89.80	0.54	0.36	0.04	0.45
1040B-12X-3, 125	P1B	97.85	0.56	0.33	0.08	0.56
1040B-13X-4, 33	P1B	103.93	0.57	0.29	0.35	0.82
1040B-14X-2, 120	P1B	106.50	0.54	0.47	0.25	0.36
1040B-15X-4, 125	P1B	119.05	0.58	0.36	0.10	0.42
1040B-16X-5, 125	P1B	128.45	0.58	0.27	0.28	12.94
1040B-18X-2, 120	P1B	144.90	0.53	0.34	0.24	0.52
1040B-19X-4, 120	P1B	157.35	0.51	0.28	0.10	0.59
1040C-1R-2, 120	P1B	162.00	0.53	0.21	0.14	0.56
1040B-20X-2, 120	P1B	164.10	0.60	0.24	0.34	0.58
1040C-2R-4, 115	P1B	174.45	0.56	0.24	0.12	0.61
1040B-21X-3, 120	P1B	174.57	0.44	0.18	0.12	0.71
1040C-3R-2, 115	P1B	181.05	0.68	0.36	0.32	0.26
1040B-22X-2, 120	P1B	183.30	0.52	0.33	0.07	0.66
1040C-4R-2, 120	P1B	190.70	1.62	0.34	0.00	0.80
1040C-5R-1, 105	P1B	198.65	1.28	0.31	0.02	0.55
1040C-5R-3, 34	P1B	200.94	1.93	0.71	0.10	0.66
1040C-5R-4, 115	P1B	203.25	1.59	0.78	0.07	0.68
1040C-5R-5, 102	P1B	204.62	1.41	0.60	0.00	0.61
1040C-6R-4, 16	P1B	211.96	0.76	0.43	0.10	0.34
1040C-6R-4, 120	P1B	213.00	0.63	0.48	0.11	0.67
1040C-6R-5, 81	P1B	214.11	0.54	0.27	0.07	0.37
1040C-7R-4, 15	P1B	221.55	0.63	0.26	0.15	0.40
1040C-8R-2, 115	P1B	229.15	0.59	0.24	0.14	0.63
1040C-9R-3, 115	P1B	240.31	0.48	0.54	0.16	0.52
1040C-10R-4, 115	P1B	251.45	0.62	0.25	0.24	0.39
1040C-11R-5, 115	P1B	261.86	0.60	0.31	0.08	0.28
1040C-12R-3, 115	P1B	269.25	0.56	0.25	0.08	0.22
1040C-14R-3, 0	P1B	287.40	0.56	0.31	0.25	0.35
1040C-16R-2, 120	P1B	306.40	0.59	0.27	0.22	0.49
1040C-17R-2, 115	P1B	315.95	0.52	0.36	0.29	0.35
1040C-18R-2, 115	P1B	325.65	0.53	1.47	0.09	0.63
1040C-19R-2, 115	P1B	335.25	0.50	0.70	0.04	0.20
1040C-20R-5, 115	P1B	349.35	0.50	0.30	0.07	0.45
1040C-21R-4, 115	P1B	357.45	0.61	0.46	0.04	0.92
1040C-22R-4, 115	P1B	367.05	0.44	0.30	0.17	0.53
1040C-23R-1, 115	U1A	372.15	0.86	0.42	0.09	1.27
1040C-24R-2, 120	U1A	383.30	0.61	0.33	0.07	1.11
1040C-25R-1, 125	U1B	391.45	0.93	0.46	0.12	1.09
1040C-26R-1, 125	U1B	401.05	0.85	0.29	0.06	1.03
1040C-27R-3, 125	U1B	413.65	0.80	0.65	0.65	1.37
1040C-28R-2, 125	U1B	421.85	0.66	0.28	0.23	0.93
1040C-29R-2, 118	U2A	431.28	0.82	0.25	0.23	0.84
1040C-30R-2, 125	U2A	440.95	0.84	0.38	0.00	1.08
1040C-31R-3, 125	U2A	452.05	0.65	0.25	0.15	0.79
1040C-32R-3, 125	U2A	461.65	0.79	0.29	0.18	0.95
1040C-33R-5, 120	U2B	474.20	1.28	0.36	0.11	1.12
1040C-34R-3, 125	U3A	480.95	1.81	0.81	11.14	2.73
1040C-35R-3, 132	U3A	490.69	2.39	1.17	10.40	1.50
1040C-36R-3, 135	U3B	500.35	NA	NA	NA	
1040C-37R-4, 135	U3B	511.32	NA	NA	NA	
1040C-38R-3, 130	U3B	519.60	NA	NA	NA	

Table T5 (continued).

			Peak areas relative to quartz (101)			Peak area ratio
Hole, core, section, interval (cm)	Subunit	Depth (mbsf)	Clay/ Quartz	Plagioclase/ Quartz	Calcite/ Quartz	Cristobalite (101)/ Quartz (100)
1040C-39R-4, 115	U3B	530.55	0.00	0.00	327.89	
1040C-40R-4, 130	U3B	540.30	NA	NA	NA	
1040C-41R-5, 130	U3B	551.40	0.00	0.00	452.21	
1040C-42R-5, 130	U3B	560.80	NA	NA	NA	
1040C-43R-1, 130	U3B	564.70	0.00	0.00	100.53	
1040C-44R-3, 126	U3C	577.36	NA	NA	NA	
1040C-45R-2, 130	U3C	585.50	0.00	0.00	205.11	
1040C-46R-2, 130	U3C	595.10	NA	NA	NA	
1040C-48R-6, 130	U3C	620.40	3.81	0.42	359.56	
1040C-49R-3, 94	U3C	625.14	36.46	2.42	17.33	
1040C-50R-3, 130	U3C	634.90	NA	NA	NA	
1040C-51R-3, 120	U3C	644.60	0.06	0.05	2.54	2.03
1040C-52R-2, 125	U3C	652.75	0.02	0.07	0.75	0.26

Notes: NA = peak was not resolvable on diffractogram. Numbers in parentheses are Miller indexes.

Table T6. Peak intensities and peak areas from X-ray diffraction analysis of bulk-powder sediment samples, Leg 205, Hole 1254A. (See table notes. Continued on next page.)

			X-ray diffraction peak intensities (cps)						X-ray diffraction peak areas (total count)					
Core, section, interval (cm)	Subunit	Depth (mbsf)	Composite clay	Quartz (101)	Plagioclase (002)	Calcite (104)	Quartz (100)	Cristobalite (101)	Composite clay	Quartz (101)	Plagioclase (002)	Calcite (104)	Quartz (100)	Cristobalite (101)
205-1254A-														
1R-3, 46–47	P1B	153.46	128	530	116	64	118	71	4631	7186	1916	847	1807	960
1R-3, 52–87	P1B	153.52	109	524	276	120	121	57	4002	7113	3147	1617	1621	977
2R-4, 125–160	P1B	161.25	121	627	292	50	103	96	4471	8605	3141	726	1452	1359
3R-3, 114–116	P1B	169.24	142	534	183	43	99	275	4639	7497	2395	596	1482	2819
3R-3, 125–165	P1B	169.35	136	511	161	32	194	78	4613	7273	2257	393	2606	1098
4R-5, 45–90	P1B	181.11	132	618	188	63	127	74	4655	8353	2534	974	1711	936
5R-1, 25–27	P1B	184.65	125	516	150	58	167	70	4329	7242	2099	694	2202	1049
5R-2, 113–115	P1B	187.03	97	697	321	88	137	77	3302	9452	3763	1213	1942	1127
5R-5, 50–90	P1B	190.40	128	521	177	79	100	62	4529	6945	2100	1085	1550	871
5R-7, 90–91	P1B	193.25	120	652	345	65	144	78	3795	8432	4753	801	2105	1281
6R-1, 65–67	P1B	194.75	115	535	217	57	107	61	4197	7163	2453	771	1654	927
6R-1, 121–162	P1B	195.31	125	559	160	21	101	59	4145	7578	2070	174	1604	742
6R-2, 125–166	P1B	196.97	127	671	240	61	126	63	4664	8750	3009	807	1964	923
6R-3, 65–67	P1B	198.08	135	570	231	30	115	54	4839	7693	2746	426	1758	708
7R-2, 26–28	P1B	205.56	128	475	229	51	110	53	4675	6419	2862	731	1656	606
7R-5, 34–74	P1B	209.55	177	447	149	24	125	49	6094	6312	1950	278	1970	552
7R-6, 33–35	P1B	210.33	167	457	105	20	119	37	5774	6487	1314	231	1882	409
8R-4, 0–45	P1B	217.65	187	319	114	57	85	48	6429	4263	1706	679	1311	581
8R-5, 22–23	P1B	218.37	179	363	166	248	102	32	5846	5098	2103	3837	1896	255
8R-6, 28–29	P1B	219.93	178	369	321	152	97	46	6381	5275	3395	2158	1521	468
9R-2, 86–88	P1B	302.36	137	517	174	43	131	46	4871	7019	2302	488	2001	578
9R-5, 0–40	P1B	305.50	148	460	184	73	129	49	4838	6427	2262	909	1829	602
10R-2, 50–52	P1B	311.70	151	494	180	41	146	51	5042	7346	2321	572	2272	669
10R-6, 0–40	P1B	316.73	134	513	228	36	108	40	4726	7136	2610	411	1598	517
11R-1, 78–117	P1B	320.08	117	636	216	43	144	166	4259	8772	2867	481	2179	1599
11R-2, 80–82	P1B	321.33	128	537	299	73	124	48	5051	7773	3579	954	1881	491
11R-5, 50–51	P1B	325.54	120	528	242	42	116	54	4365	7372	3079	532	1831	633
11R-5, 63–103	P1B	325.67	125	512	170	31	105	57	5026	7178	2307	279	1687	772
11R-7, 55–57	P1B	328.17	138	579	251	155	125	64	4933	7809	2742	2285	1888	785
12R-1, 101–141	P1B	329.91	140	555	276	43	129	38	4925	7535	3376	348	1912	470
12R-3, 17–18	P1B	332.05	127	585	208	27	117	60	4619	7958	2550	412	1807	697
13R-3, 100–145	P1B	342.50	165	585	202	27	127	30	5647	8947	2723	256	2311	388
13R-5, 65–109	P1B	344.69	138	494	204	150	111	61	4648	6914	2887	2149	1900	775
14R-3, 0–40	P1B	350.81	192	294	97	18	98	22	6650	4276	1537	130	1594	243
14R-4, 32–33	P1B	351.58	182	360	95	53	111	24	6500	3751	1546	827	1756	277
14R-4, 114–116	P1B	352.40	200	311	96	15	106	43	7088	4684	1444	99	1599	493
14R-6, 52–97	P1B	354.28	185	322	150	21	102	38	6252	4334	2003	218	1797	386
14R-7, 84–85	P1B	355.62	133	433	173	121	124	24	4695	6283	1737	1626	2034	258
15R-1, 30–31	P1B	358.00	148	346	122	63	103	25	5615	5378	1399	957	1653	294
15R-1, 65–66	P1B	358.35	133	543	194	39	208	30	4485	7256	2109	537	2867	402
15R-1, 75–76	P1B	358.45	155	400	146	32	118	33	5290	5797	1757	449	1960	356
15R-2, 40–41	P1B	359.60	150	395	235	58	113	31	4908	5493	2577	820	1729	307
15R-2, 100–101	P1B	360.20	110	519	286	89	143	265	3623	7255	3377	1034	2248	2456
15R-2, 130–131	P1B	360.50	140	381	202	106	122	57	4625	5406	2354	1054	1883	585
15R-3, 0–44	P1B	360.65	110	389	166	41	74	76	4025	5077	2057	509	1223	1122
15R-4, 20–21	P1B	361.35	69	218	174	26	42	72	2576	2910	2256	262	658	1001

Table T6 (continued).

Core, section, interval (cm)	Subunit	Depth (mbsf)	X-ray diffraction peak intensities (cps)						X-ray diffraction peak areas (total count)					
			Composite clay	Quartz (101)	Plagioclase (002)	Calcite (104)	Quartz (100)	Cristobalite (101)	Composite clay	Quartz (101)	Plagioclase (002)	Calcite (104)	Quartz (100)	Cristobalite (101)
15R-4, 80–81	P1B	361.95	107	336	245	56	80	81	4132	4483	2697	642	1213	1060
16R-1, 70–71	P1B	363.40	125	341	98	58	80	79	4506	4967	1234	724	1283	1174
16R-2, 30–31	P1B	364.50	101	303	140	30	72	79	3948	4119	1765	578	1117	1140
16R-3, 20–21	P1B	365.90	130	377	149	19	82	88	4825	5219	1629	246	1242	1205
16R-3, 49–89	P1B	366.19	114	330	162	42	76	86	4304	4704	2108	479	1210	1312
16R-4, 60–61	P1B	367.24	90	320	185	31	66	92	3344	4297	2266	257	981	1407

Notes: cps = count per second. Numbers in parentheses are Miller indexes.

Table T7. Peak area ratios for dominant minerals, Leg 205, Hole 1254A.

			Peak areas relative to quartz (101)			Peak area ratio
Core, section, interval (cm)	Subunit	Depth (mbsf)	Clay/ Quartz	Plagioclase/ Quartz	Calcite/ Quartz	Cristobalite (101)/ Quartz (100)
205-1254A-						
1R-3, 46–47	P1B	153.46	0.64	0.27	0.12	0.53
1R-3, 52–87	P1B	153.52	0.56	0.44	0.23	0.60
2R-4, 125–160	P1B	161.25	0.52	0.37	0.08	0.94
3R-3, 114–116	P1B	169.24	0.62	0.32	0.08	1.90
3R-3, 125–165	P1B	169.35	0.63	0.31	0.05	0.42
4R-5, 45–90	P1B	181.11	0.56	0.30	0.12	0.55
5R-1, 25–27	P1B	184.65	0.60	0.29	0.10	0.48
5R-2, 113–115	P1B	187.03	0.35	0.40	0.13	0.58
5R-5, 50–90	P1B	190.40	0.65	0.30	0.16	0.56
5R-7, 90–91	P1B	193.25	0.45	0.56	0.09	0.61
6R-1, 65–67	P1B	194.75	0.59	0.34	0.11	0.56
6R-1, 121–162	P1B	195.31	0.55	0.27	0.02	0.46
6R-2, 125–166	P1B	196.97	0.53	0.34	0.09	0.47
6R-3, 65–67	P1B	198.08	0.63	0.36	0.06	0.40
7R-2, 26–28	P1B	205.56	0.73	0.45	0.11	0.37
7R-5, 34–74	P1B	209.55	0.97	0.31	0.04	0.28
7R-6, 33–35	P1B	210.33	0.89	0.20	0.04	0.22
8R-4, 0–45	P1B	217.65	1.51	0.40	0.16	0.44
8R-5, 22–23	P1B	218.37	1.15	0.41	0.75	0.13
8R-6, 28–29	P1B	219.93	1.21	0.64	0.41	0.31
9R-2, 86–88	P1B	302.36	0.69	0.33	0.07	0.29
9R-5, 0–40	P1B	305.50	0.75	0.35	0.14	0.33
10R-2, 50–52	P1B	311.70	0.69	0.32	0.08	0.29
10R-6, 0–40	P1B	316.73	0.66	0.37	0.06	0.32
11R-1, 78–117	P1B	320.08	0.49	0.33	0.05	0.73
11R-2, 80–82	P1B	321.33	0.65	0.46	0.12	0.26
11R-5, 50–51	P1B	325.54	0.59	0.42	0.07	0.35
11R-5, 63–103	P1B	325.67	0.70	0.32	0.04	0.46
11R-7, 55–57	P1B	328.17	0.63	0.35	0.29	0.42
12R-1, 101–141	P1B	329.91	0.65	0.45	0.05	0.25
12R-3, 17–18	P1B	332.05	0.58	0.32	0.05	0.39
13R-3, 100–145	P1B	342.50	0.63	0.30	0.03	0.17
13R-5, 65–109	P1B	344.69	0.67	0.42	0.31	0.41
14R-3, 0–40	P1B	350.81	1.56	0.36	0.03	0.15
14R-4, 32–33	P1B	351.58	1.73	0.41	0.22	0.16
14R-4, 114–116	P1B	352.40	1.51	0.31	0.02	0.31
14R-6, 52–97	P1B	354.28	1.44	0.46	0.05	0.21
14R-7, 84–85	P1B	355.62	0.75	0.28	0.26	0.13
15R-1, 30–31	P1B	358.00	1.04	0.26	0.18	0.18
15R-1, 65–66	P1B	358.35	0.62	0.29	0.07	0.14
15R-1, 75–76	P1B	358.45	0.91	0.30	0.08	0.18
15R-2, 40–41	P1B	359.60	0.89	0.47	0.15	0.18
15R-2, 100–101	P1B	360.20	0.50	0.47	0.14	1.09
15R-2, 130–131	P1B	360.50	0.86	0.44	0.19	0.31
15R-3, 0–44	P1B	360.65	0.79	0.41	0.10	0.92
15R-4, 20–21	P1B	361.65	0.89	0.78	0.09	1.52
15R-4, 80–81	P1B	361.95	0.92	0.60	0.14	0.87
16R-1, 70–71	P1B	363.40	0.91	0.25	0.15	0.92
16R-2, 30–31	P1B	364.50	0.96	0.43	0.14	1.02
16R-3, 20–21	P1B	365.90	0.92	0.31	0.05	0.97
16R-3, 49–89	P1B	366.19	0.91	0.45	0.10	1.08
16R-4, 60–61	P1B	367.24	0.78	0.53	0.06	1.43

Notes: NA = peak was not resolvable in diffractogram. Numbers in parentheses are Miller indexes.

Table T8. Peak intensities and peak areas from X-ray diffraction analysis of glycolated oriented aggregate clay slides from sediment samples, Hole 1254A.

Core, section, interval (cm)	Depth (mbsf)	Peak intensity (cps)			Peak area (total count)		
		Smectite	Illite	Kaolinite/ Chlorite	Smectite	Illite	Kaolinite/ Chlorite
205-1254A-							
3R-3, 114–116	169.24	836	0	173	51,506	0	4,639
9R-2, 86–88	302.36	1,263	0	232	63,979	0	4,842
10R-2, 50–52	311.70	1,127	24	159	52,654	255	4,225
12R-1, 101–141	329.91	812	0	183	49,373	0	4,691
14R-3, 0–40	350.81	2,972	55	146	126,146	637	3,390
15R-1, 30–31	358.00	1,673	0	175	95,875	0	4,249
15R-1, 65–66	358.35	1,350	0	151	61,734	0	3,637
15R-1, 75–76	358.45	1,467	31	138	67,107	508	3,417
15R-2, 40–41	359.60	1,001	0	140	46,736	0	3,223
15R-2, 100–101	360.20	1,229	24	170	56,933	361	3,884
15R-2, 130–131	360.50	1,660	28	233	85,517	391	5,005
15R-3, 0–44	360.65	656	22	177	45,961	237	5,997
15R-4, 20–21	361.35	818	0	126	42,299	0	3,877
15R-4, 80–81	361.95	707	20	90	34,289	376	3,564
16R-1, 70–71	363.40	719	20	137	38,535	233	4,796
16R-2, 30–31	364.50	817	23	142	41,093	490	5,183
16R-3, 20–21	365.90	759	19	128	38,382	135	4,203
16R-3, 49–89	366.19	680	22	131	41,533	193	4,394
16R-4, 60–61	367.24	863	32	127	41,703	438	4,000

Note: cps = count per second.

Table T9. Calculated relative abundances based on X-ray diffraction analysis of oriented aggregate clay slides, Hole 1254A.

Core, section, interval (cm)	Depth (mbsf)	Relative abundance Smectite (wt%)	Illite (wt%)	Kaolinite/ Chlorite
205-1254A-				
3R-3, 114–116	169.24	84.74	0.00	15.26
9R-2, 86–88	302.36	86.85	0.00	13.15
10R-2, 50–52	311.70	84.76	1.64	13.60
12R-1, 101–141	329.91	84.03	0.00	15.97
14R-3, 0–40	350.81	93.11	1.88	5.00
15R-1, 30–31	358.00	91.86	0.00	8.14
15R-1, 65–66	358.35	89.46	0.00	10.54
15R-1, 75–76	358.45	88.33	2.67	9.00
15R-2, 40–41	359.60	87.88	0.00	12.12
15R-2, 100–101	360.20	86.07	2.18	11.74
15R-2, 130–131	360.50	88.08	1.61	10.31
15R-3, 0–44	360.65	78.03	1.61	20.36
15R-4, 20–21	361.35	84.51	0.00	15.49
15R-4, 80–81	361.95	79.89	3.50	16.61
16R-1, 70–71	363.40	78.55	1.90	19.55
16R-2, 30–31	364.50	76.93	3.67	19.41
16R-3, 20–21	365.90	81.10	1.14	17.76
16R-3, 49–89	366.19	81.29	1.51	17.20
16R-4, 60–61	367.24	81.05	3.40	15.55

Note: Peak areas were weighted (smectite by 1, illite by 4, kaolinite/chlorite by 2) and normalized to 100%, as described in Biscaye (1965).

Table T10. Summary of structural data, Site 1254. (See table notes. Continued on next two pages.)

						Measured orientation in core											
Core, section, interval (cm)	Interval (cm)	Half	Depth (mbsf)	Structural features	Thickness (cm)	First azimuth (°)	First dip (°)	Second azimuth (°)	Second dip (°)	Third azimuth (°)	Third dip (°)	Declination (°)	Corrected azimuth (°)	Lineation	Slip	Sense	Confidence
205-1254A-																	
1R-4, 27–37		A	154.14	Bedding	1	90	45	0	11	251	57	357.17	253.83				H
2R-1, 60–73	60–73	A	156.10	Stratigraphic disruption	4												H
2R-2, 73–80		A	157.73	Fault		270	56	180	27	251	57	5.82	245.18				H
2R-2, 73–88		A	157.73	Fracture		90	87	NM	NM								H
2R-2, 110–114		A	158.10	Fracture		270	53	180	28	248	55	237.35	10.65				H
2R-2, 110–114		A	158.10	Fracture		270	51	0	46	310	58	237.35	72.65				H
2R-3, 124–129		A	159.74	Fracture		270	38	180	50	213	55	8.6	204.40				H
2R-5, 144–149		A	163.04	Fault		90	36	180	14	109	38	326.34	142.66				H
3R-4, 108–108	108–110	A	170.83	Fault		90	78	NM	NM							R	H
3R-4, 108–110		A	170.83	Bedding						0	0		0.00				H
4R-1, 21–23		A	174.91	Fissility		270	18	0	19	317	25	254.25	62.75				H
4R-1, 21–23		A	174.91	Foliation		270	48	0	10	279	48	254.25	24.75				H
4R-1, 89–91	86–95	A	175.59	Fissility		270	19	0	11	299	22	179.78	119.22				H
4R-1, 89–91		A	175.59	Fracture		90	20	0	28	34	33	179.68	214.32				H
4R-3, 11–12		A	177.77	Fissility		270	16	0	41	342	42	257.23	84.77				H
4R-3, 11–12	6–12	A	177.77	Foliation		90	48	180	28	116	51	257.23	218.77				H
4R-3, 99–100		A	178.65	Fissility		270	8	180	12	213	14	59.82	153.18				H
4R-3, 99–100		A	178.65	Foliation		270	39	180	22	243	42	59.82	183.18				H
4R-3, 103–104	103–108	A	178.69	Foliation		90	24	0	26	42	33	213.98	188.02				H
4R-4, 98–104		A	180.14	Stratigraphic disruption													H
4R-5, 36–40		A	181.02	Fracture		270	34	180	51	290	55	278.6	11.40				H
4R-5, 36–40		A	181.02	Fracture		270	34	180	51	290	55	278.6	11.40				H
4R-5, 36–40		A	181.02	Fracture		270	34	180	51	290	55	278.6	11.40				H
4R-5, 40–		A	181.06	Fissility		90	34	0	23	128	51	281.35	206.65				H
5R-1, 36–42		A	184.76	Fissility		90	39	180	16	109	41	94.49	14.51				H
5R-1, 84–89		W	185.24	Fissility		270	34	180	13	251	35	1.44	249.56				H
5R-5, 30–34		W	190.20	Fissility		90	52	180	50	102	53	330.12	131.88				H
6R-1, 19–31		A	194.29	Fracture		90	56	0	9	84	56	257.66	186.34				H
6R-1, 23–33		A	194.33	Fissility		270	52	180	15	258	53	257.66	0.34				H
6R-1, 49–55		A	194.59	Fracture		270	37	0	36	314	46	95.57	218.43		DS	R	H
6R-3, 39–44		A	197.82	Foliation		90	17	0	11	58	20	287.93	130.07				H
6R-3, 64–71		A	198.07	Foliation		270	11	180	14	218	18	242.35	335.65				H
6R-3, 66–78		A	198.09	Fracture		270	58	180	15	260	58	246.55	13.45				H
6R-4, 94–99		A	199.87	Foliation		90	16	180	14	131	21	40.27	90.73				H
6R-5, 110–120		W	201.53	Fissility		90	49	180	2	91	41	230.04	220.96				H
6R-6, 50–57		W	202.43	Bedding		270	38	0	37	308	45	287.93	20.07				H
7R-5, 11–12		A	209.32	Fissility		90	5	0	5	45	7	267.29	137.71				H
7R-5, 11–12		A	209.32	Foliation		90	31	0	13	69	33	267.29	161.71				H
8R-3, 10–20		A	216.50	Foliation		270	53	180	14	259	53	320.79	298.21				H
8R-8, 26–31		A	222.41	Bedding		270	29	180	10	252	30	4.7	247.30				H
9R-3, 52–55		A	303.52	Fracture		270	26	0	2	271	26	189.38	81.62				H
11R-4, 100–121		A	324.53	Fracture		270	19	0	4	271	49	280.62	350.38				H
11R-4, 104–110		A	324.57	Fracture		90	41	0	26	151	45	322.07	188.93				H
11R-4, 126–131		A	324.79	Fracture		90	77	0	9	178	13	20.32	157.68				H
11R-6, 30–33		A	326.42	Fissility		90	12	180	10	130	15	306.97	183.03				H
11R-6, 30–33		A	326.42	Foliation		90	24	0	41	27	44	306.97	80.03				H

Table T10 (continued).

						Measured orientation in core											
Core, section, interval (cm)	Interval (cm)	Half	Depth (mbsf)	Structural features	Thickness (cm)	First azimuth (°)	First dip (°)	Second azimuth (°)	Second dip (°)	Third azimuth (°)	Third dip (°)	Declination (°)	Corrected azimuth (°)	Lineation	Slip	Sense	Confidence
12R-1, 56–58		A	329.46	Bedding		270	28	0	21	306	33	276.93	29.07				H
12R-1, 77–83		A	329.68	Bedding		270	37	0	51	331	57	283.72	47.28				H
12R-3, 83–88		A	332.71	Bedding		270	61	0	22	283	62	256.58	26.42				H
13R-2, 64–76		A	340.64	Fracture		270	61	0	15	275	61	329.3	305.70				H
13R-2, 64–76		A	340.64	Fracture		270	61	0	15	275	61	329.3	305.70				H
13R-2, 64–76		A	340.64	Fracture		270	61	0	15	275	61	329.3	305.70				H
13R-2, 64–76		A	340.64	Fracture		270	61	0	15	275	61	329.3	305.70				H
13R-2, 64–76		A	340.64	Fracture		270	61	0	15	275	61	329.3	305.70				H
13R-2, 69–72		A	340.69	Fissility		90	20	0	11	62	22	329.3	92.70				H
13R-2, 69–72		A	340.69	Foliation		90	5	0	57	3	57	329.3	33.70				H
14R-7, 57–61		A	355.35	Bedding		270	36	0	4	248	36	17.45	230.55				H
14R-7, 62–66		A	355.40	Foliation		270	38	0	9	281	39	266.25	14.75				H
14R-7, 62–66		A	355.40	Fracture		270	71	0	2	217	71	266.25	310.75				H
14R-7, 62–66		A	355.40	Fracture		270	43	0	34	306	49	266.25	39.75				H
15R-4, 11–12		A	361.26	Foliation		270	5	180	53	184	53	21.19	162.81				H
15R-4, 44–49		A	361.59	Fissility		270	60	0	33	291	62	305.82	345.18				H
15R-4, 44–49		A	361.59	Foliation		270	12	0	18	327	21	304.82	22.18				H
15R-4, 54–57		A	361.69	Fissility		270	16	180	9	241	18	144.88	96.12				H
15R-4, 54–57		A	361.69	Fracture		90	61	180	1	90	61	144.88	305.12				H
15R-4, 54–57		A	361.69	Fracture		270	82	0	6	271	82	144.88	126.12				H
16R-1, 16–21		A	362.86	Foliation		270	28	0	31	322	41	278.81	43.19				H
16R-1, 27–61		A	362.97	Foliation		270	36	0	27	305	42	31.99	273.01				H
16R-1, 34–39		A	363.04	Fault		90	36	0	8	55	42	160.23	254.77				H
16R-1, 37–70		A	363.07	Foliation		90	44	180	36	127	50	179.02	307.98				H
16R-1, 57–64		A	363.27	Fault		270	47	0	18	287	48	179.02	107.98	120	DS	R	H
16R-1, 67–70		A	363.37	Fault		90	36	0	43	128	50	30.32	97.68		DS	R	H
16R-1, 91–107		A	363.61	Fault		270	56	0	20	284	57	254.11	29.89	28	DS	S	H
16R-1, 97–101		A	363.67	Fracture		270	26	0	26	335	35	265.14	69.86				H
16R-1, 119–122	115–122	A	363.89	Fault		270	4	180	49	183	49	351.83	191.17	31	DS	N	H
16R-1, 123–127	122–127	A	363.93	Fissility		90	33	0	8	78	34	54.18	23.82				H
16R-1, 123–127	122–127	A	363.93	Foliation		90	23	180	29	143	35	141.12	1.88				H
16R-1, 125–127	122–127	A	363.95	Fault		90	20	180	29	147	34	141.12	5.88	320	DS	R	H
16R-2, 19–23	19–23	A	364.38	Brittle shear zone bound	3	270	14	180	52	191	53	78.61	112.39				H
16R-2, 24–31	27–31	A	364.44	Brittle shear zone bound	7	90	8	180	10	141	13	79.4	61.60			S	H
16R-2, 38–40		A	364.58	Fissility		90	34	0	18	64	37	341.14	82.86				H
16R-2, 48–72		A	364.68	Fault		90	63	180	20	101	63	8.92	92.08	90	SS		H
16R-2, 54–62		W	364.74	Brittle shear zone bound	7	90	22	180	13	125	26	347.04	137.96				H
16R-2, 68–73		W	364.88	Brittle shear zone bound	7	270	14	180	30	203	32	94.71	108.29				H
16R-2, 69–73		W	364.89	Brittle shear zone bound	7	270	4	180	33	183	33	94.71	88.29				H
16R-2, 110–124		W	365.30	Brittle shear zone bound		270	10	0	47	351	47	234.73	116.27				H
16R-2, 110–124		W	365.30	Fracture		270	41	0	19	292	43	234.73	57.27				H
16R-2, 122–128		A	365.42	Fault		270	63	0	4	272	65	213.41	58.59			R	H
16R-2, 140–147		A	365.60	Fault		270	65	0	14	277	62	76.85	200.15				H
16R-2, 140–147		A	365.60	Fault		270	57	0	9	84	57	76.85	7.15				H
16R-2, 140–147		A	365.60	Fissility		90	7	0	17	22	18	126.32	255.68				H
16R-3, 2–3		A	365.72	Fissility		90	1	0	46	1	46	354.76	6.24				H
16R-3, 2–3		A	365.72	Fault		90	41	180	36	130	49	374.76	115.24			R	H

Table T10 (continued).

						Measured orientation in core											
Core, section, interval (cm)	Interval (cm)	Half	Depth (mbsf)	Structural features	Thickness (cm)	First azimuth (°)	First dip (°)	Second azimuth (°)	Second dip (°)	Third azimuth (°)	Third dip (°)	Declination (°)	Corrected azimuth (°)	Lineation	Slip	Sense	Confidence
16R-3, 3–7		W	365.73	Fracture		90	56	0	50	51	62	374.76	36.24				H
16R-3, 14–20		A	365.84	Fracture		90	47	180	7	97	47	113.27	343.73				H
16R-3, 14–20		A	365.84	Fault		270	4	NM	NM								H
16R-3, 15–20		A	365.85	Fissility		90	30	180	24	128	36	124.62	3.38				H
16R-3, 30–35	30–38	A	366.00	Brittle shear zone bound	6	270	35		5	277	35	257.98	19.02			S	H
16R-4, 37–67		A	367.01	Fissility		90	9	0	28	17	29	203.02	173.98				H
16R-4, 59–57		A	367.23	Fissility		90	34	0	62	20	63	162.66	217.34				H

Notes: A = archive half, W = working half. NM = not measurable. DS = dip slip, SS = strike slip. N = normal, R = reverse, S = sinistral, D = dextral. H = high confidence.

Table T11. Pore water chemical data of major constituents, Hole 1254A.

Core, section, interval (cm)	Depth (mbsf)	Volume (cm^3)	Salinity	Cl (mM)	SO_4 (mM)	Na* (mM)	Mg (mM)	K (mM)	Ca (mM)	Mg/Ca	Na/Cl
205-1254A-											
1R-3, 52–87	153.7	8.3	28.0	496	0.00	426.79	22.62	9.28	7.34	3.08	0.86
2R-4, 125–160	161.4	8.8	29.0	513	1.08	446.76	24.02	8.98	5.69	4.22	0.87
3R-3, 125–165	169.6	19.5	28.0	519	0.00	449.68	23.39	9.46	6.54	3.57	0.87
4R-5, 45–90	181.3	18.0	28.0	507	0.00	434.71	23.37	8.63	8.46	2.76	0.86
5R-5, 50–90	190.6	6.0	28.0	494	0.00	420.34	22.34	7.16	10.91	2.05	0.85
6R-1, 121–162	195.5	4.5	27.0	519	0.00	441.31	22.70	7.12	12.58	1.80	0.85
6R-2, 125–166	197.2	5.5	28.0	516	0.00	435.91	22.63	7.53	13.65	1.66	0.84
7R-5, 34–74	209.8	3.5	29.0		0.00	ND	19.69	5.58	18.06	1.09	ND
8R-4, 0–45	217.9	3.0	25.0	406	0.00	328.54	17.68	4.54	18.78	0.94	0.81
9R-5, 0–40	305.7	5.0	26.0	474	0.00	389.76	19.03	4.65	20.77	0.92	0.82
10R-6, 0–40	316.9	3.6	27.0	469	0.00	384.05	19.26	4.51	20.96	0.92	0.82
11R-1, 78–117	320.3	3.5	28.0	474	0.00	386.48	19.90	4.62	21.55	0.92	0.82
11R-5, 63–103	325.9	2.8	28.5	494	0.00	403.83	20.23	5.11	22.30	0.91	0.82
12R-1, 101–141	330.1	7.0	31.0	522	0.00	427.39	20.64	5.40	23.97	0.86	0.82
13R-3, 100–145	342.7	2.5	25.5	484	0.00	399.28	17.31	4.83	22.64	0.76	0.82
13R-5, 69–109	344.9	3.0	25.0		0.00	ND	18.18	4.65	23.01	0.79	ND
14R-3, 0–40	351.0	4.5		431	0.00	ND	ND	ND	ND	ND	ND
14R-6, 52–97	354.5	4.0	27.0	480	0.00	389.15	16.22	4.51	26.95	0.60	0.81
15R-3, 0–44	360.9	11.5	32.0	556	1.92	460.97	29.92	9.56	14.73	2.03	0.83
16R-3, 49–89	366.4	21.0	32.0	553	0.00	444.16	42.66	12.74	5.39	7.91	0.80

Notes: * = alkalinity not included in charge balance. ND = not determined.

Table T12. Pore water chemical data of minor constituents, Hole 1254A.

Core, section, interval (cm)	Depth (mbsf)	Volume (cm^3)	B (µM)	Ba (µM)	Fe (µM)	Li (µM)	Mn (µM)	Sr (µM)	Si (µM)	NH_4 (µM)
205-1254A-										
1R-3, 52–87	153.7	8.3	128.07	8.80	5.45	51.33	7.61	79.50	274.30	10,796.4
2R-4, 125–160	161.4	8.8	137.76	8.72	4.48	51.84	7.18	83.38	261.90	10,565.0
3R-3, 125–165	169.6	19.5	109.78	10.76	4.54	53.06	21.73	84.08	264.00	10,605.5
4R-5, 45–90	181.3	18.0	122.63	14.61	2.36	50.78	5.61	85.26	275.40	9,890.0
5R-5, 50–90	190.6	6.0	125.34	8.55	5.92	57.36	9.08	82.70	177.50	8,442.2
6R-1, 121–162	195.5	4.5	123.90	11.54	2.37	71.88	3.27	86.93	257.80	8,556.7
6R-2, 125–166	197.2	5.5	104.23	12.72	2.61	66.94	2.73	88.43	163.00	8,327.7
7R-5, 34–74	209.8	3.5	77.36	10.77	2.39	135.69	2.68	90.77	74.50	6,724.2
8R-4, 0–45	217.9	3.0	78.27	14.82	2.62	229.14	2.92	91.40	71.40	5,127.5
9R-5, 0–40	305.7	5.0	91.53	9.63	18.51	125.10	3.36	77.11	83.40	5,165.0
10R-6, 0–40	316.9	3.6	97.76	8.74	3.52	129.99	3.29	84.82	ND	ND
11R-1, 78–117	320.3	3.5	130.88	10.37	5.65	133.82	3.97	97.28	ND	ND
11R-5, 63–103	325.9	2.8	ND	ND	ND	ND	ND	ND	55.40	6,302.5
12R-1, 101–141	330.1	7.0	125.35	7.95	3.80	121.67	3.47	95.20	71.40	5,540.0
13R-3, 100–145	342.7	2.5	ND	ND	ND	ND	ND	ND	51.40	5,827.5
13R-5, 69–109	344.9	3.0	109.30	7.31	4.52	171.47	3.46	90.95	ND	ND
14R-3, 0–40	351.0	4.5	ND	ND	ND	ND	ND	ND	61.40	4,427.5
14R-6, 52–97	354.5	4.0	76.68	11.17	4.68	239.18	3.62	112.76	ND	ND
15R-3, 0–44	360.9	11.5	435.07	125.48	2.51	69.69	7.44	168.18	553.40	4,865.0
16R-3, 49–89	366.4	21.0	582.67	157.96	18.28	25.96	10.23	152.00	549.40	1,452.5

Note: ND = not determined.

Table T13. Composition of vacutainer gases, Hole 1254A.

Core, section, interval (cm)	Depth (mbsf)	CH_4 (ppmv)	C_2H_6 (ppmv)	C_3H_8 (ppmv)	CH_4/C_2H_6	$i\text{-}C_4H_{10}$ (ppmv)	$n\text{-}C_4H_{10}$ (ppmv)	$i\text{-}C_5H_{12}$ (ppmv)	$n\text{-}C_5H_{12}$ (ppmv)	O_2 (ppmv)	N_2 (ppmv)	CO_2 (ppmv)
205-1254A-												
2R-1, 50–51	156.00	829,680	330	8	2,518	0	0	0	0	28,521	118,002	3,234
3R-4, 3–4	169.78	903,670	292	8	3,090	0	0	0	0	11,831	51,557	3,627
4R-2, 36–37*	176.52	198	0	0	ND	0	0	0	0	193,389	769,438	291
4R-3, 70–71	178.36	867,016	277	8	3,129	0	0	0	0	13,884	61,465	265
4R-6, 98–99	182.59	886,347	181	9	4,908	0	0	0	0	17,988	79,121	2,222
5R-1, 66–67	185.06	923,013	301	17	3,069	0	0	0	0	21,131	89,325	1,937
5R-3, 103–104	188.43	910,937	326	20	2,792	0	0	0	0	20,373	86,010	1,280
5R-6, 130–131	192.15	882,550	376	26	2,346	5	0	0	0	33,336	137,614	1,950
6R-2, 100–101*	196.72	612,219	285	27	2,149	8	0	0	0	72,814	281,291	2,083
6R-4, 50–51	199.43	851,314	629	25	1,353	7	0	0	0	27,060	112,169	1,768
6R-5, 140–141	201.83	956,207	501	51	1,908	13	0	3	0	13,694	59,281	698
7R-1, 50–51	204.30	894,607	473	116	1,890	32	0	5	0	35,297	133,470	1,184
7R-3, 50–51	207.30	938,691	796	90	1,180	34	0	0	0	7,402	38,418	807
7R-4, 50–51	208.80	948,471	616	154	1,540	39	0	3	0	42,842	160,431	710
8R-1, 80–81*	214.20	603,337	494	211	1,222	68	16	8	0	84,138	321,780	1,358
8R-3, 40–41	216.80	947,528	765	326	1,239	93	25	10	0	17,992	77,257	1,776
8R-6, 140–141	221.05	881,667	810	196	1,088	55	7	5	0	38,191	153,519	825
9R-1, 149–150	301.49	928,957	572	141	1,623	ND	ND	ND	ND	ND	ND	ND
9R-3, 23–24	303.23	880,423	552	139	1,594	52	4	7	0	26,208	110,234	755
9R-6, 60–61	306.55	895,369	689	122	1,299	ND	ND	ND	ND	ND	ND	ND
10R-1, 110–111	310.80	763,625	418	139	1,825	56	4	8	0	36,503	148,435	834
10R-3, 55–56	313.25	881,254	448	130	1,966	54	4	8	0	6,975	32,580	561
10R-5, 30–31	316.00	917,558	404	131	2,270	49	4	7	0	24,725	103,840	447
11R-2, 140–141	321.93	941,550	469	178	2,008	66	6	12	0	3,543	11,842	777
11R-4, 90–91*	324.43	588,957	322	92	1,829	33	0	5	0	421,322	523,042	461
11R-6, 105–106	327.17	808,098	325	153	2,484	19	0	3	0	42,381	173,592	466
12R-1, 101–102	329.91	913,616	580	77	1,576	26	0	4	0	23,044	96,937	367
12R-2, 55–56	330.93	798,130	407	117	1,959	51	4	9	0	37,196	151,522	546
12R-3, 50–51	332.38	878,941	643	77	1,368	29	0	7	0	20,894	89,300	564
13R-2, 140–141	341.40	943,481	559	248	1,687	132	10	16	0	29,437	121,739	765
13R-5, 30–31	344.30	892,962	430	296	2,076	113	9	15	0	31,147	127,235	655
13R-7, 3–4	346.67	904,545	402	337	2,251	132	10	16	0	29,437	121,739	765
14R-1, 130–131	349.40	864,757	635	346	1,362	117	10	15	0	34,015	137,379	911
14R-4, 20–21	351.46	920,778	589	371	1,562	130	12	18	0	19,624	83,631	1,142
14R-6, 25–26	354.01	875,068	747	286	1,172	98	10	16	0	26,763	103,524	654
15R-1, 58–59	358.28	910,096	1,091	363	834	158	22	20	0	22,175	98,782	1,032
15R-2, 70–71	359.90	892,257	1,524	207	586	85	16	15	0	27,493	115,613	1,865
15R-4, 25–26	361.40	925,039	649	149	1,426	52	9	8	0	14,101	72,954	2,253
16R-1, 93–94	363.63	678,436	181	34	3,753	4	0	0	0	66,636	277,600	938
16R-2, 122–123	365.42	415,673	68	8	6,085	0	0	0	0	118,358	466,127	885
16R-4, 32–33	366.96	43,831	5	1	9,676	0	0	0	0	182,065	735,276	354

Notes: ppmv = parts per million by volume. * = contamination with air; thus, data points are not plotted in Figure **F45,** p. 86. ND = not determined.

Table T14. Composition of headspace gases, Hole 1254A.

Core, section, interval (cm)	Depth (mbsf)	CH_4 (ppmv)	C_2H_6 (ppmv)	C_2H_4 (ppmv)	C_3H_8 (ppmv)	CH_4/C_2H_6	i-C_4H_{10} (ppmv)	n-C_4H_{10} (ppmv)	i-C_5H_{12} (ppmv)	n-C_5H_{12} (ppmv)	O_2 (ppmv)	N_2 (ppmv)	CO_2 (ppmv)
205-1254A-													
1R-1, 145–150	151.45	1,849	4	0	0	491	0	0	0	0	88,787	764,074	5,261
1R-2, 145–150	152.95	1,276	3	0	1	418	0	0	0	0	78,120	779,273	1,117
1R-3, 42–47	153.42	4,678	8	1	1	616	0	0	0	0	71,147	777,528	2,354
1R-4, 95–100	154.82	88,131	41	1	2	2,144	0	0	0	0	80,056	821,598	6,594
2R-2, 0–5	157.00	6,555	7	1	1	935	0	0	0	0	84,391	745,201	1,272
2R-3, 0–5	158.50	3,639	6	1	1	639	0	0	0	0	78,512	823,220	5,793
2R-4, 0–5	160.00	4,918	6	1	1	784	0	0	0	0	34,866	821,006	9,980
2R-4, 115–120	161.15	1,656	3	0	0	627	0	0	0	0	69,950	714,919	3,865
3R-2, 0–5	166.60	5,168	7	0	1	785	0	0	0	0	111,214	782,638	7,306
3R-3, 115–120	169.25	11,525	8	1	1	1,468	0	0	0	0	33,403	844,756	1,939
3R-3, 0–5	168.10	101,042	46	0	4	2,197	0	0	0	0	76,595	817,468	3,556
3R-4, 0–5	169.75	6,376	8	0	0	789	0	0	0	0	68,737	789,508	5,485
4R-1, 140–146	176.10	8,141	5	0	1	1,728	0	0	0	0	57,205	774,859	303
4R-3, 0–5	177.66	5,993	5	1	1	1,233	0	0	0	0	66,403	774,784	585
4R-4, 0–5	179.16	4,953	5	1	2	1,072	0	0	0	0	70,971	767,991	4,455
4R-6, 0–5	181.61	5,640	5	1	2	1,205	0	0	0	0	78,793	746,031	236
5R-1, 145–150	185.85	100	0	0	0	ND	0	0	0	0	189,297	768,861	159
5R-3, 0–5	187.40	22,419	14	0	3	1,591	0	0	0	0	64,169	780,384	152
5R-5, 45–50	190.35	5,064	6	0	2	917	0	0	0	0	77,542	785,309	87
5R-7, 95–100	193.30	2,703	5	0	3	595	0	0	0	0	81,520	805,369	99
6R-2, 0–5	195.72	2,573	3	0	2	825	0	0	0	0	175,926	742,565	43
6R-4, 0–2	198.93	4,089	5	1	3	745	0	0	0	0	109,321	724,104	51
6R-5, 0–5	200.43	4,855	7	0	5	667	0	0	0	0	71,896	859,482	19
6R-6, 0–2	201.93	5,751	11	1	11	529	5	0	3	0	65,553	870,279	137
7R-1, 145–150	205.25	7,845	8	0	12	964	6	0	3	0	24,786	873,548	21
7R-2, 145–150	206.75	3,751	6	1	13	578	4	0	0	0	51,136	840,265	21
7R-4, 0–5	208.30	9,327	20	1	27	478	7	0	4	0	92,858	827,974	25
7R-6, 0–5	210.00	5,117	9	0	18	596	6	0	3	0	93,080	835,140	17
8R-2, 0–5	214.90	15,923	30	0	91	534	56	21	19	0	80,703	653,130	48
8R-3, 120–125	217.60	7,089	19	0	67	375	33	10	9	0	104,952	618,808	24
8R-6, 0–5	219.65	721	4	0	32	184	24	7	9	0	158,300	791,063	45
8R-7, 95–100	222.10	6,590	20	0	92	324	39	7	10	0	132,536	798,058	17
9R-2, 0–5	301.50	12,256	6	0	8	1,952	5	0	0	0	132,411	742,241	92
9R-3, 0–5	303.00	4,562	5	0	11	960	0	0	0	0	172,870	774,369	0
9R-4, 0–5	304.50	2,848	4	0	10	669	0	0	0	0	176,798	766,672	19
9R-6, 0–5	305.95	2,282	6	0	9	385	0	0	0	0	184,549	771,808	42
10R-2, 0–5	311.20	4,971	5	0	9	1,067	0	0	0	0	176,147	779,170	30
10R-3, 145–150	314.15	6,146	5	0	8	1,187	0	0	0	0	176,350	768,369	22
10R-5, 0–5	315.70	4,727	5	0	10	913	0	0	0	0	173,888	743,730	25
10R-7, 0–5	317.18	3,104	3	0	7	910	0	0	0	0	182,073	769,125	28
11R-2, 0–5	320.53	21,946	11	0	18	1,952	6	0	4	0	82,384	812,569	24
11R-4, 0–5	323.53	16,565	8	0	11	1,972	0	0	0	0	140,382	775,786	60
11R-6, 0–5	326.12	8,935	10	0	14	922	4	0	3	0	105,809	805,924	18
11R-6, 145–150	327.57	2,657	3	0	7	897	0	0	0	0	184,540	765,791	24
12R-1, 96–101	329.86	19,649	12	0	12	1,578	5	0	4	0	86,694	816,463	18
12R-3, 0–5	331.88	9,946	8	0	20	1,264	12	0	8	0	11,527	715,020	29
13R-2, 0–5	340.00	23,944	15	0	26	1,590	14	0	5	0	55,554	777,754	24
13R-4, 0–5	343.00	7,753	6	0	14	1,330	0	0	0	0	180,797	771,285	231
13R-6, 0–5	345.14	5,798	5	0	17	1,218	10	0	4	0	78,405	854,699	23
13R-7, 0–5	346.64	1,138	2	0	7	654	ND	ND	ND	ND	ND	ND	ND
14R-1, 145–150	349.55	11,139	13	0	70	841	0	0	0	0	186,182	771,754	345
14R-2, 116–120	350.76	21,920	15	0	68	1,475	43	4	12	0	101,936	831,894	18
14R-5, 0–5	352.76	790	2	0	11	317	0	0	0	0	184,068	770,607	66
14R-6, 47–52	354.23	3,209	7	0	40	446	19	0	6	0	113,138	825,052	0
15R-1, 145–150	359.15	11,663	8	0	32	1,382	21	6	12	0	121,282	827,802	22
15R-2, 140–145	360.60	9,552	21	1	42	448	28	5	6	0	26,464	833,905	384
15R-4, 0–5	361.15	19,217	14	1	10	1,335	4	0	0	0	88,263	824,115	807
16R-1, 145–150	364.15	37,777	10	0	3	3,657	0	0	0	0	116,384	775,469	4,695
16R-2, 145–150	365.65	32,104	9	1	2	3,656	0	0	0	0	129,888	783,455	5,287
16R-4, 0–5	366.64	24,375	4	1	1	5,888	0	0	0	0	98,474	667,698	17,536

Notes: ppmv = parts per million by volume. ND = not determined.

Table T15. Calcium carbonate, inorganic carbon, total carbon, total nitrogen, total sulfur, and total organic carbon contents in sediments, Hole 1254A.

Core, section, interval (cm)	Depth (mbsf)	$CaCO_3$ (wt%)	IC (wt%)	TC (wt%)	TN (wt%)	TS (wt%)	TOC (wt%)	TOC/TN
205-1254A-								
1R-3, 52–87	153.52	6.80	0.82	1.98	0.24	0.18	1.16	4.8
2R-4, 125–160	161.25	6.83	0.82	1.47	0.22	0.12	0.65	3.0
3R-3, 125–165	169.35	4.59	0.55	1.49	0.20	0.47	0.94	4.6
4R-5, 45–90	181.11	3.89	0.47	1.49	0.21	0.72	1.02	5.0
5R-5, 50–90	190.40	7.37	0.88	1.83	0.21	0.22	0.95	4.5
6R-1, 121–162	195.31	5.18	0.62	1.68	0.22	0.29	1.06	4.9
6R-2, 125–166	196.97	7.47	0.90	1.48	0.18	0.17	0.58	3.2
7R-5, 34–74	209.55	3.25	0.39	1.41	0.18	0.83	1.02	5.6
8R-4, 0–45	217.65	5.93	0.71	1.75	0.17	1.08	1.04	6.1
9R-5, 0–40	305.50	7.37	0.88	1.62	0.19	0.35	0.74	3.9
10R-6, 0–40	316.73	5.73	0.69	1.58	0.18	0.29	0.89	5.1
11R-1, 78–117	320.08	3.27	0.39	1.27	0.17	0.65	0.88	5.1
11R-5, 63–103	325.67	2.04	0.24	1.08	0.18	0.74	0.84	4.6
12R-1, 101–141	329.91	2.02	0.24	1.10	0.16	1.21	0.86	5.4
13R-3, 100–145	342.50	2.41	0.29	1.14	0.17	0.89	0.85	5.1
13R-5, 65–109	344.65	5.74	0.69	1.54	0.18	0.47	0.85	4.6
14R-3, 0–40	350.81	4.12	0.49	1.47	0.19	1.40	0.98	5.2
14R-6, 52–97	354.28	6.27	0.75	1.63	0.17	1.37	0.88	5.3
15R-3, 0–44	360.65	1.04	0.13	2.03	0.25	1.20	1.90	7.7
16R-3, 49–89	366.19	1.04	0.12	1.60	0.18	0.78	1.48	8.3

Note: IC = inorganic carbon, TC = total carbon, TN = total nitrogen, TS = total sulfur, TOC = total organic carbon. Accuracies of TS and TN are very poor, ~20% (see **"Organic Geochemistry,"** p. 26, in the "Explanatory Notes" chapter).

Table T16. Rock-Eval data, Hole 1254A.

Core, section, interval (cm)	Depth (mbsf)	T_{max} (°C)	S_1 (mg HC/g)	S_2 (mg HC/g)	PI (S_1/[S_1+S_2])	PC (0.083 × S_1/S_2)	HI (mg HC/ g TOC)	TOC (wt%)
205-1254A-								
1R-3, 52–87	153.52	413	0.07	0.63	0.10	0.009	54	1.16
2R-4, 125–160	161.25	415	0.07	0.71	0.09	0.008	109	0.65
3R-3, 125–165	169.35	415	0.08	0.75	0.10	0.009	80	0.94
4R-5, 45–90	181.11	424	0.07	0.67	0.09	0.009	65	1.02
5R-5, 50–90	190.40	414	0.10	0.94	0.10	0.009	99	0.95
6R-1, 121–162	195.31	412	0.10	0.63	0.14	0.013	59	1.06
6R-2, 125–166	196.97	418	0.08	0.69	0.10	0.010	119	0.58
7R-5, 34–74	209.55	432	0.64	17.28	0.04	0.003	1,694	1.02
8R-4, 0–45	217.65	427	0.07	0.52	0.12	0.011	50	1.04
9R-5, 0–40	305.50							0.74
10R-6, 0–40	316.73	407	0.06	0.57	0.10	0.009	64	0.89
11R-1, 78–117	320.08	410	0.11	0.44	0.20	0.021	50	0.88
11R-5, 63–103	325.67	411	0.06	0.40	0.13	0.012	48	0.84
12R-1, 101–141	329.91	418	0.07	0.49	0.13	0.012	57	0.86
13R-3, 100–145	342.50	406	0.08	0.45	0.15	0.015	53	0.85
13R-5, 65–109	344.65	406	0.10	0.49	0.17	0.017	58	0.85
14R-3, 0–40	350.81	419	0.40	0.88	0.31	0.038	90	0.98
14R-6, 52–97	354.28	417	0.12	0.85	0.12	0.012	96	0.88
15R-3, 0–44	360.65	419	0.11	0.81	0.12	0.011	43	1.90
16R-3, 49–89	366.19	409	0.47	2.36	0.17	0.017	159	1.48

Notes: T_{max} = temperature of maximum hydrocarbon generation from kerogen, S_1 = volatile hydrocarbons, S_2 = kerogen-derived hydrocarbons, PI = productivity index, PC = pyrolizable carbon, HI = hydrogen index, TOC = total organic carbon obtained by CNS-elemental analysis.

Table T17. Microsphere abundance in microbiology whole rounds, Hole 1254A.

Core, section, interval (cm)	Top depth (mbsf)	Microspheres per mg of sediment	
		Interior	Exterior
205-1254A-			
1R-3, 47–52	153.47	0.00	1.00
2R-4, 120–125	161.20	0.00	1.58
3R-3, 120–125	169.30	0.07	0.76
4R-5, 90–95	181.56	0.00	0.69
5R-5, 90–95	190.80	0.00	0.07
6R-1, 115–121	195.25	0.00	0.21
6R-2, 166–171	197.38	0.00	0.08
7R-5, 74–79	209.95	0.00	0.39
8R-4, 45–50	218.10	0.00	0.46
9R-5, 40–45	305.90	0.00	0.00
10R-6, 40–45	317.13	0.03	0.61
11R-1, 117–123	320.47	0.00	0.34
11R-5, 103–108	326.07	0.00	0.52
12R-1, 141–148	330.31	0.00	0.82
13R-3, 145–150	342.95	0.24	0.72
13R-5, 109–114	345.09	0.05	0.22
14R-3, 40–45	351.21	0.18	0.14
14R-6, 97–102	354.73	0.00	0.79
15R-3, 44–50	361.09	0.08	1.21
16R-3, 89–94	366.59	0.00	0.00